Search for charginos and neutralinos decaying to final states with one lepton

Suche nach Charginos und Neutralinos in Endzustände mit einem Lepton

Master Thesis
Ludwig-Maximilians-Universität München

Faculty of Physics

Lars Ferencz

Munich, April 1, 2020

Supervisor: Prof. Dr. Dorothee Schaile

Abstract

Profiting from the large pp data statistics available, collected by the ATLAS detector at the LHC during Run 2, some searches for the electroweak production of supersymmetric particles get accessible for the first time. This work presents searches for two kinds of models:
1. chargino pair production, where both charginos $\tilde{\chi}_1^{\pm}$ decay to a W boson and the lightest neutralino $\tilde{\chi}_1^0$ (lightest supersymmetric particle, LSP)
2. chargino and neutralino pair production, where the chargino $\tilde{\chi}_1^{\pm}$ decays to a W boson and the lightest neutralino $\tilde{\chi}_1^0$ (lightest supersymmetric particle, LSP), and the neutralino $\tilde{\chi}_2^0$ to a Z boson and the LSP.
The searches presented focus on signatures with an isolated electron or muon, which provides complementary sensitivity to searches in multilepton signatures. Depending on the boost of the W and Z boson emitted, advanced tagging techniques to identify these bosons can be used, leading to different types of search region definitions.

Zusammenfassung

In dieser Arbeit wird die Suche nach Supersymmetry ausgehend von der elektroschwachen Produktion zweier supersymmetrischer Teilchenarten untersucht. Das Studium der elektroschwachen Produktion von supersymmetrischen Teilchen wird zum ersten Mal durch die hohe Datenmenge, die ATLAS während dem Run-2 aufgenommen hat, zugänglich. Diese Arbeit präsentiert zwei Analysen:
1. Chargino Paarproduktion, bei der beide Charginos $\tilde{\chi}_1^{\pm}$ in ein W Boson und das leichteste Neutralino $\tilde{\chi}_1^0$ (Lightest Supersymmetric Particle, LSP) zerfallen.
2. Chargino und Neutralino Paaproduktion, bei der das Chargino $\tilde{\chi}_1^{\pm}$ in ein W Boson und das leichteste Neutralino $\tilde{\chi}_1^0$ (LSP)zerfallen und das Neutralino $\tilde{\chi}_2^0$ in ein Z Boson und das LSP zerfallen.
Der betrachtete Zerfallskanal beinhaltet genau ein isoliertes Elektron oder Muon, wodurch sich die Analyse von komplemetären Analysen in multilepton Zerfallskanälen unterscheiden kann. Die präsentierten Analysestrategien studieren die Kombination von Rekonstruktionstechniken die auf geboostete Signaturen eines W und Z Boson optimiert sind und Rekonstruktionstechniken die auf die gegenteiligen sogenannten resolved Signaturen W und Z Boson optimiert sind.

Contents

Chapter 1

Introduction

The Standard Model of particle physics has proven to be a very successful theory in describing physical processes on the energy scale accessible to modern collider experiments. One of the largest experiments in the field of particle physics is the Large Hadron Collider located at the CERN facility in Geneva.
However, the Standard Model of particle physics lacks a number of answers for outstanding problems. For example it cannot describe all four fundamental Interactions. Further problems are discussed in chapter 2.2. From these observations, we know that the Standard Model of particle physics does not yet formulate a complete theory that describes the problems of particle physics beyond the Planck scale. It appears that the Standard Model of particle physics could be an approximation at low energies of an overarching theory describing particle physics. This work presents searches for Supersymmetry, which is described in chapter 2.3. Supersymmetry could provide answers to the aforementioned problems of the Standard Model, which are discussed in chapter 2.2. In particular, Supersymmetry could describe particle physics on all energy scales. One consequence introduced by Supersymmetry is the prediction of a class of partner particles for all particles included in the Standard Model description.

It is expected that these supersymmetric partner particles are heavier than their Standard Model counterparts. Several collider experiments have already investigated signatures of superymetric models, e.g. PETRA, LEP and Tevatron. Now the LHC, which reaches the highest centre-of-mass energies of every collider ever used, targets regions going up to the TeV mass scale. The amount of data that the LHC has recorded so far, makes it possible to search for supersymmetric particles produced in electroweak processes. This work describes the analysis of two SUSY models based on the pair production of supersymmetric electroweak bosons, which are described in chapter 2.6. For both models a full analysis is carried out for the first time in a final state, that contains one lepton and two jets. Until this point, results from analysis looking for two and three lepton final states have been published with a partial dataset of 36.1 fb^{-1} (2015-2016) (1) and the full Run-2 dataset of 139 fb^{-1} (1). For the presented analysis the full Run-2 dataset is analysed.

Chapter 2

Theoretical introduction

First a quick overview of the Standard Model of particle physics is given based on (2, 3, 4, 5). Afterwards the idea behind Supersymmetry and its motivation is illustrated as described by (6).

2.1 The Standard Model of particle physics

The Standard Model of particle physics (SM) is a theory describing the fundamental elementary particles and their interactions except gravity. Fundamental interactions such as strong, electromagnetic and weak interactions are described by Quantum Field Theories (QFT). The effect of gravity is small at energy scales accessible to the LHC and not described in the SM. Figure 2.1 shows an overview of the particle content of the SM. It can be categorized into

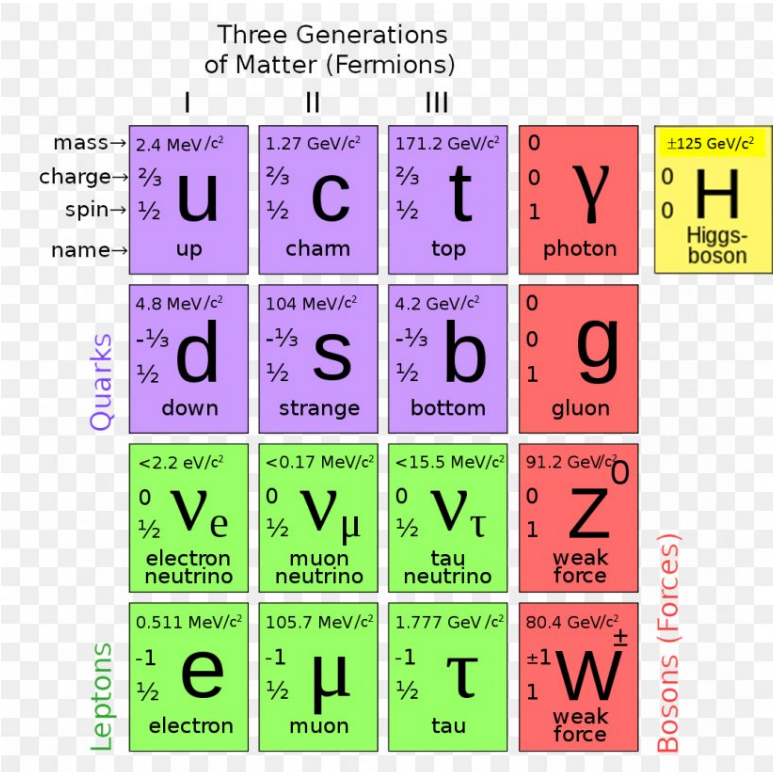

Figure 2.1: Particle content of the SM (7)

two categories: fermions and bosons. Quarks and leptons are fermions with spin $\frac{1}{2}$, while the mediator particles of the fundamental interactions are bosons with spin 1. In the context of the SM, the Higgs takes a special role as a spin 0 scalar boson.
In the SM left-handed quarks and leptons are ordered in $SU(2)_L$ doublets with three generations, while right-handed particles are ordered in singlets. A quark doublet consists of an up-type (el.charge: $+\frac{2}{3}$) and a down-type (el.charge: $-\frac{1}{3}$) quark. The three generations are ordered by mass. This coincides with the historic order they were discovered. The weak coupling of the three generations can be expressed in the formalism of the weak interaction and is illustrated by the Cabibbo-Kobayashi-Maskawa (CKM) matrix (8). The CKM matrix gives the probability of a quark flavour change in weak interactions.
Considering the case of $SU(2)_L$ lepton doublets, the three generations correspond to the number of leptons ordered in an ascending order by their mass. The other particle in each doublet is the corresponding neutrino. In the context of the SM neutrinos are assumed to be massless particles, but from observations of neutrino flavour oscillations, it is known at least two neutrinos need to be massive (9). Extensions of the SM like the one presented in (10) describe the inclusion of neutrino oscillation within the SM.
The interaction between fermions is mediated by gauge bosons. Electromagnetic processes are mediated by the exchange of a photon, weak interaction is mediated by the W and Z bosons and strong interactions are mediated by gluons. In the following the underlying theories depicting the fundamental interactions in the SM are described.

2.1.1 The SM as a gauge theory

As already mentioned, one can formulate the SM as gauge theories described by the following symmetry group:

$$SU(3)_c \otimes SU(2)_L \otimes U(1)_Y \tag{2.1}$$

The symmetry group describes the three fundamental interactions the SM consists of: Strong interaction processes are described by $SU(3)_c$ with 'c' referring to the colour charges. The symmetry group of the weak interaction is represented by $SU(2)_L$.
$U(1)_Y$ is the symmetry group describing electromagnetic interactions.
In comparison to the classical interpretation of a particle as a discrete mass point, in context of QFTs particles are described as fields $\phi(\vec{x}, t)$. In a similar way as for the classical interpretation, the action S is given by the Lagrangian density $\mathcal{L}(\phi_i, \delta_\mu \phi_i)$ integrated over the spacetime.

$$S = \int \mathcal{L}(\phi_i, \delta_\mu \phi_i) d^4x \tag{2.2}$$

Applying the principle of least action yields the Euler-Lagrange equation:

$$\partial_\mu \left(\frac{\partial \mathcal{L}}{\partial(\partial_\mu \phi_i)} \right) - \frac{\partial \mathcal{L}}{\partial \phi_i} = 0 \tag{2.3}$$

The Lagrangian has to be invariant under local and global phase transformations. Global phase transformations can be interpreted as a shift of the reference point, which can be understood as changing the point of origin. Local gauge transformations are described as a shift of the physics at each point in space and time.

2.1.2 Strong Interaction (QCD)

QCD describes the strong interaction based on a gauge theory with a $SU(3)_C$ symmetry group. The theoretical interpretation of the strong interaction introduces a colour charge, which only couples to quarks and gluons.
Colour charges are defined as fundamental properties in QCD similar to an electrical charge in QED. The three colour charges and the corresponding three anti colour charges are typically depicted in analogy as colours red, blue and green. Gluons, as the mediator particles of the strong interaction, only couple to particles that have a colour charge. Gluons carry a colour and an anti-colour, while every quark has a colour and respectively anti-quarks carry anti-colour. Therefore gluons are their own antiparticles. There are nine potentially possible colour gluon states, of which eight are allowed in nature while the singlet state $\frac{1}{\sqrt{3}}(|r\bar{r}\rangle + |b\bar{b}\rangle + |g\bar{g}\rangle)$ corresponds to a neutrally charged gluon which would not interact with other colour charged particles and does not exist.

2.1.3 Electromagnetic Interaction (QED)

Reflected by a $U(1)_Y$ symmetry group, QED describes the interaction of charged leptons based on their electromagnetic properties. In the electromagnetic theory electrically charged leptons can interact by exchanging a photon, which acts as the neutral mediator particle.

A spin-$\frac{1}{2}$ particle is described by the free Dirac Lagrangian:

$$\mathcal{L}_D = \bar{\Psi}(i\gamma^\mu \partial_\mu)\Psi - m\bar{\Psi}\Psi \tag{2.4}$$

From this, the following equation of motion is obtained for a spin-$\frac{1}{2}$ particle by acting on the wave function .

$$(i\gamma^\mu \partial_\mu - m)\Psi = 0 \tag{2.5}$$

Classical electrodynamics derived the free Lagrangian of a photon as:

$$\mathcal{L}_\gamma = -\frac{1}{4}[\partial_\mu A_\nu - \partial_\nu A_\mu][\partial^\mu A^\nu - \partial^\nu A^\mu] = -\frac{1}{4}F_{\mu\nu}F^{\mu\nu} \tag{2.6}$$

A_μ is defined as the field of the photon. One requirement a QFT has to comply with is the local and global gauge invariance. While the Lagrangians are invariant under global gauge invariance, if applying a local gauge invariance in form of $\Psi' \rightarrow e^{iq\chi(\vec{x},t)}\Psi$ it becomes apparent that the Dirac equation is not invariant. $\chi(\vec{x},t)$ depicts a phase-shift that has a space-time dependency. A consequence is that non-interacting particle fields cannot formulate a local gauge invariant theory, because the mass term violates the invariance. A solution to this problem is the introduction of a new derivative:

$$\partial_\mu \rightarrow D_\mu = \partial_\mu + iqA_\mu$$

A_μ represents a infinitesimal small gauge transformation on Ψ.

$$A_\mu \rightarrow A_\mu - \tfrac{1}{q}\partial_\mu \chi(\vec{x}, t)$$

Leading to the full QED Lagrangian:

$$\mathcal{L}_{QED} = \bar{\Psi}(i\gamma^\mu \partial_\mu - m)\Psi - \frac{1}{4}F_{\mu\nu}F^{\mu\nu} - gA_\mu \bar{\Psi}\gamma^\mu \Psi \tag{2.7}$$

The first term describes a freely propagating spin-$\frac{1}{2}$ fermion field. Described by the second term is the A_μ field of a propagating photon. Term three describes the interaction between both fields involving a charge q.

2.1.4 Weak Interaction

First historic examples of weak interactions are given by β decays. In a β-decay a neutron decays into a proton while emitting an electron and a neutrino, as illustrated in figure 2.2. On parton level the β decay can be expressed as a weak quark flavour change mediated by

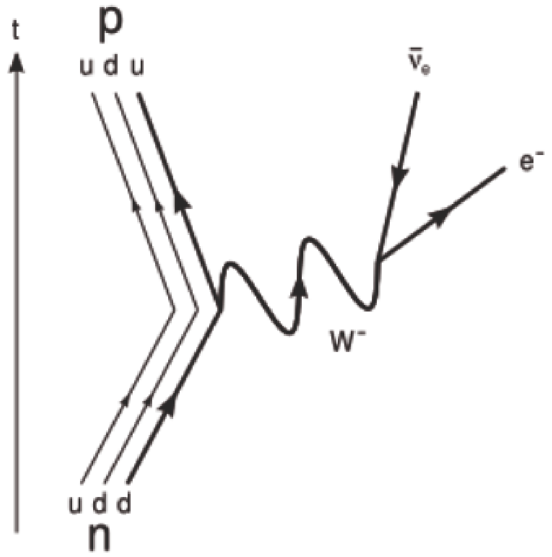

Figure 2.2: Illustration of the β-decay (11)

a W boson. For the formulation of a fundamental theory describing weak interactions the Dirac equation presents a sufficient starting point. While QED was described by a U(1) symmetry group, weak interactions are described by a two dimensional SU(2) group which transformations are illustrated in the form of a "rotation" of two dimensional complex vector spinors. Using those it is possible to formulate a Lagrangian that is invariant under SU(2) local gauge transformation.

$$\Psi \rightarrow exp\left(i\frac{\vec{\sigma}\vec{\theta}}{2}\right)\Psi \tag{2.8}$$

where $\vec{\sigma}$ are the three Pauli matrices and $\vec{\theta}$ denotes a local phase under which the system transforms.

$$\sigma_1 = \begin{pmatrix} 0 & 1 \\ 1 & 0 \end{pmatrix}, \sigma_2 = \begin{pmatrix} 0 & -i \\ i & 0 \end{pmatrix}, \sigma_3 = \begin{pmatrix} 1 & 0 \\ 0 & -1 \end{pmatrix}$$

As a basis the equation of motion of that describes spin-$\frac{1}{2}$ particles is used.

$$\mathcal{L} = \bar{\Psi}(i\gamma^\mu \partial_\mu - m)\Psi \tag{2.9}$$

In order to formulate a gauge invariant theory describing weak interactions introduce a new covariant derivative:

$$\partial_\mu \rightarrow \partial_\mu + ig\frac{1}{2}\vec{\sigma}\vec{W}_\mu \tag{2.10}$$

g describes the SU(2) gauge field coupling and $\vec{W}_\mu$ denotes the three new gauge fields $\vec{W}_\mu = (W_1, W_2, W_3)$ associated with the three spin-1 gauge bosons. Inserting the covariant derivative leads to the new formulation of the Lagrangian:

$$\mathcal{L}_{SU(2)} = \bar{\Psi}(i\gamma^\mu \partial_\mu - m)\Psi - \frac{1}{4}F_{\mu\nu}F^{\mu\nu} - \frac{g}{2}\vec{W}_\mu \bar{\Psi}\gamma^\mu \vec{\sigma}\Psi \tag{2.11}$$

The first term describes a freely propagating spin-$\frac{1}{2}$ particle, the second term describes the gauge field and the third describes the interaction of the gauge field. Charged currents are mediated by the W_μ^1 and W_μ^2 fields corresponding to the W^+ and W^-, while neutral currents are represented by the mix between the photon field B_μ and the third component of the weak gauge boson field W_μ^3. Measurements of the electroweak gauge boson mass have contradicted the interpretation of the electroweak formalism (12) depicting the bosons as massless particles.

2.1.5 Higgs mechanism

The Higgs mechanism offers a solution to the fundamental problem that electroweak gauge bosons are massive particles. Introducing the idea of spontaneous symmetry breaking (SSB), the problem related to the massless nature of electroweak gauge bosons can be explained. Ideas of spontaneous symmetry breaking have general applications in various fields of physics. The general idea behind SSB is that the ground state does not share the same symmetry as the underlying theoretical theory. An additional term is introduced in the Lagrangian describing the Higgs potential of a scalar real field ϕ :

$$V(\phi) = -\mu^2 \phi^* \phi + \frac{\lambda}{2}(\phi^* \phi)^2 \tag{2.12}$$

This potential has a vacuum expectation value (VEV) of $< |\phi| >= \sqrt{\frac{\mu^2}{\lambda}} = v$. The ground state of ϕ can be chosen as

$$\phi(x) = \frac{1}{\sqrt{2}} \begin{pmatrix} 0 \\ v \end{pmatrix} \tag{2.13}$$

The original $SU(2)_L \otimes U(1)_Y$ gets thus broken to $U(1)_{em}$. After SSB, the QED gauge group $U(1)_{EM}$ appears as a linear combination of an U(1) subgroup of $SU(2)_L$ and $U(1)_Y$. Induced by SSB the W^1_μ and W^2_μ mix:

$$W^+ \equiv \frac{W^1_\mu + iW^2_\mu}{\sqrt{2}} \tag{2.14}$$

$$W^- \equiv \frac{W^1_\mu - iW^2_\mu}{\sqrt{2}} \tag{2.15}$$

Moreover, for the case of a neutral current mediator:

$$\begin{pmatrix} Z_\mu \\ A_\mu \end{pmatrix} = \begin{pmatrix} cos(\theta_w) & -sin(\theta_w) \\ sin(\theta_w) & cos(\theta_w) \end{pmatrix} \begin{pmatrix} W^3_\mu \\ B_\mu \end{pmatrix} \tag{2.16}$$

θ_w denotes the Weinberg angle defined as:

$$cos(\theta_w) = \frac{M_W}{M_Z} \tag{2.17}$$

2.1.6 Higgs-boson

The discovery of the Higgs-boson was the last piece in the experimental validation of the particle content of the SM. Predicted by the Higgs mechanism, the Higgs-boson can be interpreted as an excitation of the interacting Higgs field. It can only couple to particles that are massive after SSB.

2.2 Issues with the SM

The SM has proven to be a remarkably successful theory for describing measurements given by experiments like the LHC. While the SM has been tested extensively, there are open issues the SM cannot explain.

Dark matter

Cosmological measurements (13) have shown that only a fraction of the mass in the universe consists of luminous baryonic matter. The non-luminous matter is called dark matter. Most theories describing dark matter predict that it would at most only weakly interact with ordinary matter.The SM offers no suitable candidate for cold dark matter(14). Different extensions of the SM propose candidates for the cold dark matter, e.g. Weakly Interacting Massive Particles.

Gravity

The formulation of a theory unifying the SM with gravity is an outstanding task. Gravity is non-negligible at the Planck scale ($M_p = (8\pi G_{Newton})^{-\frac{1}{2}} = 2.4 \cdot 10^{18}$GeV)(6). For a theory of particle physics to include gravity is thus only relevant at the Planck scale and is neglectable below that.

Hierarchy problem

One motivation for an extension of the SM by an overarching model as given by the hierarchy problem. m_H^2, which is the mass of the Higgs, is sensitive to quantum corrections. These corrections are introduced by every particle that couples directly or indirectly to the Higgs field. In particular, it can be seen that m_H^2 is sensitive to the masses of heavy particles coupling to the Higgs. Generally speaking the mass of the Higgs boson $\Delta m_H \sim |\lambda_f^2|$ and $\lambda_f \sim m_f$. m_f is the mass of a fermion. Similarly $\Delta m_H \sim \lambda_s$ (6) where λ_s describes the coupling of the Higgs to a scalar boson. For both cases the actual contribution to the Higgs mass is limited by a cutoff scale. If one assumes that the description of particle physics by the SM stays valid up to the Planck scale (10^{18}GeV) the cutoff scale could then be of the same order as the Planck scale. After the discovery of the Higgs boson in 2012 (15) measurements of the Higgs mass have shown that m_H^2 is small compared to the Planck scale. A fundamental question arising from this observation is to understand why the Higgs mass is various orders of magnitudes smaller than the Planck scale.

2.3 Supersymmetry

Supersymmetry (SUSY) is a class of theories defined by the characteristics that a fundamental symmetry between bosons and fermions exists. The fundamental symmetry between fermions and bosons is described by transforming a fermionic state to a bosonic state and vice versa using a fermionic operator $\mathcal{Q}$:

$$\mathcal{Q}|Fermion\rangle = |Boson\rangle \tag{2.18a}$$
$$\mathcal{Q}|Boson\rangle = |Fermion\rangle \tag{2.18b}$$

$\mathcal{Q}$ has to satisfy the supersymmetric algebra:

$$\{\mathcal{Q}, \mathcal{Q}^\dagger\} = P^\mu \tag{2.3a}$$

$$\{\mathcal{Q}, \mathcal{Q}\} = \{\mathcal{Q}^\dagger, \mathcal{Q}^\dagger\} = 0 \tag{2.3b}$$

$$[P^\mu, \mathcal{Q}^\dagger] = [P^\mu, \mathcal{Q}^\dagger] = 0 \tag{2.3c}$$

P_μ is a four momentum generator describing the translation in spacetime.
Supersymmetry predicts the existence of supersymmetric partner particles of the respective SM particles. These can then be ordered in supermultiplets. A consequence derived from equation 2.3c) is that P^2, which is the squared-mass operator, commutes with the $\mathcal{Q}$ and $\mathcal{Q}^\dagger$ the hermitian conjugate. An interpretation of this consequence is that all particles in the same supermultiplet have equal masses and quantum numbers, which include the electric charge, weak isospin and colour charge, as their SM partner. SM particles and their SUSY partners will only be distinguishable by their spin quantum number.

2.3.1 Supersymmetry breaking

SUSY predicts superpartners with the same mass as their SM partners. As no SUSY particle has been discovered yet, the SUSY partners cannot have the same mass as their SM partners and SUSY needs to be a broken Symmetry. Ensuring that SUSY provides a solution to the hierarchy problem the breaking of SUSY needs to be soft:

$$\mathcal{L} = \mathcal{L}_{SUSY} + \mathcal{L}_{soft} \tag{2.4}$$

Equation 1.4 shows the effective Lagrangian in which $\mathcal{L}_{\text{SUSY}}$ is the SUSY conserving part of the Lagrangian, while the symmetry breaking is introduced by the $\mathcal{L}_{\text{soft}}$ part of the equation.

2.4 The MSSM and its particle content

The Minimal Supersymmetric Standard Model describes the minimal extension of the SM in terms of new particles. Table 2.1 gives an overview of the supermultiplets of the MSSM.

The SSB of $SU(2)_L \otimes U(1)_{em}$ leads to a mixing of states with the same electric chage, colour and spin (16) and means that the elecroweak gauginos and higgsinos are not the physical particles. They mix to form neutralinos $\tilde{\chi}_i^0$ and charginos $\tilde{\chi}_i^\pm$. Neutralinos are defined as mixed eigenstates of higgsinos ($\tilde{H}_u^0$,$\tilde{H}_d^0$) with $\tilde{B}$ and $\tilde{W}^0$ yielding four particles called neutralinos ($\tilde{\chi}_1^0$,$\tilde{\chi}_2^0$,$\tilde{\chi}_3^0$,$\tilde{\chi}_4^0$), ordered by mass from lowest to highest. The mixing of charged higgsinos ($\tilde{H}_u^+$,$\tilde{H}_d^-$) with $\tilde{W}^+$ and $\tilde{W}^-$ results in four charginos ($\tilde{\chi}_1^\pm$,$\tilde{\chi}_2^\pm$). Both signal models discussed in section 1.6 are based on the pair production of charginos and neutralinos.

2.5 R-parity

The MSSM allows baryon and lepton number violating decays. One example would be a possible decay mode of the proton $p^+ \to e^+ + \pi^0$, which would be in contradiction to measurements of the lifetime of the proton which is measured to be in the order of at least 10^{31}s

Table 2.1: List of Supermultiplets in the MSSM

Particle type	spin 0	spin $\frac{1}{2}$	spin 1
sleptons/leptons	$(\tilde{\nu},\, \tilde{e}_L)$	$(\nu,\, e_L)$	-
	$\tilde{e}_{R^*}$	e_R	
squarks/ quarks	$(\tilde{u}_L,\tilde{d}_L)$	(u_L,d_L)	-
	$\tilde{u}_{R^*}$	$u_R^\dagger$	-
	$\tilde{d}_{R^*}$	$d_R^\dagger$	-
gluino/gluon	-	$\tilde{g}$	g
wions/ W bosons	-	$\tilde{W}^{\pm/0}$	$W^{\pm/0}$
bions/ B boson	-	$\tilde{B}^0$	B^0
Higgs/ Higgsinos	(H_u^+,H_u^0)	$(\tilde{H}_u^+,\tilde{H}_u^0)$	-
	(H_d^0,H_d^-)	$(\tilde{H}_d^0,\tilde{H}_d^-)$	-

(17). To prevent this, a new conserved quantum number is introduced, the so called R parity:

$$P_R = (-1)^{3(B-L)+2s}$$

B and L are the baryon and lepton number while s refers to the spin of the given particle. SM particles have a R-parity value of 1 and SUSY particle have a value of -1. Conservation of R-parity leads to that SUSY particles are always produced in pairs. Conservation of R-parity is a frequent requirement in a variety of SUSY theories. If R-parity is conserved, the lightest supersymmertric particle (LSP) is a stable particle. The LSP might be a good dark matter candidate. On the other hand, there are other classes of theories which allow for a violation of the R-parity. This work only considers models with R-parity conservation.

2.6 Description of the WW and WZ model

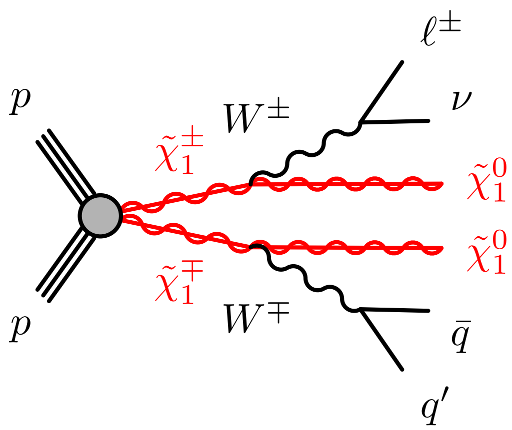

(a) WW model

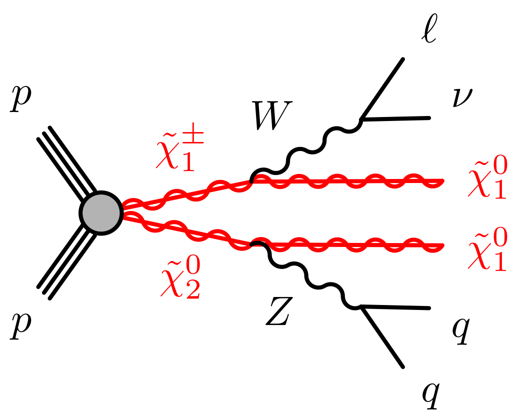

(b) WZ model

Figure 2.3: SUSY signal models

In context of the analysis presented, two simplified SUSY models are proposed. In a simplified model it is assumed that only SUSY particles explicitly appearing are accessible to the experiment, while all other SUSY particles decouple. The decays of the SUSY particles are clearly defined in a given simplified model. While a simplified model does not represent a "realistic" theory the reasoning behind the usage of simplified models is based on the idea that simplified models reduce the amount of free parameters. For example in the MSSM one has $\sigma(100)$ free parameters (18).

Figure 2.3 shows decay diagrams for both models considered in this work. Both models consider the pair production . Taking a more detailed look at Figure 2.3 a), it shows chargino pair production. Both charginos decay into a W boson and a neutralino, here assumed to be the lightest supersymmetric particle (LSP). Because the neutralino is assumed to be a stable particle that only interacts weakly with the SM particles, the neutralino escapes the detector without signal. On the other hand, the produced W bosons decays into SM particles. Focusing on a final state with one lepton, one of the W bosons decays leptonically into a lepton and a neutrino, while the other W boson decays hadronically into two jets.

Similar to the WW model, the WZ model (Figure 2.3 b) describes the pair-production of charginos and neutralinos. The second-lightest neutralino decays into a Z boson and a the LSP and the lightest chargino decays into a W boson and the LSP. As for the WW model the LSPs escape the detector while the W and Z bosons decay into SM particles. The W boson decays leptonically into a lepton and a neutrino, while the Z boson decays hadronically into quarks. Results for both models have been published in the 2 and 3 lepton channel (19, 20) and the 0 lepton is studied as well within ATLAS.

Chapter 3

LHC and ATLAS

In this section the Large Hadron Collider (LHC) (21) and the ATLAS detector (22) are described.

3.1 LHC

The LHC (21) is the largest accelerator and collider in the world in which protons collide with a centre-of-mass energy of up to 13 TeV (24). Generating such high energies with a single accelerator would be an unrealistic task from a technical standpoint. Instead a system of pre-accelerators, mostly formerly used accelerators at the CERN facility, accelerate the protons to higher energies from which they are induced in the LHC and accelerated to the maximum centre-of-mass energy. Four large experiments are located around the ring of the LHC. Figure 3.1 shows the accelerator complex at CERN.
Starting from a single hydrogen source, bunches of protons are filled into the Linac2 accelerator. A bunch can be understood as a package of $1.15 \cdot 10^{11}$ (25) protons while 2556 (25) of these are running simultaneously through the LHC. Protons are filled into the Proton Synchrotron Booster (BOOSTER) with an energy of 50 MeV. In the BOOSTER the protons are accelerated to an energy of 1.4 GeV. In the Proton Synchrotron (PS) the protons are accelerated to an energy of 26 GeV, from which they are injected into the final pre-accelerator the Super Proton Synchrotron (SPS) and then into the LHC with an energy of 450 GeV. During their time in the PS protons are ordered in bunches. Along the beam pipe of the LHC, with its circumference of 27 km, 1232 superconductive dipole magnets are placed, generating a magnetic field strength of about 8.3 T. Furthermore, the bunches itself are located in two separated beam pipes travelling separated from each other for most of the time. At eight interaction points the proton beams can be brought to collisions. The four experiments ATLAS, ALICE, CMS and LHCB are located at four of these interaction points. In close proximity to a collision point both beams are focussed before colliding in the centre of the detectors.
Designed for a centre-of-mass energy of 14 TeV (24) the LHC started operation in 2009 running with $\sqrt{s} = 7$ TeV from 2010 to 2011 and $\sqrt{s} = 8$ TeV in 2012. After a long shutdown from 2013 to 2014 the LHC started running again with $\sqrt{s} = 13$ TeV during the so called Run 2 from 2015-2018. As consequence of the number of protons in a bunch, additional proton-proton collisions can occur in addition to the hard primary collision. The additional inelastic collisions are called pile up. During Run-2 the number of inelastic interactions per bunch crossing varied from 14 to 43 (26).

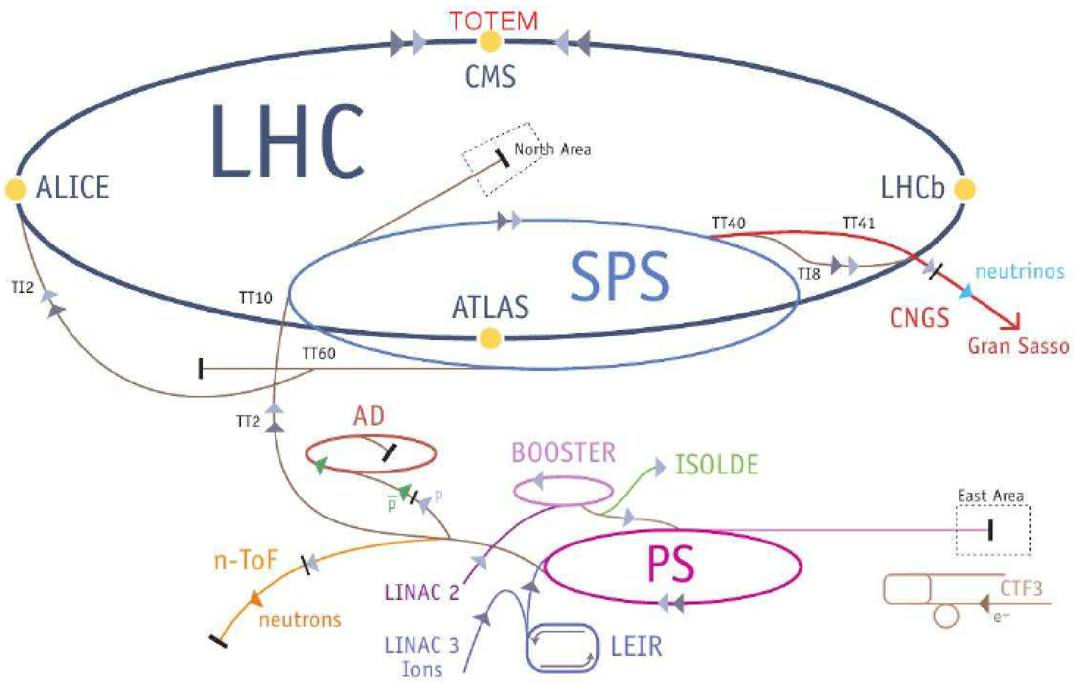

Figure 3.1: Accelerator complex at CERN (23)

3.2 The ATLAS detector

The ATLAS detector is located at point 1 of the LHC. The detector itself is a multi-purpose detector, which means that it is not specialised to a specific process to be measured. Figure 3.2 shows a schematic layout of ATLAS. The detector has a total size of about 44 m in length and 25 m in height. ATLAS is composed of subdetectors located either cylindrically around the beam axis, or in end caps, which are located perpendicular to the beam axis.

3.2.1 Coordinate system describing ATLAS

Particles collide in the centre of ATLAS, therefore the origin of a right-handed Cartesian coordinate system can be placed at this point. Moreover, the x-axis points towards the centre of the LHC ring, the y-axis points upwards. The z-axis points in the beam direction. Another definition, used to describe the directions particles travel in the detector, is the definition of an azimuthal angle ϕ, which is defined as the angle around the beam axis. Furthermore, η, the pseudorapidity is defined as $\eta = -ln(tan(\frac{\theta}{2}))$, while θ is defined as the polar angle measured with respect to the beam axis. Both variables are used to define distances between objects in the detector $\Delta R = \sqrt{\Delta\eta^2 + \Delta\phi^2}$. The second coordinate definition is more beneficial since the ATLAS detector has the shape of a cylinder.

3.2.2 Subdetectors

Inner detector (ID)

Located closest to the beam pipe, the inner part of the Inner Detector (ID) (28) consists of semiconductor pixel and silicon microstrip detectors. In the outer part the Transition Radiation Tracker (TRT) (29) is located, which consists of straw-tube detectors. Additionally, the ID is enclosed by a magnetic field with a field strength of 2T. Due to the Lorentz force

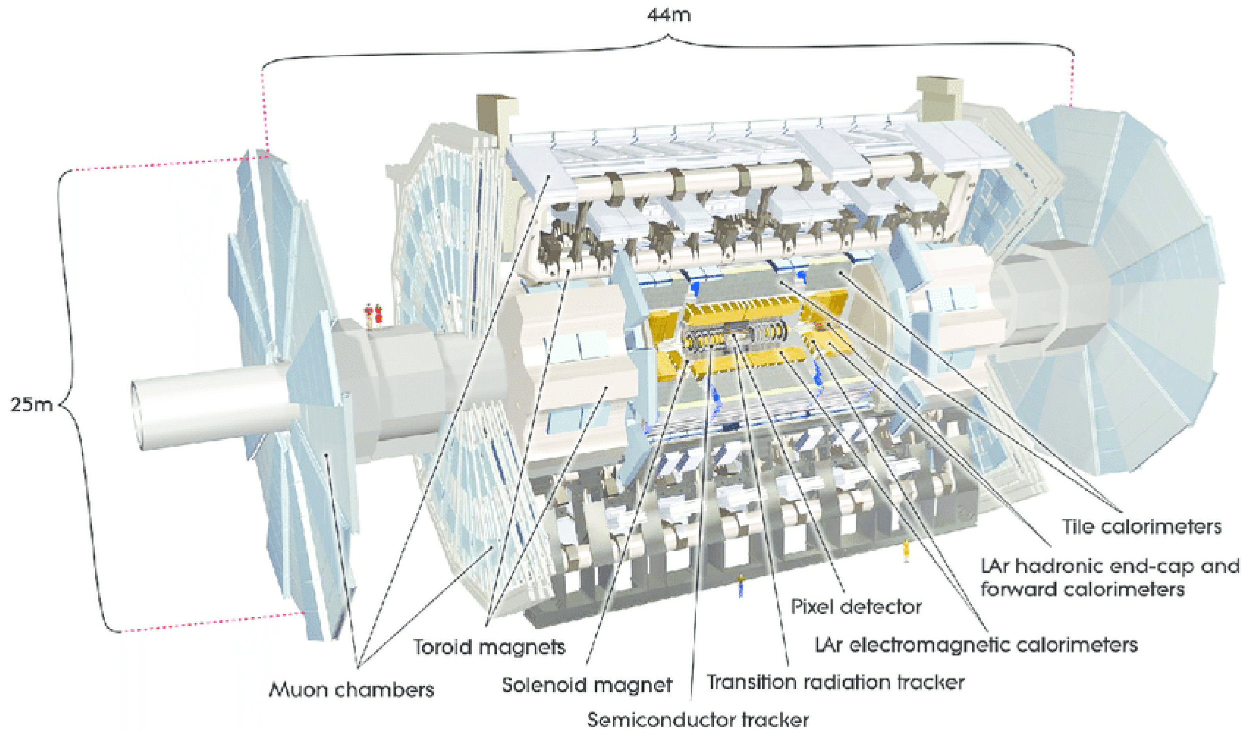

Figure 3.2: Schematic layout of the ATLAS detector (27)

induced by the magnetic field, tracks of charged particles will be curved and a momentum measurement thus possible. Neutral particles will not leave a track in the ID. This information is used in the reconstruction combined with measurements in following detector parts. Measurements in the ID are used to reconstruct the momentum of charged particles, as well as their electrical charges.

Calorimeter

ATLAS uses two types of calorimeters (30, 31):
1. Electromagnetic calorimeter (ECAL) which is used for measuring electromagnetically interacting particles
2. The hadronic calorimeter (HCAL) that is used to measure strongly interacting particles

Calorimeters are used to absorb particles and measure the resulting energy deposits. In order to stop high energetic particles calorimeters are built up of dense materials designed to be highly interactive with particles travelling through the calorimeter. This is also called a disruptive measurement. Generally speaking, calorimeters measure the energy of the charged secondary particles that are produced during the interaction between the initial particle with the detector material. These cause a shower signature in the calorimeter. The resulting signature is then measured as an energy cluster in which a combination of all secondary particles and fragments of the initial particle will be combined to recreate properties of the initial particle. Both calorimeter types are built up in the form of a sandwich structure, which is composed of a passive and an active material. Passive materials are primarily used as absorbers. On the other hand active materials are used for the actual measurement of the calorimeters and are the only parts of the detector that give information about the energy deposited by particles travelling through the calorimeters.

In the ECAL particles interacting through the electromagnetic force are stopped (electrons and photons). These particles will display a shower structure based on two subprocesses, the Bremsstrahlung and pair production. The energy deposits resulting from secondary particles are then measured by the ECAL (30).

Surrounding the ECAL is the HCAL, which primary purpose is the measurement of hadronic showers caused by particles such as protons, neutrons, pions etc. In addition to the shower patterns caused by the strong interaction in the HCAL, one would expect an electromagnetic component as well. Electromagnetic interactions in the HCAL are caused by the charge of the initial or secondary particles.

Muon chamber

The muon system (32) is enclosing the ID and calorimeters. Its primary usage is the measurement of tracks originating from a muon candidate. The muon system consists of several separate detector types and is enclosed by a separate magnetic field. The Monitored Drift Tube (MDT) (33) in combination with track measurements in the ID is used to determine the momentum and charge of a muon. MDTs are used in the central detector region, but at large rapidity η cathode strip chambers (CSC)(34) become more beneficial for the reconstruction of muons. Additionally, two different detector types are used for triggering muons: Resistive Plate Chambers (RPC) (34) in the barrel regions and Thin Gap Chambers (TGC) (35) in the end-caps. The CSC and MDT are used for the track reconstruction muons, due to their superior spatial resolution compared to the RPC and TGC. The latter two are used for fast reconstruction that give information for the triggers.

3.3 Trigger system

During runtimes the LHC collides particles with a rate of 40 MHz. Experiments like ATLAS aim to record the maximal amount of useful data that the LHC provides them. Due to finite resources, it is not feasible to record every collision. In fact ATLAS reduces the event rate to 1 kHz of events that are being recorded. Therefore the question arises of how to select collisions and how to identify events that are interesting for a broad spectrum of physics analyses. In order to find a solution to this problem, the trigger system (36) is used. The basic concept relies on the idea that every initially recorded event will be reconstructed using a fast reconstruction algorithm called level-1 trigger. This is a hardware based trigger using a subset of detector information which then is used to reduce the event rate to 100 kHz. The high-level trigger (HLT) is a software based trigger that leads to a reduction of the event rate to 1 kHz. On a basic level the high-level trigger receives the events of the L1 trigger and does a more detailed reconstruction of the objects in the events. These reconstructions are then used to choose the most interesting events.
Several types of triggers are used, that are optimized on a variety of signatures, i.e. a trigger on the signature of a high energetic isolated lepton.

3.4 Particle identification

This section will focus on the particle identification and reconstruction using the ATLAS

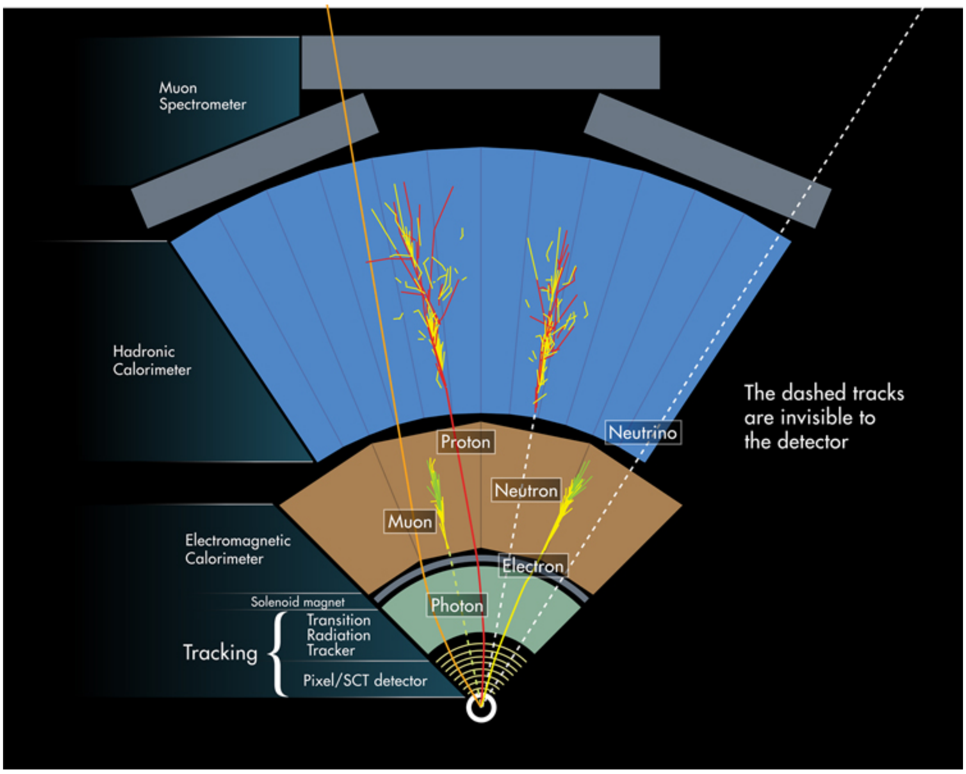

Figure 3.3: Display showing the interaction of a given set of particles with the various components of the ATLAS detector (37)

detector.

Electrons

Electron candidates are reconstructed based on measurements from the ID and ECAL. The signature of an electron is characterized by a charged track in the ID and a cluster of energy deposits matched to an electron candidate in the ECAL (38). In the ID electrons are expected to show a curved track, due to their electrical charge. Exiting the ID, tracks associated with electrons that are travelling through the central region, which is defined as the region of the detector for which $|\eta| < 2.47$, are reconstructed from the measurement of energy deposits with a threshold of 2.5 GeV in the ECAL. In addition a requirement on the matching of tracks and clusters in the η x ϕ space is used. The basic idea is to investigate the proximity in the η x ϕ space of these energy deposits and sort out signatures not belonging to the electron or the double counting of a single calorimeter cell.

Muons

Muons (39) are charged particles, therefore they can leave tracks in the ID and the MS. The information given by the measurement of the ID and MS can then be supplemented with additional information from the calorimeters. However, interactions between muons and the calorimeters are suppressed, which is why most measurements of muon candidate are not using the calorimeters. A more beneficial idea is to concentrate on the measurement of the MS, since muons are the only particles entering the MS. Four types of reconstructed muons are considered in ATLAS:

1. Combined (CB) muons: Independent track measurements in the ID and MS are combined

for the reconstruction of a muon.
2. Segment-tagged (ST) muon: Tracks from the ID are associated with more than one track in the MDT or CSC.
3. Calorimeter-tagged (CT) muons: Tracks of a muon candidate in the ID associated with an energy deposit recorded in the ECAL are reconstructed. These kinds of muon candidates are expected to yield low energetic signature.
4. Extrapolated (ME) muons: Only the measurement in the MS is used, where tracks are then required to be registered in at least two layers. The reconstruction of muons using the ME muon identification are beneficial to cover the $2.5 < |\eta| < 2.7$ region, which the ID is not covering.

Quarks and gluons

While leptons can travel through the detector and are detected directly QCD predicts that quarks and gluons cannot travel through the detector as free particles due to them undergoing hadronization (40). Top quarks can be seen here as a special case, because the lifetime of the top quark is too short for them to enter a bound state. The hadrons may have a short lifetime and might decay further in secondary particles. These secondary particles might then have short lifetimes as well. Further iterations of this process can lead to a cluster structure containing a variety of secondary particles referred to as a jet. Due to its electromagnetic components a jet is expected to show a track in the ID. During the hadronization process leptons and other charged particles can be produced, which then could interact with the ECAL. Eventually the jet is expected to be stopped in the HCAL.

Neutrinos

Neutrinos only interact via the weak interaction, therefore they do not interact with the detector.

3.5 Object definitions

Chapter 3.4 described the typical signatures associated with a certain kind of particle in the ATLAS detector. When an event passes the criteria defined in the previous section the recorded signatures can be linked to potential particle hypotheses. Certain criteria are applied, to identify particles in the collision events. The criteria depend here on the phase space the analysis is interested in, and thus different working points are used in the identification of particles.

Electron

Chapter 3.4 explained how electrons are measured in the detector. The analysis requires that electron candidates pass the loose identification criteria. (41). The loose identification criteria set requirements on the number of hits in the ID and restrict the width of particle showers in the ECAL. In the analysis two kinds of electron types are used. Table 3.1 shows the selection criteria used to define a baseline and signal electron. In context of the analysis, baseline leptons, meaning electrons and muons, are used to calculate the missing transverse energy. Leptons passing the overlap removal (described in chapter 5.3) are required to pass the 'signal lepton' criteria.

Table 3.1: Electron baseline and signal definitions

Variable	baseline electron	signal electron
p_{T}[GeV]	> 4.5	> 7
η	< 2.47	< 2.47

Another criterion regarding signal leptons is that they are required to occur in isolation. Meaning that the signature of an electron candidate does not overlap with tracks from charged particles in the ID and energy deposits from other particles in the ECAL. Therefore, the electron is required to satisfy a set of p_{T} based isolation criterium. How lepton isolation criteria are defined in ATLAS can be seen here (42).

Muon

Chapter 3.4 illustrated the signature expected of a muon and the ways, muons are reconstructed by ATLAS. Baseline and signal muon definitions are shown in table 3.2. Additionally to reduce the rate of particles misidentified as muons requirements that $\frac{d_0}{\sigma(d_0)} < 3$ and $z_0 sin(\theta) < 0.5$mm are used.

Table 3.2: Muon baseline and signal definitions

Variable	baseline muon	signal muon
p_{T}[GeV]	> 3	> 6
η	< 2.7	< 2.7

' As for electrons muons have similar isolation criteria, which are described in (43).

Jets

Chapter 3.4 detailed the nominal signature a jet displays in the ATLAS detector. The information measured by the ATLAS detector is reconstructed using the anti-k$_t$ algorithm (44). The anti-kt-algorithm combines cluster that are geometrically "close" to each other into a jet. Distances between two reconstructed objects are defined as d_{ij}:

$$d_{\mathrm{ij}}^2 = min\left(\frac{1}{p_{\mathrm{T_i}}^2}, \frac{1}{p_{\mathrm{T_j}}^2}\right)\frac{(\Delta R)_{\mathrm{ij}}^2}{R^2} \tag{3.1}$$

$p_{\mathrm{T_{i,j}}}^2$ are defined as the square root of the transverse momentum of the cluster. Clusters are understood as a three-dimensional energy deposits in the calorimeters. The algorithm starts with a single cell, that recorded an energy deposit above a certain threshold. In the next step neighbouring cells in the calorimeters with comparable energy signatures are gathered in a cluster.

This uses a distance measure $(\Delta R)_{\mathrm{ij}}^2 = (\eta_{\mathrm{i}} - \eta_{\mathrm{j}})^2 + (\phi_{\mathrm{i}} - \phi_{\mathrm{j}})^2$. The free parameter considered in the equation, R, that symbolizes a measure for the opening angle of the jet cone. Therefore, R (44) is sensitive to the energy measurement of a jet. Moreover, if the value of R would be too small, potential energy deposits can be cut off and not considered in the reconstruction leading to a potential source of missing energy. On the other hand, the case of defining an R value that is too large can include energy deposits that do not come from the initial jet leading to a mismeasurement of the jet properties. Two different definitions of jet collections using different R parameters are studied in the analysis. First, the case of a small-R jet, which is defined with an R value of 0.4 and reflects the standard definition of a jet in ATLAS. Second, a large-R jet that is defined with an R value of 1.0 is used in the reconstruction of boosted signatures, which will be defined in chapter 7.1.

Table 3.3: Small and large R jets definitions

Variable	small R jet	large R jet
p_{T}[GeV]	> 20	> 200
η	< 2.8	< 2.0

Missing transverse momentum

Chapter 3 illustrated the circumstances under which particles can escape the detector, which are referred to as real sources for missing transverse momentum, or energy deposits are reconstructed inefficiently in the calorimeters leading to so-called fake missing transverse momentum. If looking for signatures that contain missing energy only the transverse plane of the detector is accessible. This is because, while the LHC accelerates protons, the collision itself is between the respective partons. Therefore, it is not possible to retrace the fraction of the momentum that the colliding partons had at the moment of the collision. For the subsequent measurement of the missing transverse momentum, a summation over the transverse momenta of all reconstructed objects associated with the event is performed. In addition, all tracks originating from the primary vertex that are not matched to a particle are included in the track soft term (TST). The missing transverse energy E_T^{miss} is calculated from the E_x^{miss} and E_y^{miss} component. First the respective $E_{x,y}^{\mathrm{miss}}$ components are calculated:

$$E_{x,y}^{\mathrm{miss}} = \sum_i E_{x,y}^{\mathrm{miss,i}} + E_{x,y}^{\mathrm{miss,TST}} \tag{3.2}$$

In equation 6.2 the sum is used over all particles that are included in the calculation of E_T^{miss}. Eventually E_T^{miss} is defined as the absolute value of E_x^{miss} and E_y^{miss}:

$$E_{\mathrm{T}}^{\mathrm{miss}} = \sqrt{(E_{\mathrm{x}}^{\mathrm{miss}})^2 + (E_{\mathrm{y}}^{\mathrm{miss}})^2} \tag{3.3}$$

Chapter 4

Monte Carlo and background processes

4.1 Measuring data with ATLAS

A way to determine the number of events recorded by ATLAS is given by the product of the integrated luminosity $\mathcal{L}$ (45) and the total cross section σ

$$N = \sigma\mathcal{L} = \sigma \int L dt \tag{4.1}$$

Data considered for this analysis was taken from 2015 to 2018 with a centre-of-mass energy of 13 TeV during Run-2 (45). This corresponds to a recorded integrated luminosity of $\mathcal{L} = 139$ fb^{-1} (26). Actually the LHC has provided and ATLAS has measured more than the recorded luminosity, but when taking the restriction on the data quality (46) into account about 95% of the data recorded is classified as usable for an analysis.

4.2 Monte Carlo

All results shown in this analyses are blinded, which means that the analysis is not performed by studying data during the optimisation in regions were potential signal events are expected. The analysis in this work uses simulations of ATLAS data produced with Monte Carlo methods. Using simulated data is an important tool when searching for signatures beyond the SM. Simulated data is based on theoretical calculations and reflects the data ATLAS measures. The analysis uses simulated data because an optimisation using real data could become biased on the potential signal model signature. Another case could arise when the analysis becomes sensitive to fluctuations in the kinematic region of the data. Since the analysis targets kinematic regions with low expected event numbers which are usually located in more remote regions of the phase space a perfect modelling of the physics in these regions cannot be expected. Only when an analysis can show that the defined search regions are well modelled by the simulated data the use of unblinded data is allowed.

4.2.1 Simulating data with Monte Carlo methods

Monte Carlo simulations (47) are used to predict the properties of an event as if recorded by ATLAS. Any process of interest to the analysis is simulated beginning with the hard scattering up to the electronical signal recorded by the detector.

First, the hard collision of two partons is simulated. The decays of the resulting hard particles are simulated. Additional radiation from the initial-state or final-state is considered up to the corresponding order. Following these steps, the hadronization of the decay products is simulated. Finally, the underlying event and decays of unstable particles are generated. Afterwards for every generated event, the interaction with the ATLAS detector is simulated (48).

4.2.2 Standard Model backgrounds

Referring back to the signal models introduced in chapter 2.6. Signatures displayed by both models in the detector include two jets, one lepton and missing transverse energy (explained in chapter 3.5) In the following, SM processes that are expected to yield similar final states are presented. These processes are referred to as background events. Background processes of this analysis are presented in figure 4.1, and are characterised as SM processes that yield similar final state signatures as the proposed signal models. On a general note the selection of background processes focuses on a potential final state including one lepton coming from a W boson decay, two jets coming from a hadronically decaying weak gauge boson. All SM processes, that are shown in figure 4.1 and used in the later chapters have shown to be contributing factors in previous analysis of the 1 lepton channel in similar models (49). SM background processes can be ordered in two categories:
1. Reducible backgrounds are expected to yield similar signatures as the signals, when the initial event is misreconstructed.
2. Irreducible backgrounds are expected to yield an almost identical signature as the signal processes.

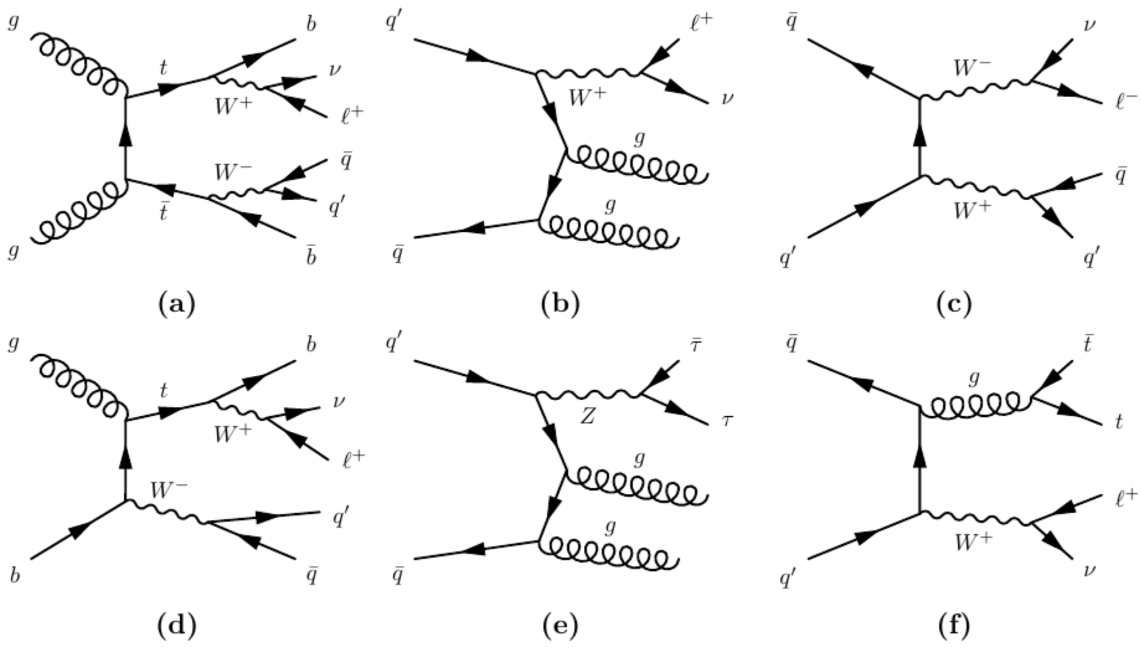

Figure 4.1: a) $t\bar{t}$, b) W+jets, c) Diboson, d) Single top , e) Z+jets, f) $t\bar{t}$+V (50)

$t\bar{t}$

A process that is expected to be a main background for both signal models is given by the semileptonic decay of a $t\bar{t}$ pair. $t\bar{t}$ is characterised as reducible background, because in addition to the semileptonically decaying W boson pair two b jets are produced. On tree-level $t\bar{t}$ this would give a total of four jets in the event. Compared to the expected signatures of the signal models, introduced in chapter 2.6. Both models have two jets in their final state, while b quarks are kinematically forbidden in the WW model and have only a small branching fraction in the WZ model. Therefore, the two b jets would most likely have to be mismeasured. Despite the fact that two b jets would have to be misidentified, $t\bar{t}$ events are one of the main backgrounds of the analysis, due to the relatively high cross-section at the LHC in comparison to the potential signal models.

W+jets

W+jets defines a class of signatures in which a W boson is produced in association with additional jets. These jets can then be ordered in categories of light jet flavours, jets coming from c quark and heavy flavour jets. If looking for a 1-lepton final state, the W boson is required to decay leptonically into a lepton and the corresponding flavour-matching neutrino. Searches for final states containing a lepton would neglect the contributions given by hadronically decaying W bosons, because these cases would require the case of a fake lepton. Fake leptons could arise from mismeasurements in the detector. An example is given by a jet misidentified as an electron. In comparison, muons have a significantly lower probability of being misidentified as a jet.

Diboson

Diboson describes the production of an electroweak gauge boson pair. There are three potential signatures: WW, WZ and ZZ. Comparing these to the proposed signal models introduced in chapter 2.6, one sees that diboson can yield very similar final state signatures. Thus, diboson is regarded as an irreducible background in context of the analysis. A significant difference between a diboson process and the signal models is that in the SM only the neutrino is expected to escape the measurement of the detector, while in the signal model the LSP results into an increased $E_{\mathrm{T}}^{\mathrm{miss}}$.

Single top

Figure 4.1 d) shows the signature given by the Wt single top decay channel. In the Wt-channel a top quark, which decays further decay into a W boson and a b quark, is produced in association with a W boson. One potential decay mode, that is expected to yield a similar final state as the signal models is given by the semileptonic decay of the two W bosons. However, in this scenario the jet coming from the b quark would then have to be misidentified or lost in the reconstruction of the event. For this analysis the Wt-channel is regarded as the dominant channel since the production of a single top event using the s-channel and t-channel are neglected. Both production channels can be seen in (51). For the s-channel a signature with one b jet and a top quark is expected. Then the top quark would decay into a b quark and a W boson, which then would decay leptonically. In comparison to the signal models the s-channel would include two b quarks in comparison to the two lighter quarks in the WW model. As for the WZ model a similar signature can be seen, when the Z boson decays into two b quarks, but the two quarks in the signal event are expected to give the invariant mass of a Z boson. This would then be used to discriminate from the s-channel. As for the t-channel, which is also expected to yield a final state signature that includes two b jets, an additional third jet and a leptonically decaying W boson. One can use the identical argument as for the s-channel. Compared to the dominant production of $t\bar{t}$, single top processes have a lower cross section and are thus less important in this analysis.

Z+jets

Z+jets describes the production of a Z boson in association with additional jets. A possible diagram is illustrated in figure 4.1 e). A Z boson is produced and decays into two leptons, of which one could be misidentified. In addition to the production of the Z boson a jet pair can be produced, yielding a final state similar to the signal models.

$t\bar{t}$+V

Resulting in a similar final state as both signal models, the production of a $t\bar{t}$ pair in association with a boson is a reducible background in the same way as $t\bar{t}$. A potential diagram is shown in figure 4.1 f), where the W boson decays leptonically and the top quark pair could decay fully hadronically. In a similar way as single top, $t\bar{t}$+V processes have a lower cross section compared to the production of a $t\bar{t}$ event, and are therefore less important in this analysis.

4.3 Overview of simulated SM samples used in the analysis

As it has been explained in the previous section, the basis for the analysis is the simulation of a variety of SM processes. Therefore, an overview of the SM background and signal models considered in the analysis is given in table 4.1.

Table 4.1: Simulated Monte Carlo samples

Simulated physics sample	Generator	PDF	Parton shower
$t\bar{t}$	Powheg-Box v2(52)	CT10 NLO (53)	Pythia 8 (54)
Single top	Powheg-Box v1/v2	CT10f4 NLO	Pythia 8
W+jets	Sherpa 2.2.1(55)	NNPDF3.0 NNLO (56)	Sherpa(57)
Z+jets	Sherpa 2.2.1	NNPDF3.0 NNLO	Sherpa
Diboson	Sherpa 2.2.1/2.2.2	NNPDF3.0 NNLO	Sherpa
$t\bar{t}$+V	Powheg-Box v2	NNPDF2.3 LO	Pythia 8
Signal WW/WZ	MadGraph5(58)	NNPDF2.3 LO	Pythia 8

The generator in table 4.1 refers to the MC generator used for the production of the given process. PDF refers to the Parton Distribution Function which describes the distribution of the partons in a hadron depending on the fraction of the hadron momentum carried by a parton. The entries in the list refer to set of PDF used in the generation process of the sample. As an example, the first entry describes a PDF set based on CT10 that describes the PDF up to the NLO (next-to-leading order).

Chapter 5

Event cleaning

Chapter 3 presented the design up of the ATLAS detector and the methods used to identify particles. Measured data taken by the experiment is influenced by effects arising from mismeasurements and mis-modelling. In context of the analysis, it means that the analysis applies a certain set of cleaning criteria on the recorded events. One example would be that if individual detector parts are temporarily non functional and events falling into this time period are discarded.

5.1 Data quality

Accommodating for problems with detector measurements during a luminosity block, usually corresponding to a data taking time of 1-2 minutes, events are removed if at the time of the recording the detector or parts of the detector were malfunctioning. This affects data only.

Primary vertex

In ATLAS, the primary vertex is defined as the vertex associated with the highest $\sum p_T^2$ (tracks). At least two tracks in the event with $p_T > 400$ MeV are required to be traced back to the vertex. Requirements relating to the primary vertex are used to reduce pile-up.

Bad muon veto

To reject mismeasured muons, events containing a so-called bad muon are rejected. A bad muon is defined as a muon candidate that satisfies $\frac{\sigma(q/p)}{|q/p|} > 0.2$. q is the charge, p the momentum of the muon and $\sigma(q/p)$ the uncertainty regarding measurement of $|q/p|$.

Cosmic muon veto

Due to the relatively long lifetime and relativistic effects, muons created during the interaction of high energy cosmic rays with the earth's atmosphere can enter the ATLAS cavern and pass through the detector. In comparison to events containing muons that originate from a collision in the ATLAS detector, cosmic muons are expected to have values of $d_0 > 0.2$ mm and $z_0 > 1$ mm with respect to the primary vertex. Here d_0 and z_0 are defined as the transverse and longitudinal impact parameters. The distance from the primary vertex in the x-y-plane is given by d_0 and z_0 describes the distance in z direction to the primary vertex.

Bad jet veto

Environmental factors like cosmic rays, noises in the detector or signatures in the detector arising from protons that have been removed during the beam cleaning (59) provide an additional source of background. For example, during the beam cleaning an interaction with the collimators (60) could yield signatures similar to jets.The LooseBad cleaning criterium is applied

5.2 b-tagging

Signatures given by jets that are originating from b quarks have distinct properties. These properties can then be used to distinguish them from jets originating from different quark flavours. In order to distinguish jets originating from b quarks from other flavour jets a tagging algorithm is used. b quarks are likely to go into bound states called B-hadrons. Because the decay of B-hadrons is suppressed by the CKM matrix element (61), they have longer lifetimes than hadrons affiliated with lighter jets. Thus, the signature of a b quark can be distinguished from a lighter quark by measuring the primary and corresponding secondary vertex of the decay of the B-hadron.
In this analysis the MV2c10 algorithm (62) is used to tag b jets. MV2c10 is based on a boosted decision tree (BDT) (63) and is primarily trained to discriminate between jets originating from b and c quarks. Variables used for the tagger are the $\mathrm{Jet}_{\mathrm{p_T}}$ and $\mathrm{Jet}|\eta|$. The actual criteria depend on the efficiency point.
The analysis uses a b-tag efficiency of 77% using the additional requirements listed in table 5.1.

Table 5.1: b-tagging acceptance requirements

Variable	b-tagging acceptance
p_{T}[GeV]	> 20
η	< 2.5

5.3 Overlap removal (OR)

One possible source leading to a contamination of the measured signature in the detector is given by cases, in which the measured signatures of two particles overlap. An example would be the case of a jet which energy deposits in the calorimeter overlap with the ones coming from an electron. The particle identification needs to distinguish between the energy deposits of the two particles. Overlapping signatures could yield in a double counting of energy deposits in the detector. The analysis uses a selection of criteria designed to handle problems originating from overlapping particles.
Overlap removal is applied on a step-by-step basis (64).

- Cases depicting two electrons that the reconstruction algorithm assigned the same track in the ID are resolved by discarding the electron with lower transverse momentum.

- In cases where electrons and muons share the same tracks in the ID the electron is removed.

- Jets that are not b-tagged in a distance of $\Delta R < 0.2$ with respect to an electron are removed.

- Electrons are rejected if closer than $\Delta R = \min(0.4, 0.004 + 10\ \mathrm{GeV}/p_{\mathrm{T}})$ to a jet.

- Non-b-tagged jets are rejected if overlapping with a muon candidate within $\Delta R < 0.2$ or when on an earlier stage of the reconstruction the muon has been matched to the same jet when using ghost association.

- When a muon overlaps with a jet with $\Delta R = min(0.4, 0.004 + 10GeV/p_T)$ it is removed.

Chapter 6

Statistical data analysis

Experiments like ATLAS are collecting large amounts of data. Analysing the amounts of data recorded by ATLAS can only be done by using techniques from the field of statistical data analysis. This chapter introduces methods commonly used to interpret data in SUSY searches. Descriptions given in this chapter are based on (65).

6.1 Significance and p-value

The analysis searches for potential signatures that have been motivated from a theoretical point of view, but have not been observed yet. The agreement of the data with the SM expectations of with the presence of a BSM signal is assessed via e.g. calculating p-values. In order to do so, two hypotheses are compared to data in a hypothesis test. A common strategy is to determine the significance by calculating a p-value.
First, a null hypothesis (H_0) is defined which corresponds to the SM background processes. The null hypothesis is then compared to a hypothesis H_1, which includes in addition to SM processes a signal. A model plus background hypothesis is then evaluated against the only background processes hypothesis. The agreement of the hypotheses with data is studied by calculating a p-value. p-values are a measure for the probability of observing an agreement or an even better result between the measured data, assuming hypothesis H_0 is true. In BSM searches it is used to explain how likely an excess of signal events can be coming from only background processes. Aiming to exclude certain models a hypothesis is defined to be excluded, if the corresponding p-value is below a certain threshold. Actually for the exclusion of certain models confidence level (CL) values are used instead of p-values. CL values are used, because when using p-values cases were the number of signal and background events (s+b) is about equal to the number of background events (b) can be excluded, while there could still be an excess in signal events. Therefore, one uses the $\mathrm{CL_s}$ method (66)

$$CL_{\mathrm{s}} = \frac{p_{\mathrm{s+b}}}{1 - p_{\mathrm{b}}} \tag{6.1}$$

For the applications in particle physics a significance is calculated from the p-value:

$$Z = \Phi^{-1}(1 - p), \tag{6.2}$$

here Φ^{-1} is defined as the quantile of the Gaussian distribution. In the particle physics groups a convention is used that classifies the rejection of a SM background hypothesis with a significance Z = 5.0 as the threshold for a discovery (corresponds to a p-value $p = 2.87 \cdot 10^{-7}$). For the task of excluding signal models $\mathrm{CL_s}$ values are used. For exclusions of a signal hypothesis the threshold is chosen to be a $\mathrm{CL_s}$ value of 0.05 coinciding with a significance $Z = 1.64$. The exclusion threshold is chosen to exclude the hypothesis on a 95% confidence level.

6.2 Fit region definitions

For the fit a set of kinematic regions are used:

Signal regions (SR) are optimised on a set of kinematic variables designed to give the highest possible significance for the signal events.
Control regions (CR) are kinematic regions used to control the main backgrounds and to estimate the dominant backgrounds of the analysis.
Validation regions (VR) are used to validate the background estimation obtained by the CRs. In an ideal view of these regions, CR and VR would be defined so that there are no potential signal events in them.

The task of performing these fits is handeled by a statistical data analysis framework. In this work HistFitter (65) is used to perform complex fits. In later chapters results in the form of exclusion plots will be shown. These exclusion plots are actually simplified shape fits. Which means that only the SRs are used as input for this fit. This means that the background estimation is not handled by CRs and it is assumed that the simulated data represents the kinematic properties of the SR. Systematic uncertainties have not been investigated as well. For them a flat uncertainty was chosen, which value is motivated by looking at the uncertainty calculated by similar analysis.

Chapter 7

Signal Region definition for the WW and WZ model

In chapter 2.6 the WW and WZ models were presented. The following chapters will describe the study of these models. These studies aim to define a set of analysis regions, while in the beginning studies depicting the definition of the SR are presented. Afterwards the background estimation is studied by defining preliminary CR and VR regions.

7.1 Analysis strategy

The analysis is aimed at two types of phase spaces. Definitions of resolved signatures are expected to target regions with medium $m_{\tilde{\chi}_1^\pm}$ values. On the other hand, parts of the phase spaces with high values of $\Delta m_{\tilde{\chi}_1^0-\tilde{\chi}_1^\pm}$ are expected to display signatures more sensitive to boosted cases. Both assumptions are based on the idea, that when a heavy chargino decays into a light neutralino and an electroweak gauge boson, the gauge boson would be more likely to be produced with a higher momentum. This statement relates to the comparison with cases in which the neutralino has a higher mass. Figure 7.1 displays the average number of large R jets plotted for every available signal point for both models. For now a multiplicity in the number of large R jets can be interpreted as a measure for boosted signatures. Moreover the distributions over the signal point display reflects the initial. Meaning that parts of the phase space with high $\Delta m_{\tilde{\chi}_1^0-\tilde{\chi}_1^\pm}$ values show a higher average number of large R jets than regions with lower $\Delta m_{\tilde{\chi}_1^0-\tilde{\chi}_1^\pm}$ values. In context of the analysis the part with high $\Delta m_{\tilde{\chi}_1^0-\tilde{\chi}_1^\pm}$ values will be referred to as the boosted section of the phase space, while the part with lower $\Delta m_{\tilde{\chi}_1^0-\tilde{\chi}_1^\pm}$ values will be regarded as the resolved part of the phase space. Therefore, definition of the SR will concentrate on techniques sensitive to reconstruct boosted and resolved signatures. In order to capitalize on the kinematic properties of the grid two kinds of SRs are defined.
As indicated by the name the resolved region is defined as not using variables that are designed for boosted signatures.

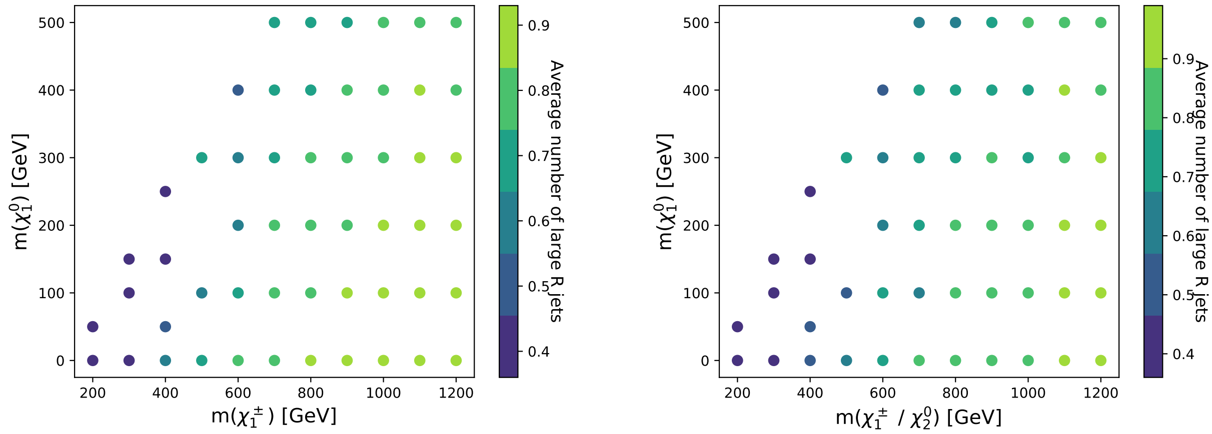

(a) WW model

(b) WZ model

Figure 7.1: Average number of large R jets distributed over the signal point grid

7.2 Variable definitions

7.2.1 Resolved variables

This section will detail the variables used for the design of the resolved SR. Moreover an overlap between the variables used for the two kinds of SR is expected. In which case the variable will only be presented in this section. On a more general note, it would be important at this point to explain the difference between resolved and boosted variables. From a physical standpoint resolved signatures are defined as events in which every jet can be reconstructed independently. Special focus is given to the case of the hadronically decaying boson. One speaks of a boosted signature if it is not possible to clearly separate the two jets coming from the initial boson decay. In these cases, they are called merged and in order to accommodate the problem of reconstructing the two jets, one defines a large R jet. While regular jets, also called small R jets, are defined with an R value of 0.4, large R jets are defined with an R value of 1.0. The basic idea behind the definition of a large R jet is to enhance the probability of reconstructing the full signature displayed by the decay of the merged signature of two jets.

Lepton variables

Since the search is being conducted in the 1-lepton channel one demands only one signal lepton in the SR, only electrons and muons are considered. Aiming for a better discrimination from soft processes and fakes a requirement on the transverse momentum of the lepton p_T^l has shown to be useful.

Number of jets

The decay chain of both signal models includes two jets in the final state. Discriminating from some of the main backgrounds, one would expect that a constraint on the number of jets in an event would be useful in order to decrease the SM background, especially multi-jet backgrounds.

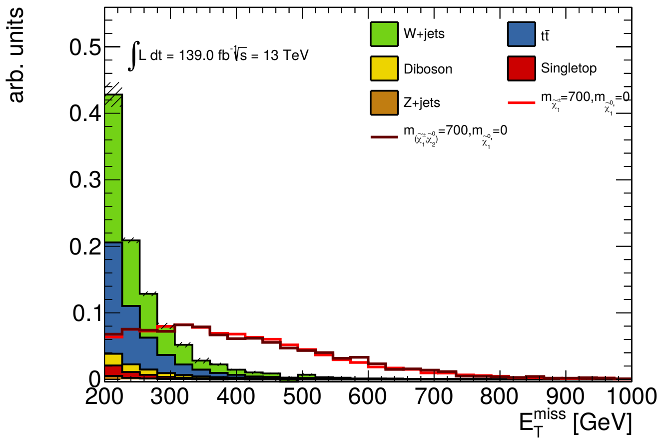
arb. units
∫L dt = 139.0 fb⁻¹ √s = 13 TeV
W+jets
tt̄
Diboson
Singletop
Z+jets
E_T^{miss} [GeV]

(a)

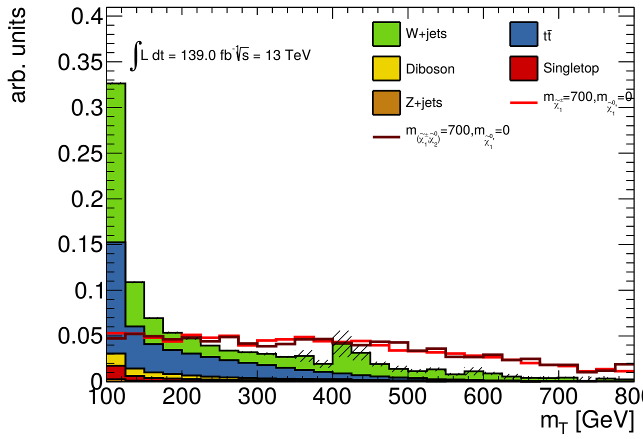
arb. units
∫L dt = 139.0 fb⁻¹ √s = 13 TeV
W+jets
tt̄
Diboson
Singletop
Z+jets
m_T [GeV]

(b)

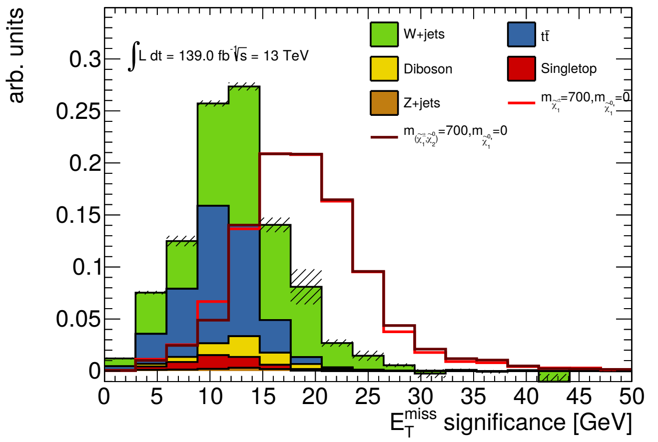
arb. units
∫L dt = 139.0 fb⁻¹ √s = 13 TeV
W+jets
tt̄
Diboson
Singletop
Z+jets
E_T^{miss} significance [GeV]

(c)

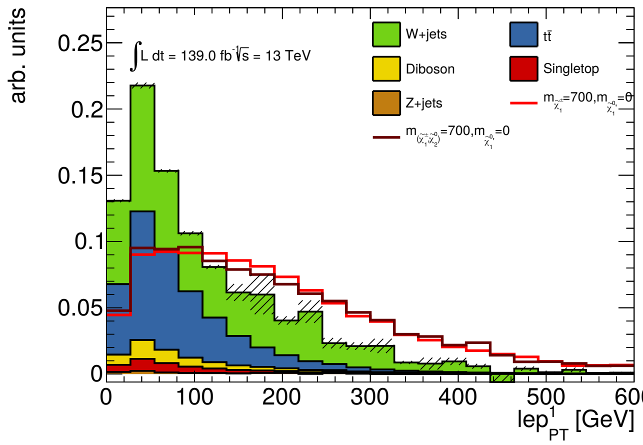
arb. units
∫L dt = 139.0 fb⁻¹ √s = 13 TeV
W+jets
tt̄
Diboson
Singletop
Z+jets
lep^1_{PT} [GeV]

(d)

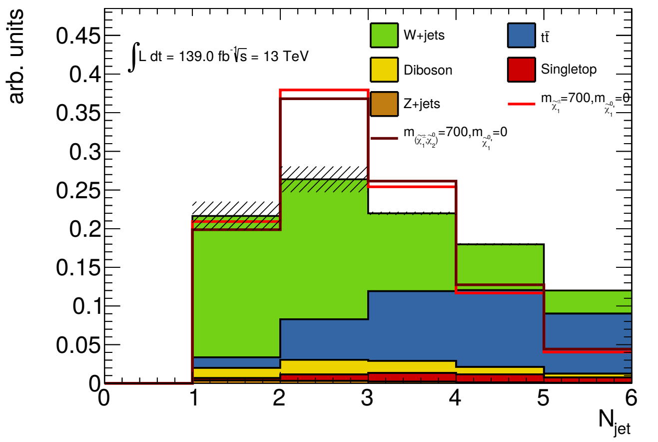
arb. units
∫L dt = 139.0 fb⁻¹ √s = 13 TeV
W+jets
tt̄
Diboson
Singletop
Z+jets
N_{jet}

(e)

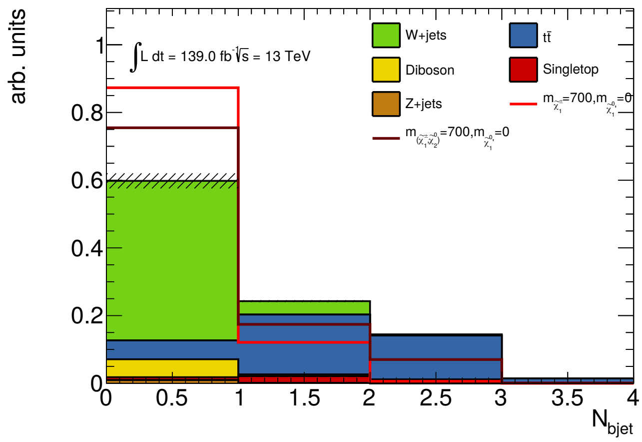
arb. units
∫L dt = 139.0 fb⁻¹ √s = 13 TeV
W+jets
tt̄
Diboson
Singletop
Z+jets
N_{bjet}

(f)

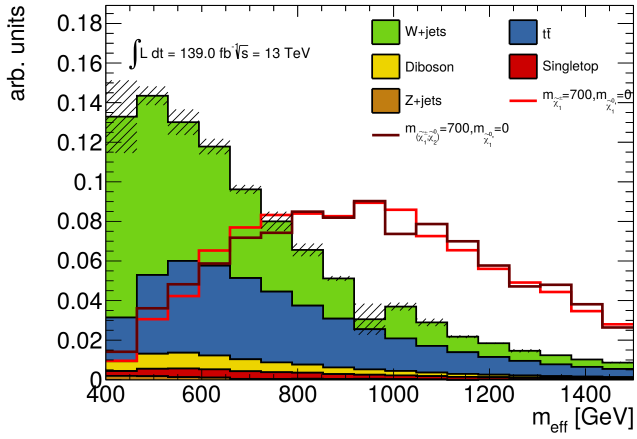

(g)

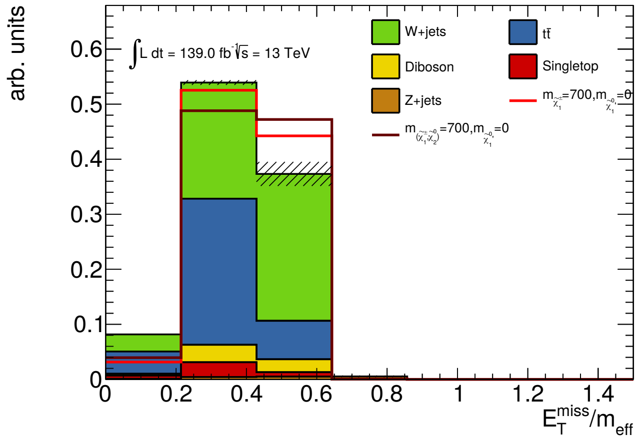

(h)

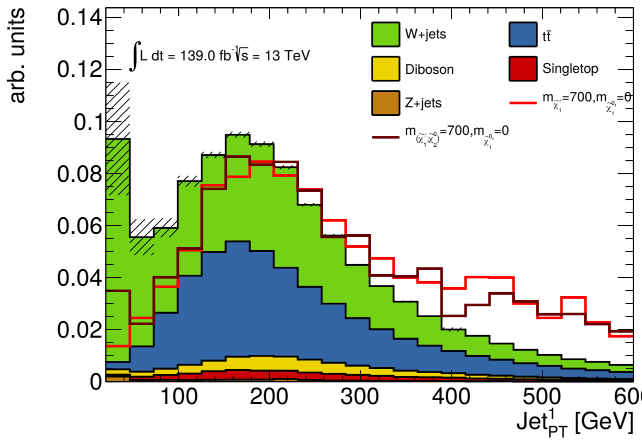

(i)

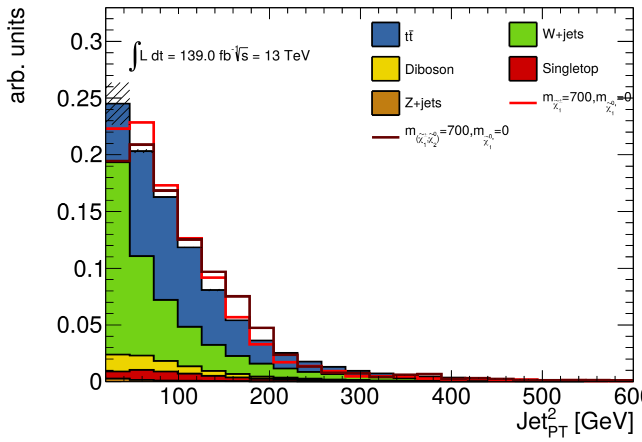

(j)

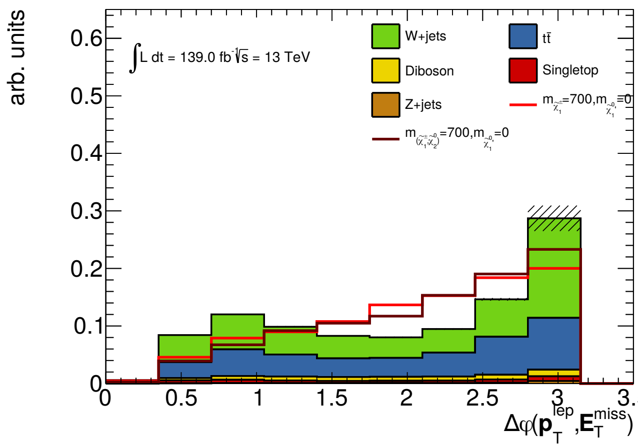

(k)

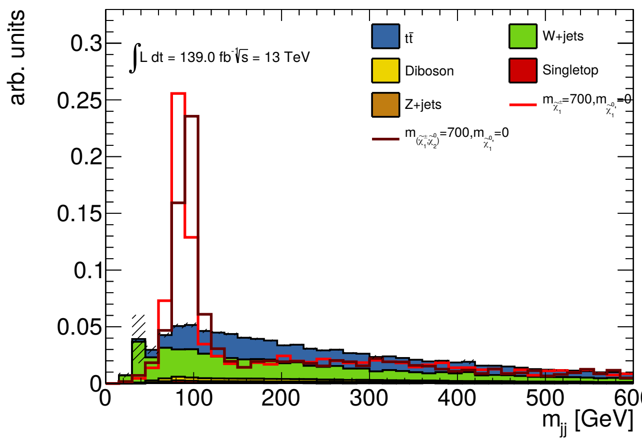

(l)

Figure 7.2: Kinematic distributions of the resolved variables in which the background and signal is independently plotted to a unit area of 1. On all of these plots a set of basic criteria is applied. One demands only one signal and baseline lepton, $m_{\mathrm{T}} > 100$ GeV and $E_{\mathrm{T}}^{\mathrm{miss}} > 200$ GeV.

Number of b-tagged jets

In a similar way, the number of b-tagged jets can be used to discriminate between background and signal hypothesis. Since the production of b quarks is strongly suppressed in the WW model, and is only predicted with a small branching fraction in the WZ model, main backgrounds with a high b jet multiplicity like $t\bar{t}$ can be suppressed.

Transverse mass m_T

m_T is defined as the transverse invariant mass of a leptonically decaying W boson.

$$m_{\mathrm{T}} = \sqrt{2p^{l}_{\mathrm{T}} E^{\mathrm{miss}}_{\mathrm{T}} (1 - cos(\Delta\phi[p^{\mathrm{l}}_{\mathrm{T}}, p^{\mathrm{miss}}_{\mathrm{T}})])} \tag{7.1}$$

Motivating the definition of the transverse mass is the idea that in the SM the main contribution to the missing transverse energy comes form neutrinos and miss measurements of the detector. Therefore the expected kinematic distribution of m_T in the SM peaks around the W boson mass and then falls off. In contrast to the SM, the proposed signal models, which both include a leptonically decaying W boson, include an additional source of real missing transverse energy given by the neutralinos. In Figure 7.2 the kinematic distribution of the SM background and SUSY models is shown. It can be seen that the signal models display a broader distribution of the transverse mass compared to the the SM processes.

Effective mass m_{eff}

An interesting variable for BSM searches is the effective mass m_{meff}:

$$m_{\mathrm{eff}} = \sum_{i} p^{i}_{\mathrm{T}} + E^{\mathrm{miss}}_{\mathrm{T}} \tag{7.2}$$

It is defined as the sum over the momenta of all reconstructed particles in the event and the $E^{\mathrm{miss}}_{\mathrm{T}}$. Since the signal points on the grid go up to masses higher than these expected from SM particles, the m_{eff} distribution of the signal points is expected to peak at higher values. This effect can be seen in figure 7.2 (g).

Angular distance between the lepton and $\mathbf{E}^{\mathrm{miss}}_{\mathrm{T}}$: $\Delta\phi(p^{lep}_{T}, E^{miss}_{T})$

$\Delta\phi(p^{lep}_{T}, E^{miss}_{T})$ is defined as the azimutal angle between the transverse momentum of a lepton and the missing transverse energy.
In comparison to SM processes, which peak at values indicating a back-to-back emittance, signal models are expected to show a more even spread distribution. Both distributions are illustrated in figure 7.2 k).

Invariant mass of a hadronically decaying boson m_{jj}

In the resolved part of the phase space one would expect the signature of a hadronically decaying boson, which decaying products are clearly separated in the detector. m_{jj} describes the invariant mass of the jets coming from the hadronic boson decay. The analysis uses the combination of the leading and sub-leading jets.

$$m_{\mathrm{jj}} = \sqrt{2Jet^1_{P_T} Jet^2_{P_T} [cos(Jet^1_\eta - Jet^2_\eta) - cos(Jet^1_\phi - Jet^2_\phi])} \tag{7.3}$$

As shown in Figure 7.2 (l), the kinematic distributions of the signal models display a sharp peak around the respective boson mass in contrast to the SM background, which only shows a broad peak around the mass range of the electroweak bosons.

Missing transverse energy

A common variable in BSM searches is the missing transverse energy $E_{\mathrm{T}}^{\mathrm{miss}}$. $E_{\mathrm{T}}^{\mathrm{miss}}$ is sensitive to searches including particles that are not expected to display signatures the detector can reconstruct, like neutrinos and lightest neutralinos. Figure 7.2 (a) illustrates the kinematic distributions, in which the proposed signal models are expected to peak at higher values, due to the additional real $E_{\mathrm{T}}^{\mathrm{miss}}$ sources.

Missing transverse energy significance

When looking at potential events in the ATLAS detector, effects driven by the finite resolution of the detector contribute to the missing transverse energy .To accommodate this mismeasurement the missing transverse energy significance has shown to be a useful variable.

$$S^2 = 2ln\left(\frac{max\mathcal{L}(E_T^{miss}|p_T^{inv} \neq 0)}{max\mathcal{L}(E_T^{miss}|p_T^{inv} = 0)}\right) \tag{7.4}$$

The analysis uses the object based missing transverse energy significance definition (67). As a basis for the missing transverse energy significance the expected resolution with respect to the reconstruction of all objects that are used for the reconstruction of $E_{\mathrm{T}}^{\mathrm{miss}}$ are calculated on a event by event basis. Formula 7.4 describes the log-likelihood ratio between the two cases that the measured $E_{\mathrm{T}}^{\mathrm{miss}}$ is real or is caused by resolution effects. In a greater detail, the nominator describes the hypothesis that the missing transverse momentum given by an invisible particle $p_{\mathrm{T}^{\mathrm{inv}}}$ is non-zero, while the denominator depicts the case in which the missing transverse momentum does not arise from invisible particles. From a physical standpoint, high values for the missing transverse energy significance would indicate that the origin of $E_{\mathrm{T}}^{\mathrm{miss}}$ is not from resolution effects. It would therefore suggest that the event contains particles or objects that escape the detector without a signature.

7.2.2 Boosted variables

This section introduces the set of variables sensitive to boosted signatures. Most variables are classified in this category, because they depend on large R jets. Exceptions are given by variables like D_2, these are sensitive to substructure effects relating to boosted signatures.

Number of large R jets

The number of large R jet can be used to separate between events with boosted and resolved signatures. The reconstruction of a large R jet is sensitive to identifying boosted signatures.

Transverse momentum of large R jet

The initial momentum of the hadronically decaying boson is expected to peak at higher values compared to the SM background. The momentum of a large R jets is required to be greater than 200 GeV.

Mass of the large R jet

Another important variable is the mass of the large R jet. In terms of the WW and WZ model, a W/Z boson decays hadronically. If this boson is then boosted, the large R jet is expected to contain their decay products. That way the original mass of the boson can be accessed by using the large R jet mass variable. The measurement of the large R jet mass is used to discriminate between large R jets coming from the boosted decay of a boson and other signatures, which are not expected to yield masses within the defined mass window.

W/Z Tagger

In cases were the hadronically decaying boson is boosted, the idea of defining a tagger sensitive to the boosted signature of a merged W or Z boson is used (68). In general a tagger is a multivariant variable optimised on a collection of variables sensitive to a given kind of signature. The tagger is optimised on the signature of a merged boosted boson signature and uses BDTs and neural networks during the optimisation. For the optimisation a $W' \rightarrow WZ \rightarrow qqqq$ signal sample and a sample of dijet QCD events is used. Both taggers where then optimised using signal jets matched to a truth W or Z boson. These jets are then expected to be within a mass window of [50,100] GeV for W tagging and [60,110] GeV when looking at the Z boson tagging. Two kinds of taggers trained on boosted W boson and boosted Z boson signatures are used. The tagger uses three variables. This tagger is optimized using the mass of a large R jet mass, D_2 and nTrk. Two versions are available for the tagger. One with a 50 % relative signal efficiency and 80% relative signal efficiency. Previous studies by the analysis team indicated, that the use of the 50% efficiency point would be most fitting for both models.

D_2

D_2 is used to identify boosted jets coming from the decay into two charged particles also called two prong decays.

$D_2^{(\beta)} = \frac{e_3^{(\beta)}}{(e^2(\beta))^3}$

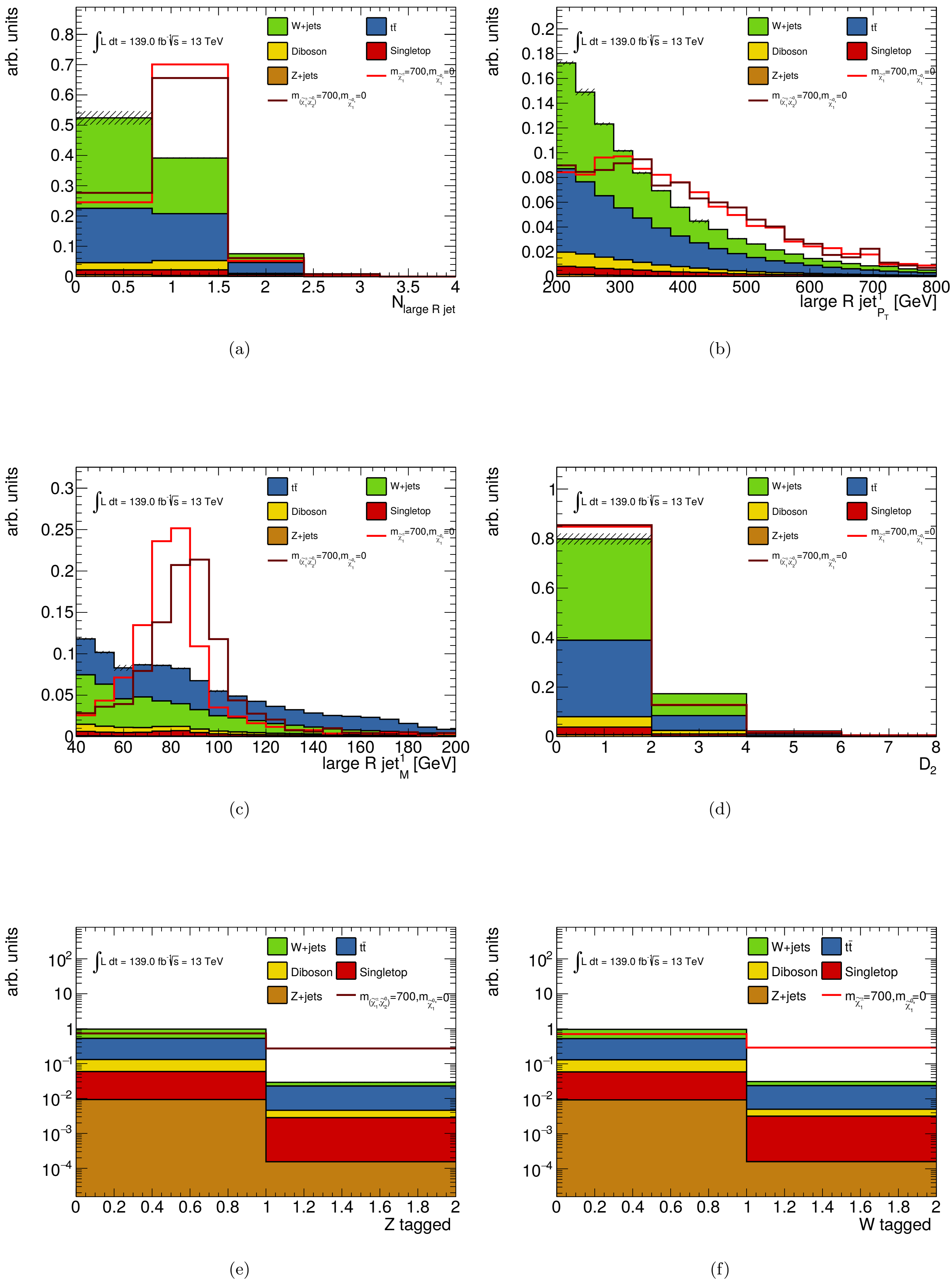

Figure 7.3: Kinematic distributions of the boosted variables in which the background and signal is independently plotted to a unit area of 1

$e_2^{(\beta)}$ and $e_3^{(\beta)}$ are the two- and three-point energy correlation functions, which are used as a probe of the jet substructure (69). Studies (68) have shown that D_2 is one of the most powerful variables when trying to identify the decay of a boosted boson.

Number of tracks

Used for the optimisation of the boosted tagger, nTrk is defined as the number of tracks in the inner detector associated with a jet. Comparing the signatures of a small and large R jet, one would expect that the case of a large R jet will be more likely to show event signatures with more tracks than the case of small R jets. During the optimisation process of the boosted boson taggers, restrictions on the number of tracks has shown to be useful. It is expected, that restriction on the number of tracks are sensitive to larger energy deposition signatures given by heavier boosted bosons.

7.3 Optimisation strategy

The main body of the analysis describes the optimisation process of the respective SR definitions of both models. In the first two steps, a set of kinematic variables with their respective kinematic values will be optimized aiming for the maximal significance. These results are then used to define signal regions. The optimisation process follows along 3 steps:

Step 1.: Selecting a few benchmark points. These benchmark points are chosen to be around the edges of previous exclusion plots that have already been published for the corresponding models (19, 20). For every benchmark point a multidimensional cut scan will be performed using the ahoi tool (70). A multidimensional cut scan will present a first glance on a potential SR definition.

Step 2.: Look at the results given by Step 1., and use them as input for kinematic plots. The proposed criteria can then be "fine-tuned " by looking at the kinematic distribution of every variable and their specific cut values. As for the first step one optimizes here on the significance.

Step 3.: Using the results from Step 2 as input, potential binning strategies aiming to define SR with multiple bins is tested by performing shape fits with HistFitter (65). In Step 3 a scan is performed over a variety of potential binning strategies. First, the SR given by Step 2 is taken as a basis from which many potential binning strategies are fitted and compared. Second, the most promising variables are used and a reoptimisation of the SR is performed. At this point, the number of bins and their kinematic values are optimized parallelly with the SR. Finally the optimal SR and binning strategy is chosen, while keeping the statistics of the resulting SR in mind.

7.3.1 Multidimensional cut scan using ahoi

N dimensional cut scans are performed by using the publicly available ahoi framework (70). As an input, a given set of kinematic variables is selected. For every variable a range is defined, in which the potential restriction values lie, while allowing the framework to not apply criteria on certain variables if it proves to not be beneficial. The definition of these criteria is based on kinematic distributions comparing signal and background expectations. Some variables are set by the general kinematics of the signal model, while others can be seen in kinematic distribution comparing SM background and signal models. This first broad spectrum of variables and their respective ranges are then used as input for the framework. Ahoi calculates the signal efficiency and background rejection for every single cut combination. Ensuring that the effects seen in the samples is not driven by a limited statistic leading to higher sensitivity, the concept of a train and test dataset is used. At this point it is important to note that ahoi does not use machine learning techniques. The input datasets are split in train and test datasets based on the idea, that when two independent sets of events display similar signatures it can be assumed that the features does not arise from statistical fluctuations. A verification method for the agreement between the test and train datasets used by ahoi is to plot a Receiver Operating Characteristic (ROC) curve. ROC curves are commonly used methods focussing on the illustration of a dependence between the efficiency and corresponding error rate. Figure 7.4 (b) shows such a ROC curve. The ROC curves displays the relation between the signal efficiency and the corresponding background rejection. In an ideal case the train and test curves display a full agreement ensuring that the results are do not suffer from statistical fluctuations in the simulation. As an output, the framework gives a set of kinematic restrictions used for a given signal efficiency and corresponding background rejection point. In terms of an optimisation, one is most interested in the point having the highest signal efficiency and maximal background rejection, but due to constraints on the statistics these selections corresponding to this points will most likely not be useful. The most extreme cases are expected to cut away almost all SM processes. However, for an exclusion plot it is important to keep a number of events in the SR. Otherwise it would be more difficult to check the kinematics of the simulated data with the measured data. Another method used for the interpretation of the multidimensional cut scan is to plot the signal efficiency against the expected significance. Figure 7.4 (a) shows such a plot in which the frameworks sorts all possible cut combinations in bins by their signal efficiency, while only considering cut combinations maximizing the background rejection. The ideal output in terms of the optimisation can be seen as the ideal balance between the maximal significance and a signal efficiency that is expected to be high enough to ensure the kinematic selection has high enough statistics in the defined kinematic region. In a similar way as for the ROC curve, it is important that the significance curves of the train and test datasets display a similar behaviour. Another point that has not been discussed yet is the application of systematic uncertainties on the optimisation. In figure 7.4 (a) four types of curves are presented of which three show the significance with varying systematic uncertainties and the grey curve shows the expected background events of the signal efficiency bins. Coming back to the three curves illustrating the significance, first the blue curve shows the significance if only applying the statistical uncertainty of the MC simulation. On the other hand the red curve omits the statistical uncertainties. Here a flat systematic uncertainty of 30% is applied. Flat values for the uncertainty are guesses justified by results from previous analyses studying similar models and phase spaces. Therefore, the chosen value of 30% is typical when studying SUSY models and will be used later as well. Lastly, the green curve combines the requirements of the blue and red curve, meaning that the a statistical uncertainty and a flat 30% uncertainty are used.

7.3.2 N-1 plots

N-1 plots are defined as kinematic plots that display the general characteristic of a given SR. This SR is defined by kinematic criteria on a number of variables N. In case of a N-1 plot all the restriction are plotted except for one. The kinematic distribution of this one variable, which gives the name N-1, is then plotted displaying the change in the expected significance for a variation on the used criteria. Moreover, the kinematic distribution of every variable can be plotted and the kinematic criteria can be "fine-tuned". Figure 7.5 displays a N-1 plot. In every N-1 plot the cut is symbolized by an arrow, which points in the direction the cut is applied. Additionally the impact of variables excluded in previous optimisation efforts can be investigated and cross-checked.

7.4 WW model optimisation

In the following the optimisation process of both models will be presented. Because both models display very similar kinematic properties, the subsequent optimisation procedures will resemble each other. Therefore, some of the findings will only be explained when describing the optimisation of the WW model.

7.4.1 Step 1: Optimise with a multidimensional cut scan

Chapter 7.3.1 introduced the basic idea of a multidimensional cut scan and explained the methods used to evaluate the scan. The first table lists the variables used as input parameter for the multidimensional cut scan and the corresponding ranges in which a cut on the kinematic variable can be made.

Variable		Value ranges
N_{lep}	$=$	1
$lep^1_{\mathrm{P_T}}$[GeV]	$>$	$\{0, 10, 15, 20, 25, 30, 35, 40, 50\}$
$E_{\mathrm{T}}^{\mathrm{miss}}$[GeV]	$>$	$\{100, 150, 180, 200, 240, 280, 300, 340, 400\}$
N_{Jet}	$\leq$	$\{2, 3, 4\}$
m_{T}[GeV]	$>$	$\{0, 50, 100, 150, 200, 250, 300, 350, 400, 500\}$
$Jet\mathrm{P_T^1}$[GeV]	$>$	$\{0, 40, 60, 80, 100, 120, 150, 200\}$
$Jet\mathrm{P_T^2}$[GeV]	$>$	$\{0, 30, 50, 70, 90, 110, 130\}$
m_{eff}[GeV]	$>$	$\{0, 400, 450, 500, 550, 600, 650, 700, 750, 800, 850, 900, 1200\}$
$\Delta\phi(p_T^{lep}, E_T^{miss})$[rad]	$<$	$\{1.6, 1.8, 2.0, 2.2, 2.4, 2.6, 2.8, 3.0, 3.5\}$
N_{bJet}	$\leq$	$\{0, 1\}$
$\sigma_{\mathrm{E_T^{miss}}}$	$>$	$\{0, 5, 10, 15, 20\}$
m_{jj} upper [GeV]	$<$	$\{85, 90, 100, 110, 120, 150, 1000\}$
m_{jj} lower [GeV]	$>$	$\{0, 40, 50, 60, 65, 70, 75, 80\}$
large R $\mathrm{jet}^1_{\mathrm{p_T}}$[GeV]	$>$	$\{200, 250, 280, 300, 320, 350, 380, 400, 500\}$
large R $\mathrm{jet}^1_{\mathrm{M}}$ upper [GeV]	$<$	$\{85, 90, 100, 110, 120, 150, 1000\}$
large R $\mathrm{jet}^1_{\mathrm{M}}$ lower [GeV]	$>$	$\{40, 50, 55, 60, 65, 70, 75, 80, 85\}$
W Boson Tag		{Yes,No}

Restrictions such as N_{lep}, N_{Jet} and N_{BJet} are based on general properties of the WW model. Moreover, variables like E_T^{miss}, m_{eff} and m_T are useful since they are sensitive to BSM physics. Another class of variables is given by the transverse momenta of objects such as $lep^1_{P_T}$, $Jet^1_{P_T}$, $Jet^2_{P_T}$ and large R $\mathrm{jet}^1_{P_T}$. Putting lower limits on the transverse momentum of the reconstructed particle is useful to restrict the influence of fakes in the SR. Furthermore the analysis uses two methods to reconstruct the mass of the hadronically decaying W boson. The application of both methods can be separated into two cases, the m_{jj} variable that is expected to be sensitive to resolved signatures and the mass of a large R jet, that is sensitive to merged signatures. Kinematic criteria for both variables are placed around the mass of a W boson. Using a boosted boson tagger is expected to benefit the definition of a boosted region.

As explained in the previous sections, figure 7.4 (a) shows the results of the first optimisation steps. Here the significance is plotted against the signal efficiency for a signal point with $m_{\tilde{\chi}_1^\pm}$ 500 GeV and $m_{\tilde{\chi}_1^0}$ 0 GeV. For this point a signal efficiency of 0.072 was chosen, which corresponded to a significance of 1.9 σ. Results from this step are presented in the table below displays the corresponding kinematic values that have been obtained by choosing a

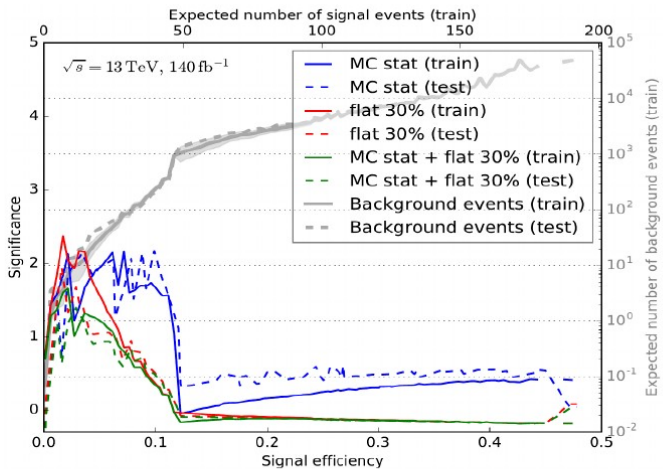

(a) WW model significance against signal efficiency

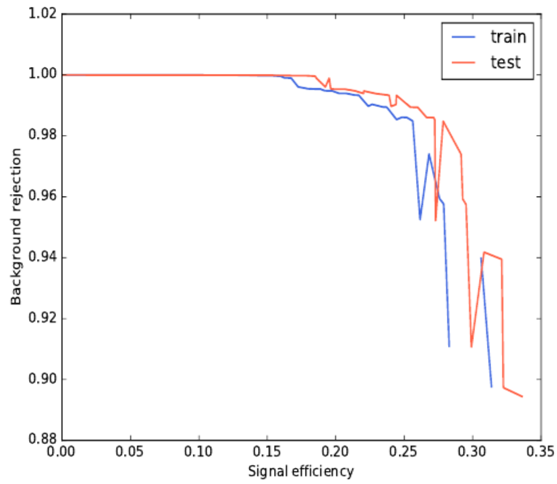

(b) WW model ROC curve

Figure 7.4: Background compositions in the SR and VR

selection corresponding to the most suitable combination of significance and signal efficiency as described in chapter 7.3.

Variable	$m_{\tilde{\chi}_1^\pm} = 400\ m_{\tilde{\chi}_1^0} = 0$	$m_{\tilde{\chi}_1^\pm} = 500\ m_{\tilde{\chi}_1^0} = 0$	$m_{\tilde{\chi}_1^\pm} = 400\ m_{\tilde{\chi}_1^0} = 150$
N_{lep}	=1	=1	=1
$lep^1_{\mathrm{P_T}}$[GeV]	> 10	> 15	> 10
$E_{\mathrm{T}}^{\mathrm{miss}}$[GeV]	> 180	> 200	> 200
N_{Jet}	2-3	2-4	2-3
m_{T}[GeV]	> 150	> 280	> 280
$Jet\mathrm{P}^1_{\mathrm{T}}$[GeV]	> 40	> 60	> 60
$Jet\mathrm{P}^2_{\mathrm{T}}$[GeV]	> 40	> 60	> 60
m_{eff}[GeV]	> 450	> 700	> 500
$\Delta\phi(p_T^{lep}, E_T^{miss})$[rad]	< 2.6	< 2.4	< 3.0
N_{bJet}	=0	=0	=0
$\sigma_{\mathrm{E_T^{miss}}}$	> 20	> 20	> 20
m_{jj} [GeV]	65-90	65-95	65-100
large R $\mathrm{jet}^1_{\mathrm{P_T}}$[GeV]	> 200	> 320	> 250
large R $\mathrm{jet}^1_{\mathrm{M}}$ [GeV]	$65 - 90$	$70 - 100$	$60 - 110$
W Boson Tag	Yes	Yes	Yes
Z [σ] (blue curve)	2.3	1.9	1.5

When using the full collection of variables, the two types of kinematic region definitions, namely resolved and boosted are combined. During the optimisation, scans were also run with subsets of the variable list. These simulated cases like strictly resolved region definitions. Along the selected benchmark points the impact of the different strategies shifted, but they clearly showed that a combination of boosted and resolved variables increases the sensitivity compared to a SR definition, that is restricted to one of the region types. As can be seen in the table below, benchmark points with low values of $\Delta m_{\tilde{\chi}_1^0-\tilde{\chi}_1^\pm}$ are targeted by a resolved SR definition, while benchmark points with high $\Delta m_{\tilde{\chi}_1^0-\tilde{\chi}_1^\pm}$ show the highest significance when using a combined SR definition with resolved and merged variables.

7.4.2 Step 2: Optimise with N-1 plots

Using the results obtained in the previous step, a preliminary SR definition has been formulated for a variety of benchmark points. These preliminary SR definitions can then be validated by using N-1 plots. Additionally, all cut selection of these benchmark points can then be reoptimised and the effect of previously excluded variables can be evaluated as well. The main task of the second step is to find a SR definition, that has the highest sensitivity to benchmark points in the part of the grid this analysis investigates. In Figure 7.5 the sets of N-1 plots for the investigated selection of benchmark points is presented. Here results are shown for the $m_{\tilde{\chi}_1^\pm}$ 700 GeV and $m_{\tilde{\chi}_1^0}$ 0 GeV signal point. All kinematic criteria are carefully cross-checked with the expected number of events in the defined region. This explains why not in all cases the criteria maximising the significance were used. A combined and a resolved SR were optimised separately. As could be expected the combined SR showed the highest sensitivity. But the optimisation of the resolved SR was used as a basis for the definition used in step 3.

7.4.3 Step 3: Optimise with shape fit scans

Step 2 of the optimisation provides the preliminary definition of a combined SR. In step 3, two tasks are targeted: the statistical and simultaneous fit of the two types of SRs and the development of a suitable binning strategy to increase the sensitivity. In a first instance, two bins were defined of which one corresponds to a resolved SR definition and the second one corresponds to a merged SR definition. Table 7.1 shows the definition of initial definition of the two types of SR. Values shown in the table are not necessarily the same ones as displayed in step 2, since the preliminary SR definition was optimized for its best exclusion limits. Moreover, it can be seen that a variety of variables appear to be useful in both types of SR, while variables sensitive to properties of the types of regions differ. In detail m_{jj} is only used in the resolved region, while in the merged region it is substituted with large R jet$^1_{\text{M}}$, which is the large R jet with the highest momentum. Another difference is that kinematic restrictions on the transverse momenta of the small R jets showed no significant gain in sensitivity, but in the boosted region the usage of the large R jet$^1_{\text{P}_\text{T}}$ has lead to a better sensitivity.

Table 7.1: The first draft of a combined WW SR definition from step 2

Variable	resolved region	boosted region
$p_{\text{T}}^{\text{lep}}$[GeV]	> 15	> 15
N_{Jet}^{25}	$2 - 3$	$2 - 4$
N_{bJet}^{25}	=0	=0
$E_{\text{T}}^{\text{miss}}$[GeV]	> 200	> 240
$d\phi(p_{\text{T}}^{\text{lep}}, E_{\text{T}}^{\text{miss}})$	< 2.8	< 2.6
$\sigma_{E_{\text{T}}^{\text{miss}}}$	> 5	> 20
m_{jj}[GeV]	$70 - 100$	-
Number of large R jets	=0	>= 1
large R jet$^1_{\text{M}}$ [GeV]	-	$70 - 95$
W tagged	No	Yes
large R jet$^1_{\text{p}_\text{T}}$ [GeV]	-	> 250
m_{T} [GeV]	> 300	> 300

The corresponding shape fit is displayed in figure 7.8 (a). In general, it presents a shape fit with two bins separated by the number of large R jets. This result will be taken as the

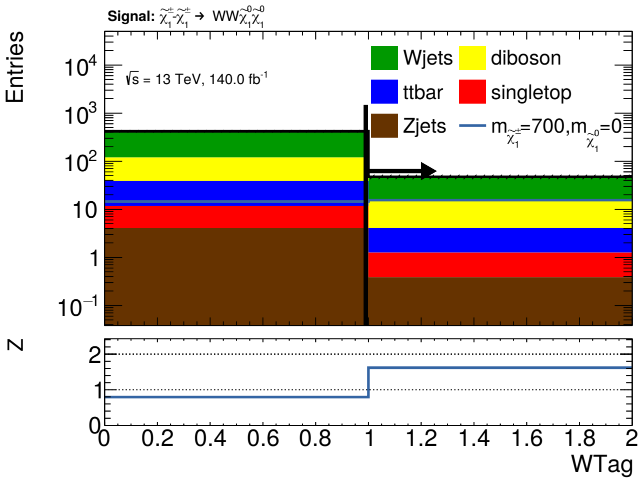
Entries
√s = 13 TeV, 140.0 fb⁻¹
Wjets
diboson
ttbar
singletop
Zjets
Z
WTag

(a)

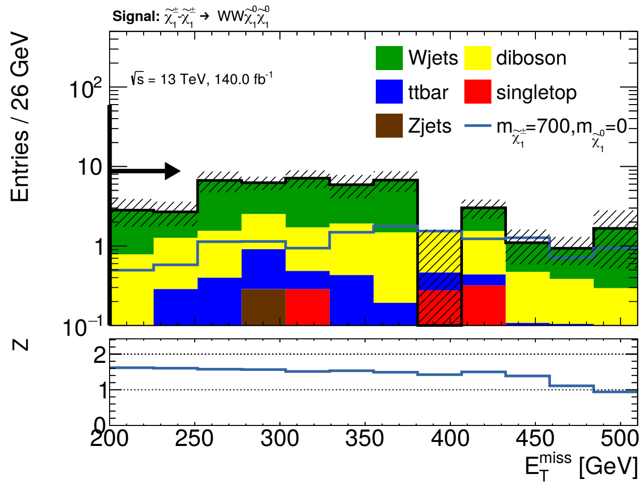
Entries / 26 GeV
√s = 13 TeV, 140.0 fb⁻¹
Wjets
diboson
ttbar
singletop
Zjets
Z
E_T^{miss} [GeV]

(b)

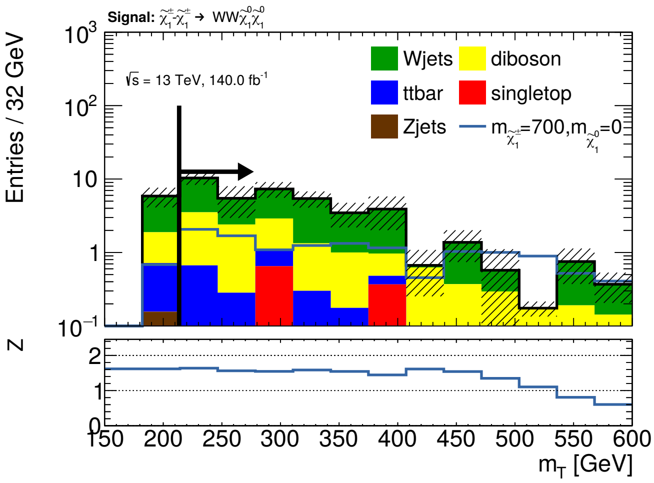
Entries / 32 GeV
√s = 13 TeV, 140.0 fb⁻¹
Wjets
diboson
ttbar
singletop
Zjets
Z
m_T [GeV]

(c)

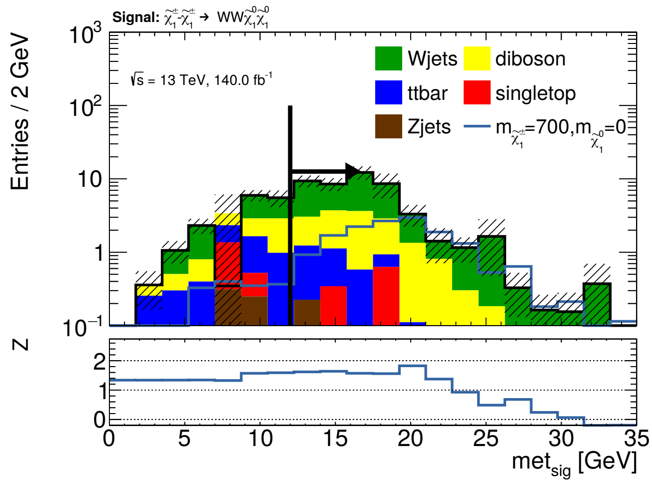
Entries / 2 GeV
√s = 13 TeV, 140.0 fb⁻¹
Wjets
diboson
ttbar
singletop
Zjets
Z
met_{sig} [GeV]

(d)

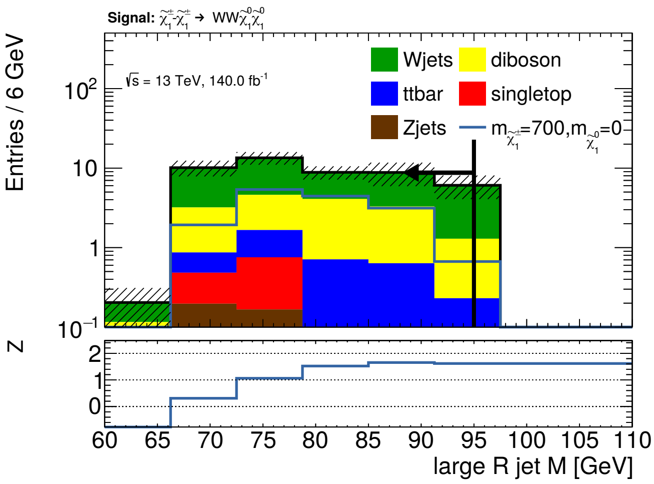
Entries / 6 GeV
√s = 13 TeV, 140.0 fb⁻¹
Wjets
diboson
ttbar
singletop
Zjets
Z
large R jet M [GeV]

(e)

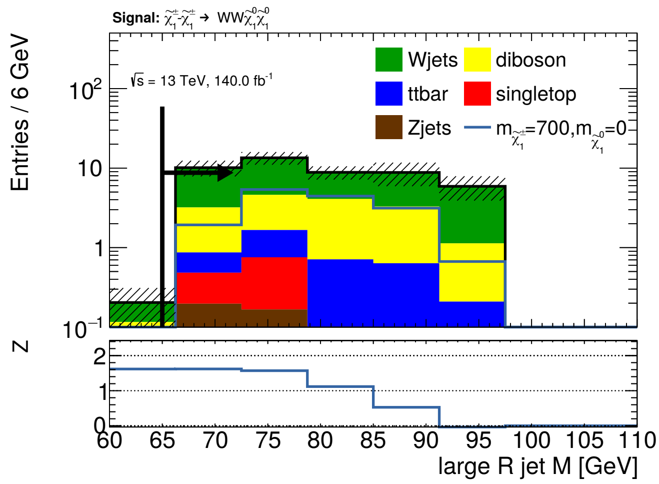
Entries / 6 GeV
√s = 13 TeV, 140.0 fb⁻¹
Wjets
diboson
ttbar
singletop
Zjets
Z
large R jet M [GeV]

(f)

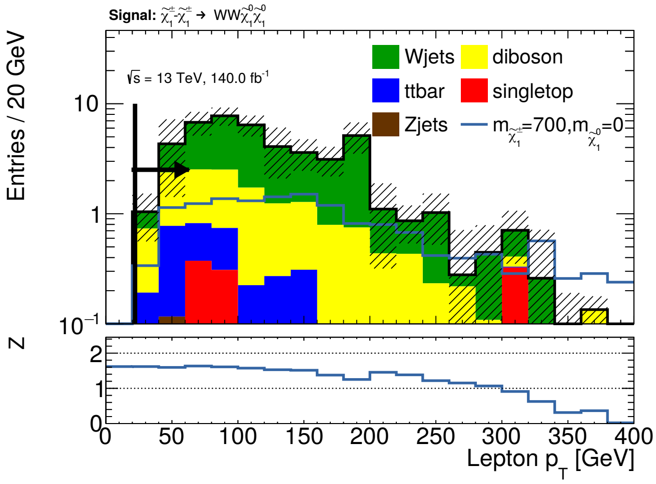

(g)

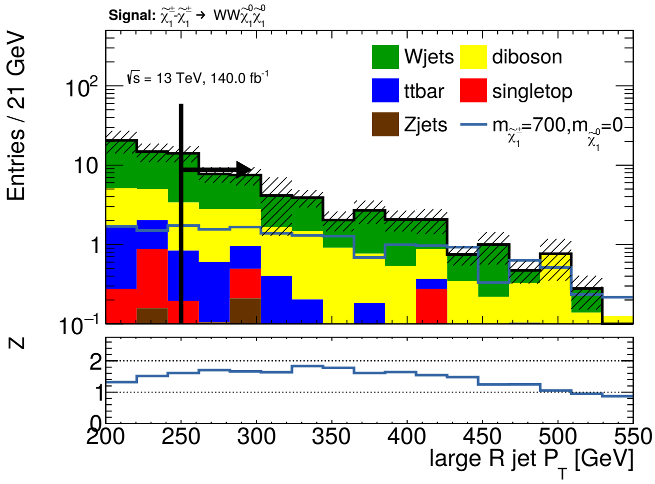

(h)

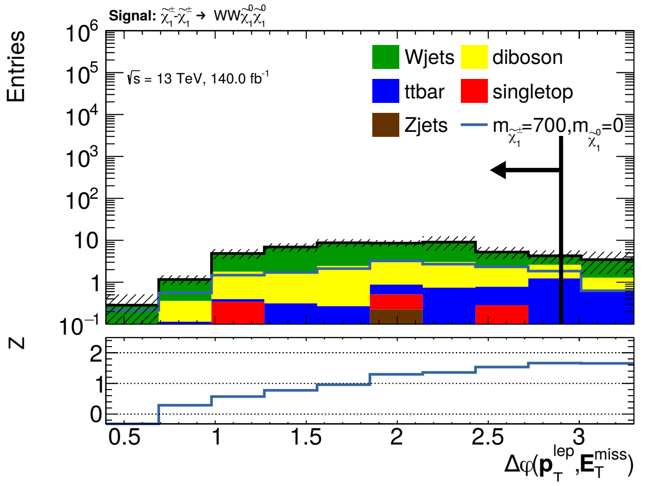

(i)

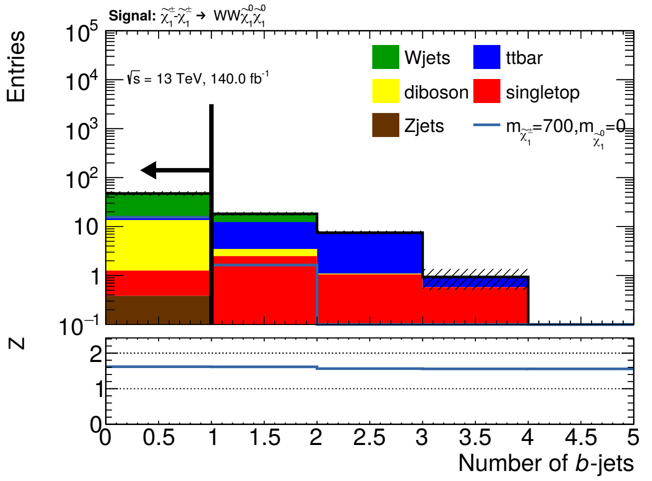

(j)

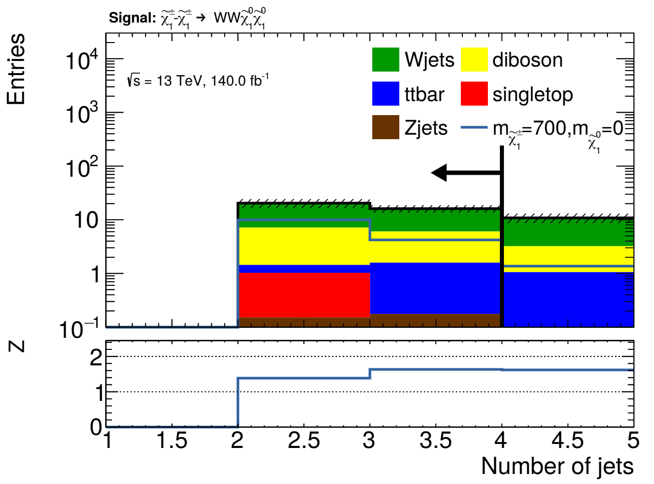

(k)

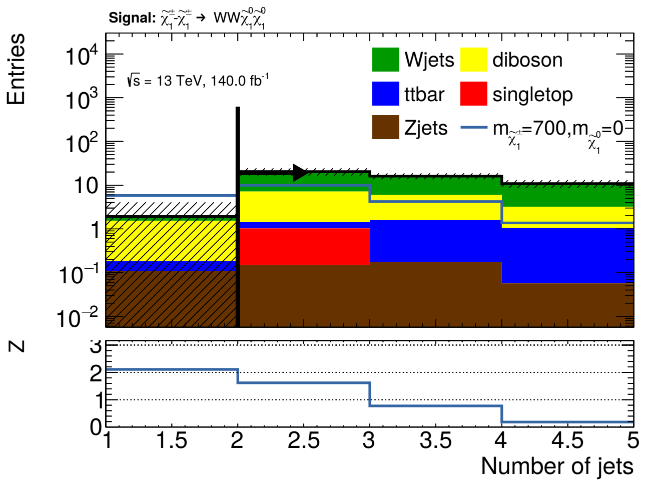

(l)

Figure 7.5: Results from step 1 are studied by using N-1 plots

first draft of a combined SR when comparing the shapes obtained by the various binning strategies.
In order to determine a binning strategy that maximizes the exclusion limits suitable variables will have to be chosen.
Variables used for the formulation of suitable binning strategies are m_{T}, m_{eff} and $E_{\mathrm{T}}^{\mathrm{miss}}$. The selection of these variables is justified by comparing the kinematic distributions as can be seen in figure 7.2. In contrast to the SM background the shapes of all three variables peak at higher values and its shapes does not fade away as sudden as the SM backgrounds. Strategies that seemingly increased the sensitivity were investigated further while strategies that seemingly decreased or did not affect the sensitivity were disregarded. The strategy used for every variable was to begin with two bins in each SR type and optimize them. Ongoing from these the multiplicity of the bins was changed and could vary between the resolved and boosted regions as well. After finding the best SR definition for every variable, further efforts aiming to combine certain binning strategies were investigated as well. For the most promising strategies reoptimisations of the initial SR that served as a first draft were investigated as well. Figure 7.8 (b) presents a collection of the best results given by various investigated binning strategies. Throughout the optimisation a binning strategy using m_{T} has proven to be the most beneficial. The scan plot also illustrates the difference in sensitivity when defining a fit with only the boosted region, which is presented by the grey curve. From this observation the definition of a combined resolved and boosted region seems to give the highest sensitivity.

Conclusively, a binning strategy using m_{T} was chosen. The detailed SR definition of the m_{T} shape fit and a more detailed exclusion plot are presented in chapter 7.6. The SR is separated in five bins of which two are defined as corresponding to the resolved SR definition and three correspond to the merged SR definition. Resolved and merged regions do not share common events due to different requirements on the number of large R jets.

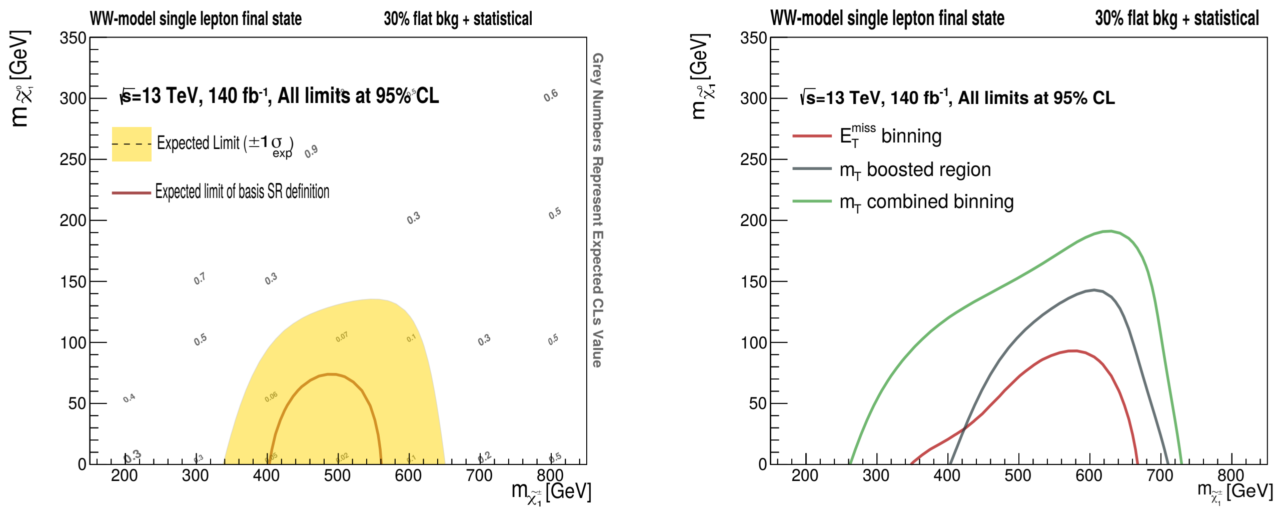

(a) The first draft of a combined WW SR contour plot

(b) WW model scan result

Figure 7.6: Step 3. optimisation reults

7.5 WZ model optimisation

In the following section the optimisation of the WZ model is shown. It was already mentioned that the optimisation strategy is similar compared to the one presented in the previous section. Therefore, some of the steps and ideas will not be explained if they were already presented there.

7.5.1 Step 1: Optimize with a multidimensional cut scan

The starting point of the WZ optimisation is given by a multidimensional cut scan. A collection of input parameters used for the scan is presented in the table below. Largely the selection is the same as the one used for the WW optimisation, except for a change in the number of b-tagged jets, an adjustment of the for the mass range variables m_{jj} and the large R jet mass corresponding to the heavier Z boson, m_{eff} and using the boosted Z Boson Tagger.

Variable		Value ranges
N_{lep}	$=$	1
$lep^{1}_{\mathrm{P_T}}$[GeV]	$>$	$\{0, 10, 15, 20, 25, 30, 35, 40, 50\}$
$E_{\mathrm{T}}^{\mathrm{miss}}$[GeV]	$>$	$\{100, 150, 180, 200, 240, 280, 300, 340, 400\}$
N_{Jet}	$\leq$	$\{2, 3, 4\}$
m_{T}[GeV]	$>$	$\{0, 50, 100, 150, 200, 250, 300, 350, 400, 500\}$
$Jet\mathrm{P}^{1}_{\mathrm{T}}$[GeV]	$>$	$\{0, 40, 60, 80, 100, 120, 150, 200\}$
$Jet\mathrm{P}^{2}_{\mathrm{T}}$[GeV]	$>$	$\{0, 30, 50, 70, 90, 110, 130\}$
m_{eff}[GeV]	$>$	$\{0, 400, 500, 600, 650, 700, 750, 800, 850, 900, 950, 1000, 1200\}$
$\Delta\phi(p_T^{lep}, E_T^{miss})$[rad]	$<$	$\{1.6, 1.8, 2.0, 2.2, 2.4, 2.6, 2.8, 3.0, 3.5\}$
N_{bJet}	$\leq$	$\{0, 1, 2\}$
$\sigma_{\mathrm{E_T^{miss}}}$	$>$	$\{0, 5, 10, 15, 20\}$
m_{jj} upper [GeV]	$<$	$\{95, 100, 105, 110, 120, 150, 1000\}$
m_{jj} lower [GeV]	$>$	$\{0, 40, 50, 60, 65, 70, 75, 80, 85, 88\}$
large R jet$^{1}_{\mathrm{p_T}}$[GeV]	$>$	$\{200, 250, 280, 300, 320, 350, 380, 400, 500\}$
large R jet$^{1}_{\mathrm{M}}$ upper [GeV]	$<$	$\{, 95, 100, 110, 120, 130, 150, 1000\}$
large R jet$^{1}_{\mathrm{M}}$ lower [GeV]	$>$	$\{40, 50, 60, 70, 75, 80, 85, 90, 95\}$
Z Boson Tag		{Yes,No}

The corresponding SR definitions are listed in the table below. In addition, all benchmark points were run with with subsets of the variables corresponding to different types of regions. The results shown correspond to a combined SR definition, which showed the highest significance.

Variable	$m_{\tilde{\chi}_1^\pm,\tilde{\chi}_2^0} = 400\ m_{\tilde{\chi}_1^0} = 0$	$m_{\tilde{\chi}_1^\pm,\tilde{\chi}_2^0} = 500\ m_{\tilde{\chi}_1^0} = 0$	$m_{\tilde{\chi}_1^\pm,\tilde{\chi}_2^0} = 400\ m_{\tilde{\chi}_1^0} = 150$
N_{lep}	=1	=1	=1
$lep^1_{\mathrm{P_T}}$[GeV]	> 10	> 10	> 10
$E_{\mathrm{T}}^{\mathrm{miss}}$[GeV]	> 240	> 300	> 240
N_{Jet}	=2	2-4	1-3
m_{T}[GeV]	> 250	> 250	> 200
$Jet\mathrm{P_T^1}$[GeV]	> 40	> 60	> 60
$Jet\mathrm{P_T^2}$[GeV]	> 40	> 40	> 50
m_{eff}[GeV]	> 0	> 800	> 650
$\Delta\phi(P_T^{lep}, E_T^{miss})$[rad]	< 2.2	< 2.0	< 2.6
N_{bJet}	=0	0-2	0-2
$\sigma_{\mathrm{E_T^{miss}}}$	> 0	> 20	> 20
m_{jj}[GeV]	70-120	65-110	80-1000
large R jet$^1_{\mathrm{P_T}}$[GeV]	> 200	> 320	> 250
large R jet$^1_{\mathrm{M}}$ [GeV]	$65 - 110$	$70 - 100$	$60 - 110$
Z Boson Tag	Yes	Yes	Yes
Z [σ] (blue curve)	2.5	2.2	1.7

7.5.2 Step 2: Optimize with N-1 plots

A preliminary SR definition taken from the results of optimisation step 1 is presented in the table below. Some of the notable differences in comparison to the initial results in section 7.4.1 are larger mass windows regarding the mass of the hadronically decaying boson and the presence of b-tagged jets in the SR. Obviously, changes like the shift of the boson mass window is caused by the higher mass of the Z boson.

Using N-1 plots a validated and reoptisimed SR was constructed. The best sensitivity was given by using a combined region definition that included boosted and resolved variables. For the purpose of defining the first draft of a combined SR used in the third step of the optimisation, an accommodating resolved region was optimised as well.

7.5.3 Step 3: Optimize with shape fit scans

As for the optimisation of the WW model a set of suitable variables has to be chosen for the binning strategy. For the exclusion fit scan of the WZ model a preliminary SR was chosen motivated by results from step 2. The definition is shown in table 7.2. In comparison to the preliminary SR shown for the WW model (table 7.1) one can see that the preliminary SR definition of the WZ model illustrates the fundamental differences between both models. Namely the reconstruction of the hadronically decaying boson, which is a W boson in the WW model defined with a mass cut window of 70-100 GeV in the resolved region and a mass cut window of 70-95 GeV in the boosted region. In contrast, in the WZ model the hadronically decaying Z boson shows the highest significance for a resolved mass cut window of 85-100 GeV and a merged mass cut window of 60-95 GeV. Additionally, most variable restriction values differ between the two preliminary regions, while the value still appear to be very close.

Based on the similarity between the preliminary SR of both models the same scan and binning variables strategy is used. Additionally signatures sensitive the decay of the Z boson into two b quarks are possible and motivate a binning in the b-tagging multiplicity. Similar to the previous scan used in the WW optimisation the second best binning in $E_{\mathrm{T}}^{\mathrm{miss}}$ and the best one in m_{T}. As well the impact of the defined resolved region is illustrated by the yellow curve.

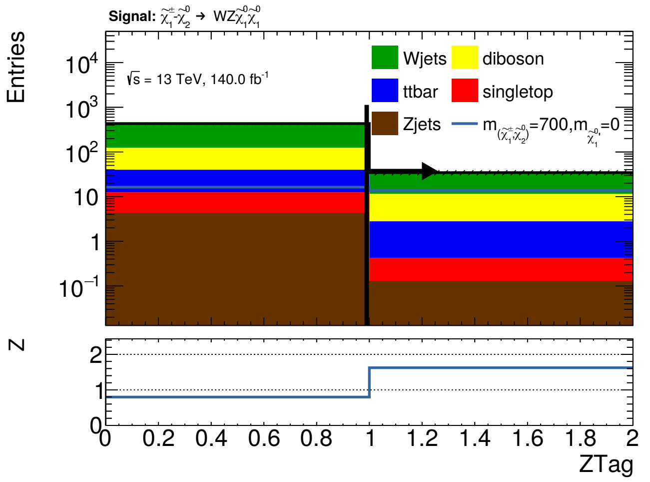
Signal: $\tilde{\chi}_1^{\pm}\tilde{\chi}_2^0 \rightarrow WZ\tilde{\chi}_1^0\tilde{\chi}_1^0$
$\sqrt{s}$ = 13 TeV, 140.0 fb^{-1}
Wjets
diboson
ttbar
singletop
Zjets
$m_{(\tilde{\chi}_1^{\pm},\tilde{\chi}_2^0)}$=700,$m_{\tilde{\chi}_1^0}$=0
Entries
Z
ZTag

(a)

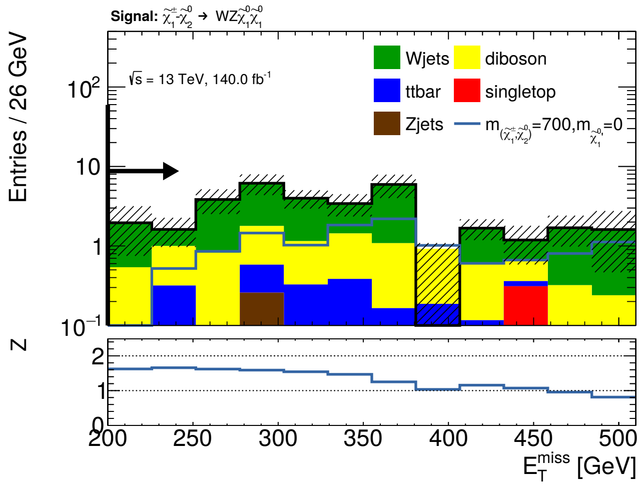
Signal: $\tilde{\chi}_1^{\pm}\tilde{\chi}_2^0 \rightarrow WZ\tilde{\chi}_1^0\tilde{\chi}_1^0$
$\sqrt{s}$ = 13 TeV, 140.0 fb^{-1}
Wjets
diboson
ttbar
singletop
Zjets
$m_{(\tilde{\chi}_1^{\pm},\tilde{\chi}_2^0)}$=700,$m_{\tilde{\chi}_1^0}$=0
Entries / 26 GeV
Z
E_T^{miss} [GeV]

(b)

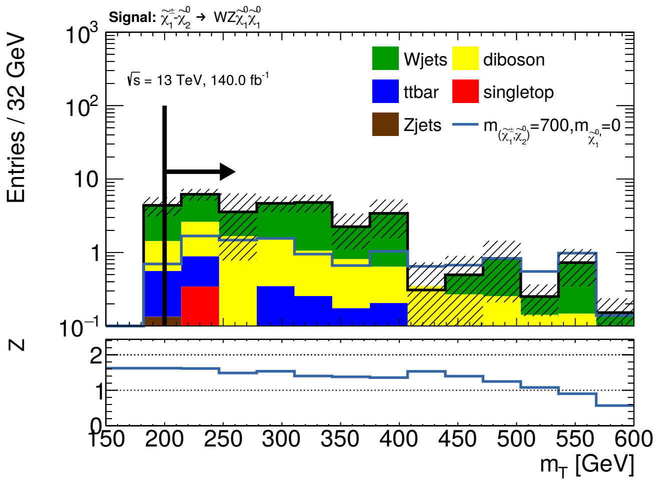
Signal: $\tilde{\chi}_1^{\pm}\tilde{\chi}_2^0 \rightarrow WZ\tilde{\chi}_1^0\tilde{\chi}_1^0$
$\sqrt{s}$ = 13 TeV, 140.0 fb^{-1}
Wjets
diboson
ttbar
singletop
Zjets
$m_{(\tilde{\chi}_1^{\pm},\tilde{\chi}_2^0)}$=700,$m_{\tilde{\chi}_1^0}$=0
Entries / 32 GeV
Z
m_T [GeV]

(c)

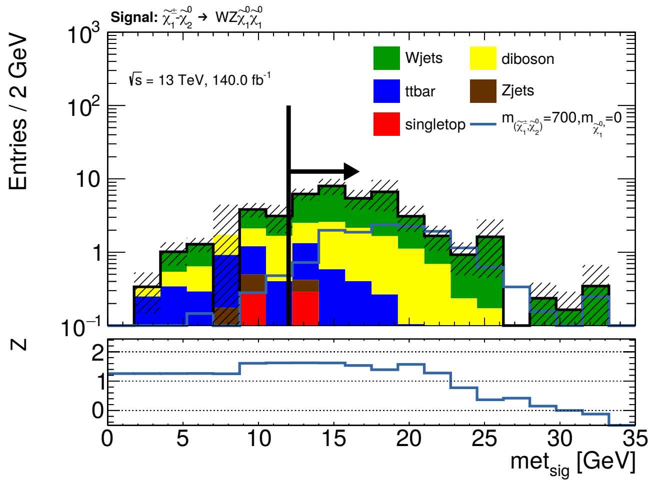
Signal: $\tilde{\chi}_1^{\pm}\tilde{\chi}_2^0 \rightarrow WZ\tilde{\chi}_1^0\tilde{\chi}_1^0$
$\sqrt{s}$ = 13 TeV, 140.0 fb^{-1}
Wjets
diboson
ttbar
Zjets
singletop
$m_{(\tilde{\chi}_1^{\pm},\tilde{\chi}_2^0)}$=700,$m_{\tilde{\chi}_1^0}$=0
Entries / 2 GeV
Z
met_{sig} [GeV]

(d)

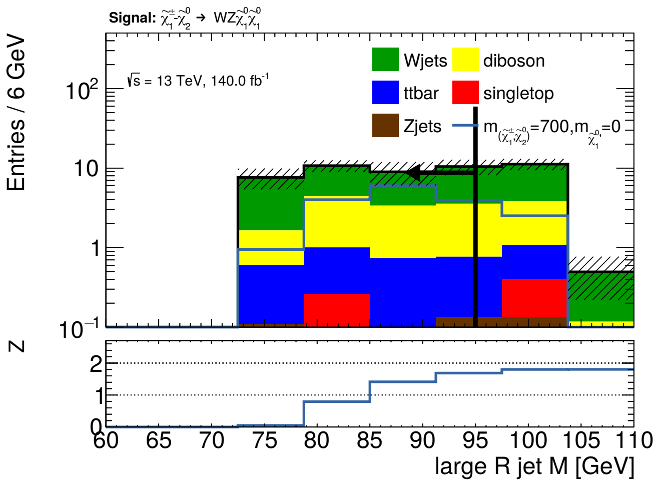
Signal: $\tilde{\chi}_1^{\pm}\tilde{\chi}_2^0 \rightarrow WZ\tilde{\chi}_1^0\tilde{\chi}_1^0$
$\sqrt{s}$ = 13 TeV, 140.0 fb^{-1}
Wjets
diboson
ttbar
singletop
Zjets
$m_{(\tilde{\chi}_1^{\pm},\tilde{\chi}_2^0)}$=700,$m_{\tilde{\chi}_1^0}$=0
Entries / 6 GeV
Z
large R jet M [GeV]

(e)

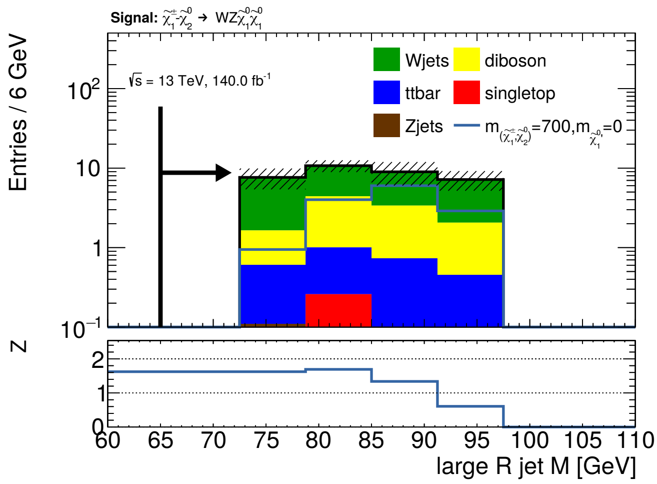
Signal: $\tilde{\chi}_1^{\pm}\tilde{\chi}_2^0 \rightarrow WZ\tilde{\chi}_1^0\tilde{\chi}_1^0$
$\sqrt{s}$ = 13 TeV, 140.0 fb^{-1}
Wjets
diboson
ttbar
singletop
Zjets
$m_{(\tilde{\chi}_1^{\pm},\tilde{\chi}_2^0)}$=700,$m_{\tilde{\chi}_1^0}$=0
Entries / 6 GeV
Z
large R jet M [GeV]

(f)

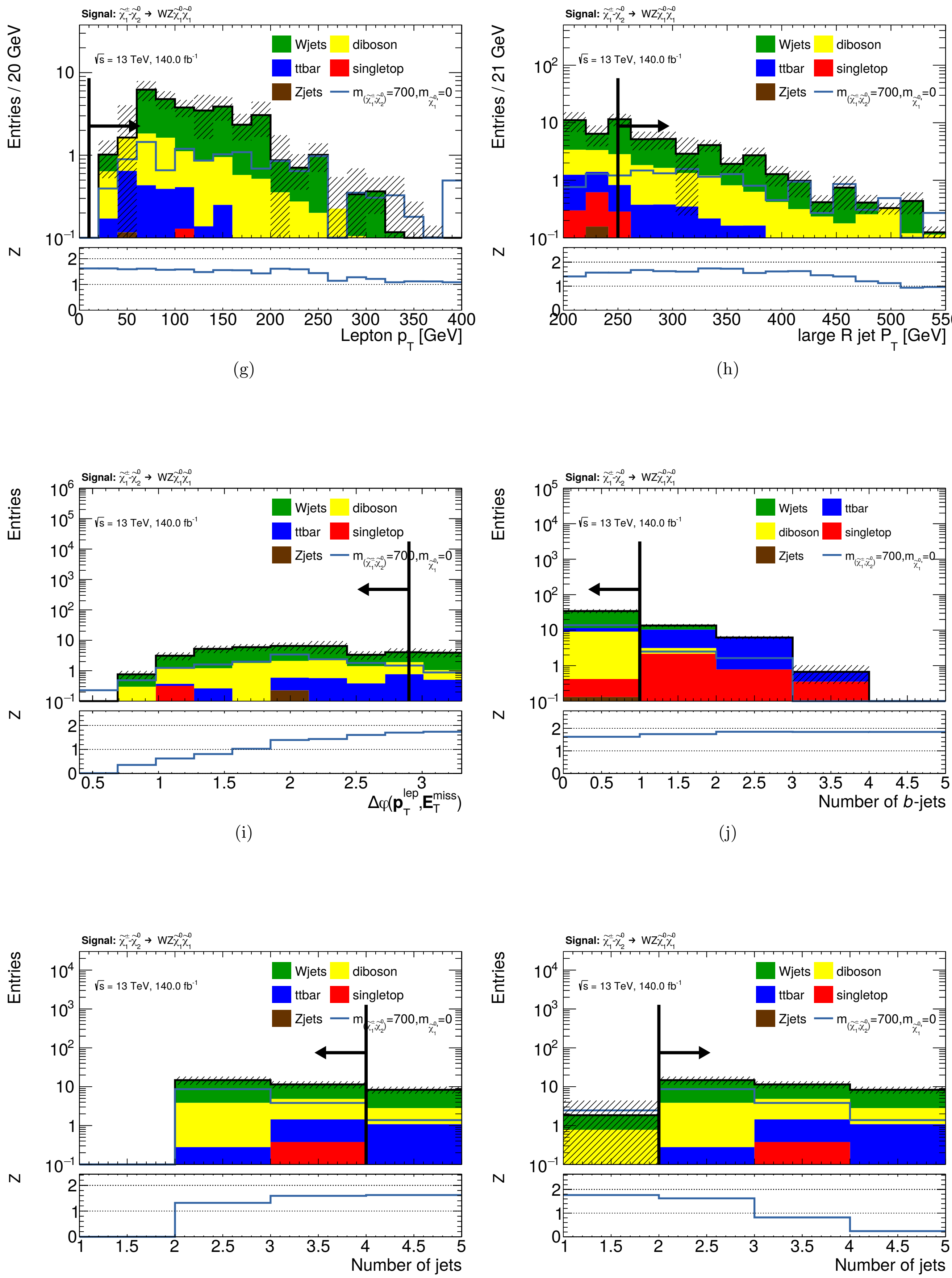

(g) (h)

(i) (j)

(k) (l)

Figure 7.7: Results from step 1 are studied by using N-1 plots

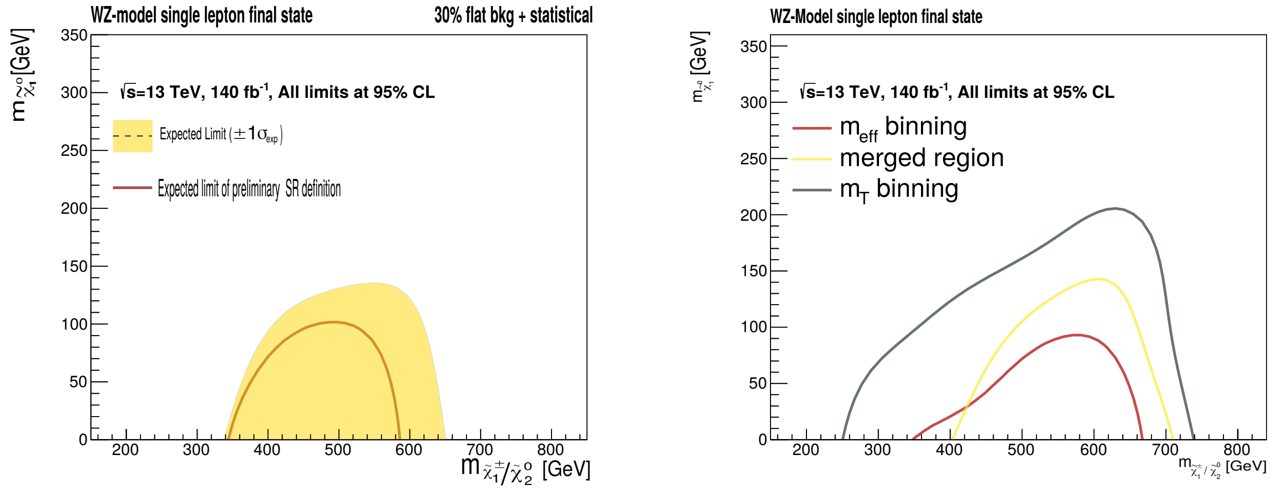

(a) The first draft of a combined WZ SR contour plot

(b) WZ model scan result

Figure 7.8: Step 3. optimisation results

Table 7.2: The first draft of a combined WZ SR definition from step 2

Variable	resolved region	boosted region
$p_{\mathrm{T}}^{\mathrm{lep}}$[GeV]	> 10	> 10
N_{Jet}^{25}	$2-3$	$2-4$
N_{bJet}^{25}	0-2	0-2
$E_{\mathrm{T}}^{\mathrm{miss}}$[GeV]	> 220	> 240
$d\phi(p_{\mathrm{T}}^{\mathrm{lep}}, E_{\mathrm{T}}^{\mathrm{miss}})$	< 2.7	< 2.4
$\sigma_{E_{\mathrm{T}}^{\mathrm{miss}}}$	> 10	> 20
m_{jj}[GeV]	$85-100$	-
Number of large R jets	=0	>= 1
large R jet$_{\mathrm{M}}^{1}$ [GeV]	-	$70-120$
Z tagged	No	Yes
large R jet$_{p_{\mathrm{T}}}^{1}$ [GeV]	-	> 250
m_{T} [GeV]	> 260	> 260

7.6 Results of the WW and WZ optimisation

In the previous section the optimisation studies for both signal models were presented. Resulting exclusion plots are presented in figure 7.9 and 7.10. These fits assume a flat uncertainty of 30% and include the statistical uncertainty coming from the MC as well. Both models are fitted using simplified shape fits in m_{T} as defined in chapter 7.2 and the conclusive SR definitions are shown in the table below.

	WW model		WZ model	
Variable	resolved region	boosted region	resolved region	boosted region
$p_{\mathrm{T}}^{\mathrm{lep}}$[GeV]	> 25	> 25	> 25	> 25
N_{Jet}^{25}	$2-4$	$<= 4$	$2-4$	$<= 4$
N_{bJet}^{25}	=0	=0	=0	=0
$E_{\mathrm{T}}^{\mathrm{miss}}$[GeV]	> 200	> 200	> 200	> 200
$\Delta\phi(p_{\mathrm{T}}^{\mathrm{lep}}, E_{\mathrm{T}}^{\mathrm{miss}})$	< 2.9	< 2.9	< 2.8	< 2.6
$\sigma_{E_{\mathrm{T}}^{\mathrm{miss}}}$	-	> 15	-	> 15
m_{jj}[GeV]	$70-90$	-	$80-110$	-
Number of large R jets	=0	>= 1	=0	>= 1
large R jet$^1_{\mathrm{M}}$ [GeV]	-	< 100	-	< 105
W tagged	No	Yes	No	No
Z tagged	No	No	No	Yes
large R jet$^1_{p_{\mathrm{T}}}$ [GeV]	-	> 300	-	> 250
m_{T} [GeV]	-	100-250	-	100-250
	200-380	250-420	200-380	250-420
	> 380	> 420	> 380	> 420

Looking at the two contours it can be seen that the expected exclusion limits are similar to each other. This would have been expected since the SR definitions and kinematics are similar as well. Moreover, it appears that the similarity is primarily induced by the boosted region, which is actually the region giving the highest sensitivity, because in the boosted regime the difference between the W and Z boson are expected to vanish in the smearing of a boosted reconstruction. In contrast the resolved region was defined as a complementary region increasing the sensitivity of the boosted region, but not as a stand-alone region.

Published results by ATLAS for both models from previous analyses can be seen in (19, 20). These results are from the 2 and 3 lepton channels. Comparing these results to the ones obtained during the presented optimisation process, one sees a clear improvement of the exclusion limits. It has to be noted, that the results presented in this work are based on simulated data, while the results published results are based on measured data. At this point, the claim of improving the previous results is based on the assumption, that the used data reflects the measured data.

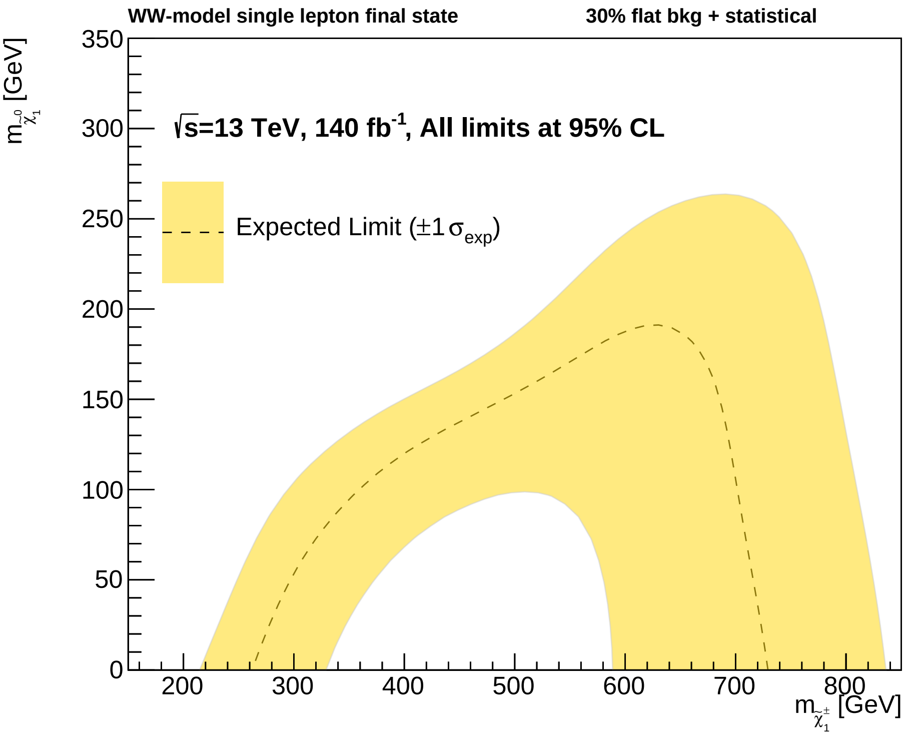

Figure 7.9: Exclusion plot for the WW model

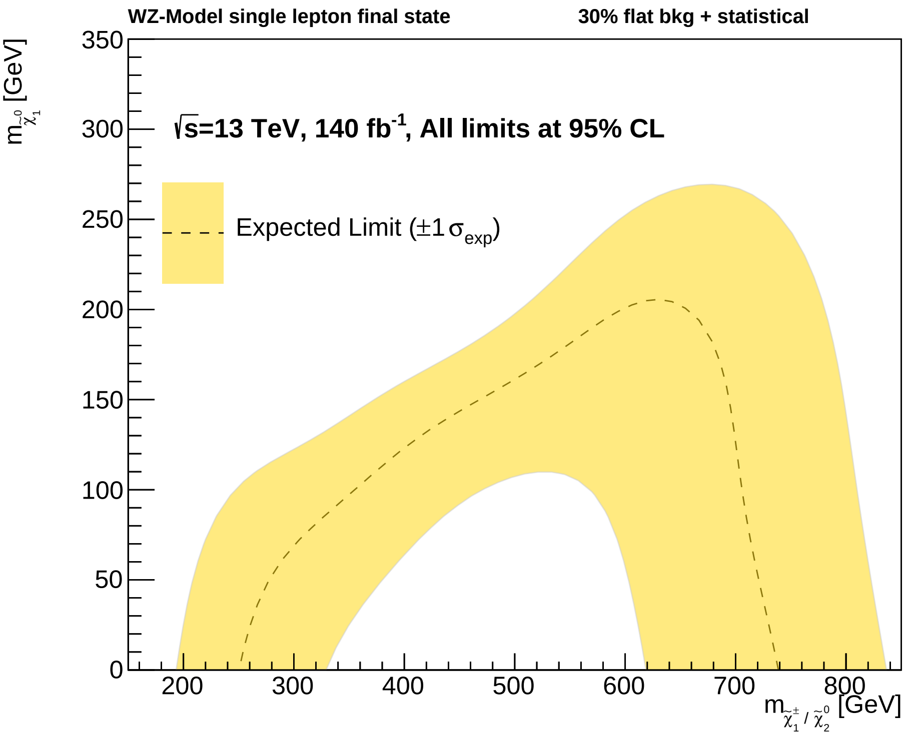

Figure 7.10: Exclusion plot for the WZ model

Chapter 8

Control Region definitions

In the following chapter the definition and construction of the CR used for both models is presented.

8.1 Background estimation

During the optimisation process of an analysis simulated data is used. When performing the fit it is assumed that the variables used to separate the SRs and CRs are represented very well in the fit. A method commonly used in searches for SUSY is to validate the modelling with VRs. The strategy used is shown in figure 8.1. First a set CR is defined, which will be shown in chapter 8. Corresponding to the SRs a set of VRs is defined. In a background-only fit the backgrounds are normalized to data in the CRs. This is shown in figure 8.1. The normalization factor found is applied to the background simulation in the SR to obtain the background estimates in the SR. The extrapolation from CRs to SRs is cross-checked in VRs. If an excess in data in the SRs is found, discovery significances are calculated, else exclusion limits for specific signal models.

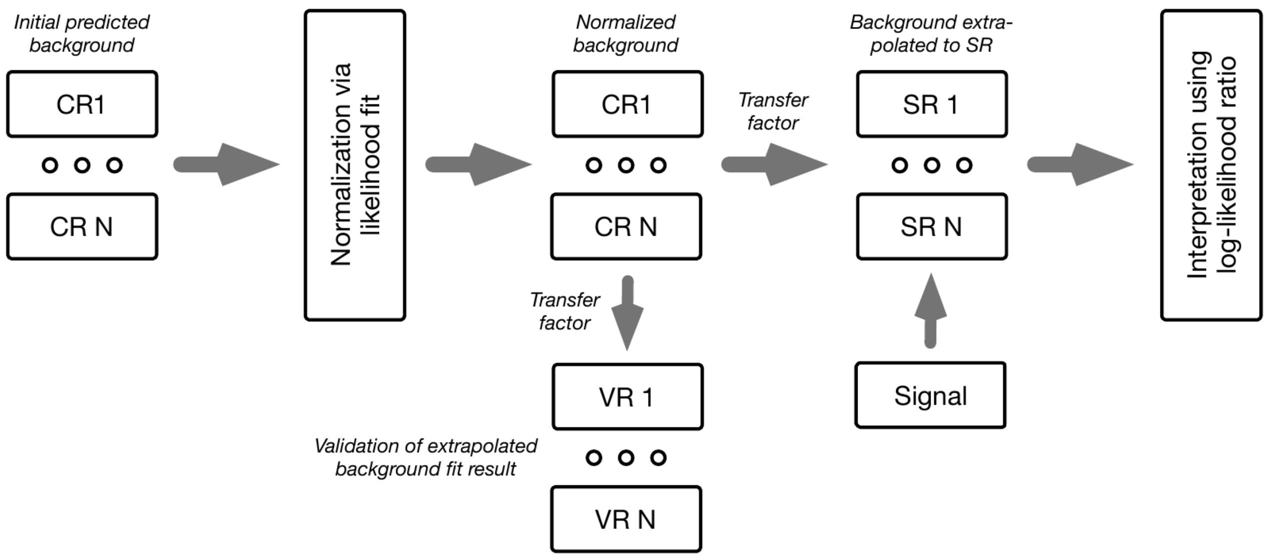

Figure 8.1: Schematic process of the fit strategy of an analysis (65)

8.2 SR background composition for WW

Illustrated in the table below are the yields of all the kinematic regions of the WW SR. The expected number of SM background events and of a benchmark signal model are shown. From this background composition it is possible to identify the main backgrounds contributing in the SR. As can be seen in the table, W+jets , diboson and $t\bar{t}$ are expected to show the largest contribution in the respective SRs. While W+jets is the dominant background in every SR bin, the relation between $t\bar{t}$ and diboson differs between the merged and resolved SRs. The second largest background in the resolved SR is $t\bar{t}$, while diboson is the second largest background for merged cases. From this it appears that for each main background a resolved and boosted control region will have to be defined.

Table 8.1: Yieldstable for the WW SR definition. Here the five bins are shown and ordered in resolved and boosted and on a subordinate level they are ordered by their m_{T} mass window

Process	SRLM resolved	SRHM	SRLM boosted	SRMM	SRHM
Total SM	507.83 ± 38.88	384.42 ± 75.03	79.90 ± 6.74	31.51 ± 4.73	18.13 ± 3.13
$\mathrm{t\bar{t}}$	63.30 ± 2.16	16.10 ± 1.03	4.24 ± 0.28	0.53 ± 0.08	0.24 ± 0.04
W+jets	329.84 ± 38.14	318.81 ± 74.81	30.36 ± 4.78	9.51 ± 3.61	6.00 ± 2.83
Single top	3.42 ± 0.98	2.91 ± 0.89	1.13 ± 0.58	0.28 ± 0.28	0.31 ± 0.31
Diboson	49.73 ± 1.44	18.94 ± 1.02	12.17 ± 1.05	4.55 ± 0.31	2.53 ± 0.22
Z+jets	7.28 ± 2.74	4.94 ± 3.67	0.57 ± 0.22	0.01 ± 0.20	0.05 ± 0.06
$m_{\tilde{\chi}_1^\pm} = 300$ $m_{\tilde{\chi}_1^0} = 0$	53.23 ± 6.47	20.64 ± 3.95	28.04 ± 4.57	12.49 ± 3.01	2.11 ± 1.23
$m_{\tilde{\chi}_1^\pm} = 700$ $m_{\tilde{\chi}_1^0} = 0$	1.03 ± 0.15	2.09 ± 0.22	3.39 ± 0.28	4.15 ± 0.31	6.89 ± 0.40

When constructing a potential background CR, which should be designed in such a way that it shows the largest possible relative amount of events of a given background, while the kinematic definition of the region displays a similarity to the SR. Conclusively, it means that a CR is constructed by changing the criteria on a minimal number of variables. An ideal CR definition would only include changes of one variable, e.g if one inverts the value setting an upper limit instead of a lower limit. However, there are cases that do not allow for a simple CR definition. In these cases changes on other variables have to be included, while one would try to minimise the amount of changes with respect to the original SR. Another point that can potentially exacerbate the definition of a CR is the signal contamination, which is required to be as low as possible. However, in some cases a the definition of a CR with no signal contribution is more difficult, when only changing a few variables. Therefore a compromise is chosen by allowing a certain signal contribution in the CRs, here amounting to 10% of the total event yields in the CR.

8.3 SR background composition for WZ

Table 8.1 displays the yields in all kinematic regions of the WZ SR. As can be seen in the table, W+jets , diboson and $t\bar{t}$ contribute the highest amounts of events in the respective SRs. In order to distinguish between the two kinds of background compositions in the resolved and boosted signatures, two different types of CRs are defined.

Table 8.2: Yieldstable for the WZ SR definition. Follows the same nomenclature as in table 8.1.

Process	SRLM resolved	SRHM	SRLM boosted	SRMM	SRHM
Total SM	584.99 ± 42.95	250.50 ± 62.24	70.29 ± 5.08	27.74 ± 4.18	13.92 ± 2.32
$t\bar{t}$	83.82 ± 2.51	14.61 ± 0.97	4.31 ± 0.29	0.53 ± 0.09	0.11 ± 0.03
Diboson	60.38 ± 1.42	17.49 ± 0.79	12.36 ± 0.85	4.41 ± 0.28	1.69 ± 0.16
W+jets	369.43 ± 42.52	194.02 ± 62.11	28.20 ± 3.85	11.77 ± 3.71	4.55 ± 2.08
Single top	7.49 ± 1.47	1.32 ± 0.55	0.95 ± 0.48	0.26 ± 0.26	0.00 ± 0.00
Z+jets	2.74 ± 1.82	3.14 ± 2.49	0.34 ± 0.15	0.10 ± 0.17	0.05 ± 0.04
$m_{\tilde{\chi}_1^\pm,\tilde{\chi}_2^0} = 300$ $m_{\tilde{\chi}_1^0} = 0$	59.71 ± 4.80	17.70 ± 2.66	20.23 ± 3.13	7.39 ± 1.82	1.64 ± 0.86
$m_{\tilde{\chi}_1^\pm,\tilde{\chi}_2^0} = 700$ $m_{\tilde{\chi}_1^0} = 0$	1.42 ± 0.26	2.21 ± 0.32	3.89 ± 0.44	3.49 ± 0.41	5.88 ± 0.53

8.3.1 $t\bar{t}$ CR definition

As already mentioned for every dominant background two kinds of CRs are defined. One is used for the background estimation in the resolved region and one is used for the background estimation in the boosted region. In the SR definition a strict veto on b-tagged jets is used. As can be seen in chapter 4.2.2 the production of a top quark pair will almost always result in a final state displaying two b quarks. Therefore, for the definition of the CR, two b-tagged jets are demanded. Additionally, the $t\bar{t}$ CR is defined in a m_{T} window from 100 GeV to 200 GeV.

The next step is then to investigate the background composition and signal contamination of both regions.

Background composition in $t\bar{t}$ CR

Figures 8.2 and 8.3 show the contributions from the SM backgrounds in the defined $t\bar{t}$ CR. The background composition is displayed by a pie chart showing the percentual amount a SM background contributes in the CR. For all regions presented, the $t\bar{t}$ contribution dominates with values of up to 90 %. Furthermore, the influence of other main backgrounds like W+jets is clearly limited.

Signal contamination for $t\bar{t}$ CR

Figures 8.4 and 8.5 display the signal contamination in the $t\bar{t}$ CRs defined for the WW and WZ model. For the measure of the signal contamination the percental amount of signal events of a given signal point is plotted over a grid of all available signal points. In case of the regions defined for the WW model, the signal contamination is clearly within the set limits. This follows directly from the condition that two b-tagged jets were required because, as already explained at a previous point, a final state signature with two b-tagged jets is kinematically forbidden in the WW model.
On the other hand the WZ model shows a relatively larger signal contamination, but it is still clearly below the limit of 10%.

8.3.2 W+jets CR definition

W+jets is the largest SM background in every SR bin. Due to the characteristics of a W+jets process, as mentioned in chapter 7, a lowering of the restriction on m_{T} appears to be a suit-

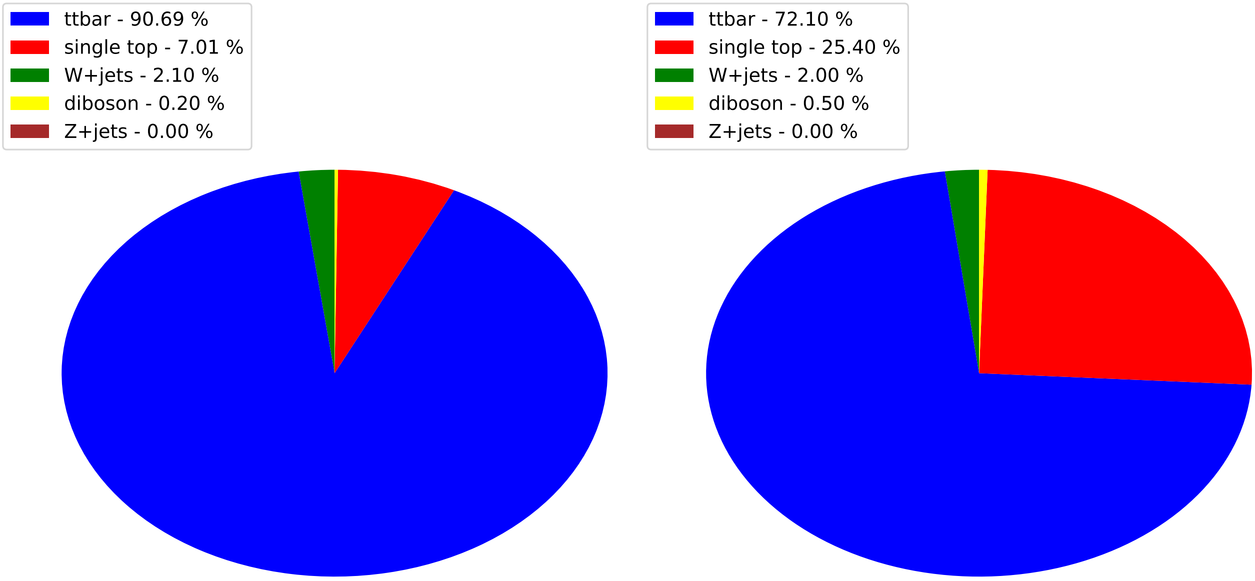

(a) WW model resolved CR

(b) WW model boosted CR

Figure 8.2: WW model CR background composition

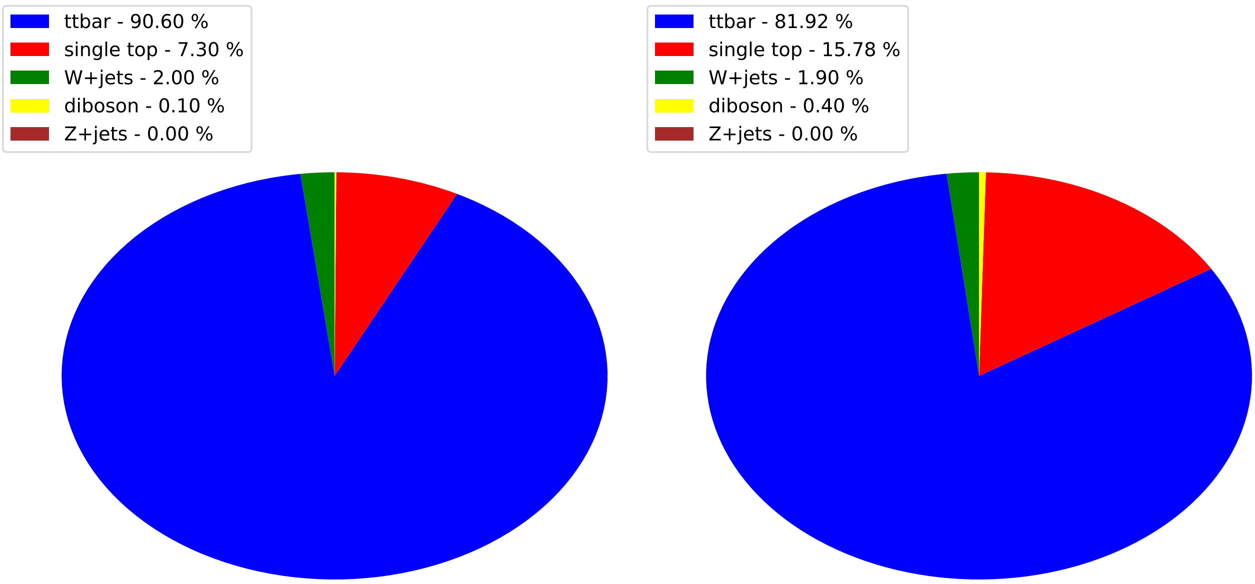

(a) WZ model resolved CR

(b) WZ model boosted CR

Figure 8.3: WZ model CR background composition

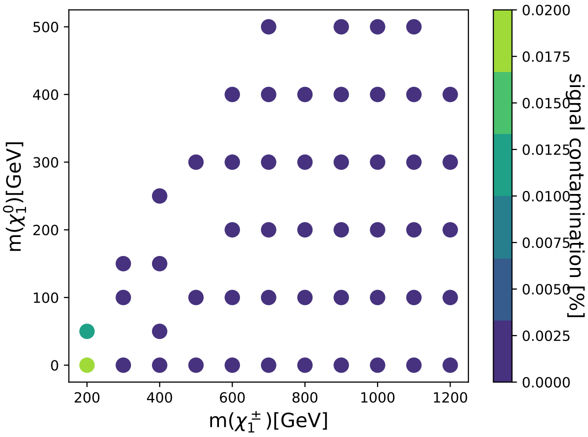

(a) WW model resolved CR

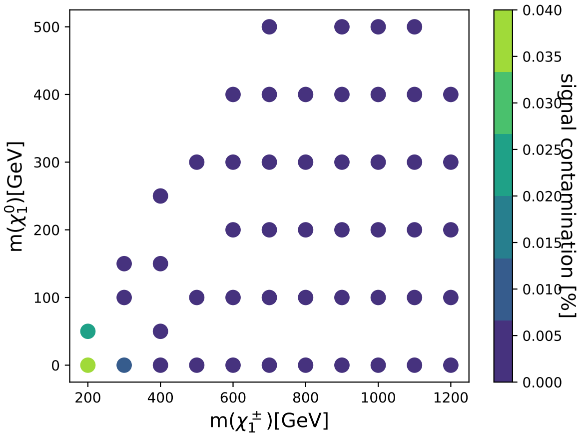

(b) WW model boosted CR

Figure 8.4: WW model CR signal contamination

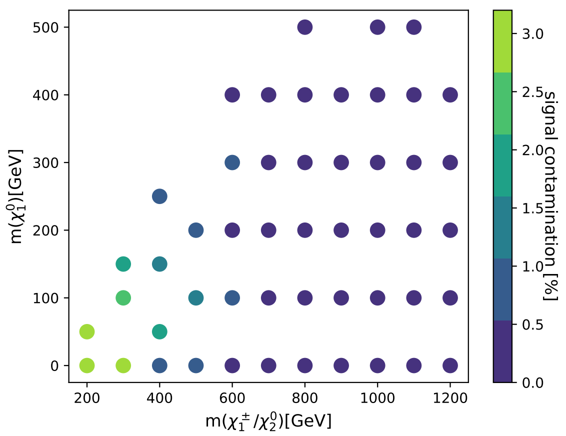

(a) WZ model resolved CR

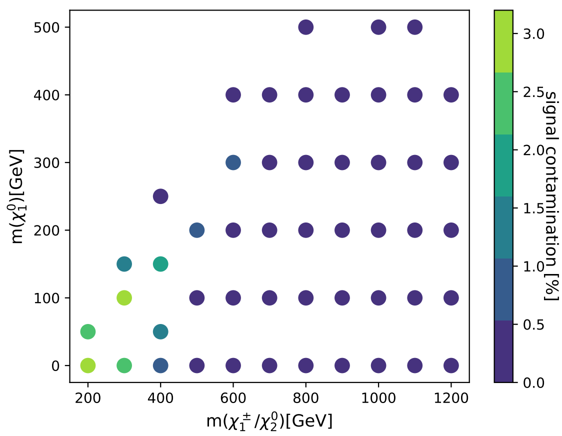

(b) WZ model boosted CR

Figure 8.5: WZ model CR signal contamination

Table 8.3: $t\bar{t}$ CR definition

Variable	WW model resolved region	boosted region	WZ model resolved region	boosted region
N_{lep}	=1	=1	=1	=1
$p_{\mathrm{T}}^{\mathrm{lep}}$[GeV]	> 25	> 25	> 25	> 25
N_{Jet}^{25}	$2-4$	$<= 4$	$2-4$	$<= 4$
N_{bJet}^{25}	=2	=2	=2	=2
$E_{\mathrm{T}}^{\mathrm{miss}}$[GeV]	> 200	> 200	> 200	> 200
$\Delta\phi(p_{\mathrm{T}}^{\mathrm{lep}}, E_{\mathrm{T}}^{\mathrm{miss}})$	< 2.9	< 2.9	< 2.8	< 2.6
$\sigma_{E_{\mathrm{T}}^{\mathrm{miss}}}$	-	< 15	-	< 15
m_{jj}[GeV]	75-90	-	80-110	-
Number of large R jets	=0	$>= 1$	=0	$>= 1$
large R jet$_{\mathrm{M}}^{1}$ [GeV]	-	< 100	-	< 105
W tagged	No	Yes	No	No
Z tagged	No	No	No	Yes
large R jet$_{\mathrm{p_T}}^{1}$ [GeV]	-	> 300	-	> 250
m_{T} [GeV]	100-200	100-200	100-200	100-200

able strategy for the resolved case, as for SM processes the m_{T} distribution peaks around the W boson mass. $t\bar{t}$ processes are also enhanced for lower m_{T} values, but are suppressed by applying a veto on b-tagged jets.
When investigating a CR definition for the boosted region, a separation inverting the restrictions on the missing transverse energy significance was used, as shown in figure 8.6 (b). The SR is defined with a value for $\sigma_{E_T^{miss}}$ greater than 15. Corresponding the CR is defined with a $\sigma_{E_T^{miss}}$ value between 2 and 12.

Table 8.4: W+jets CR definition

Variable	WW model resolved region	boosted region	WZ model resolved region	boosted region
N_{lep}	=1	=1	=1	=1
$p_{\mathrm{T}}^{\mathrm{lep}}$[GeV]	> 25	> 25	> 25	> 25
N_{Jet}^{25}	$2-4$	$<= 4$	$2-4$	$<= 4$
N_{bJet}^{25}	=0	=0	=0	=0
$E_{\mathrm{T}}^{\mathrm{miss}}$[GeV]	> 200	> 200	> 200	> 200
$\Delta\phi(p_{\mathrm{T}}^{\mathrm{lep}}, E_{\mathrm{T}}^{\mathrm{miss}})$	< 2.9	< 2.9	< 2.8	< 2.6
$\sigma_{E_{\mathrm{T}}^{\mathrm{miss}}}$	-	< 15	-	< 15
m_{jj}[GeV]	75-90	-	80-110	-
Number of large R jets	=0	$>= 1$	=0	$>= 1$
large R jet$_{\mathrm{M}}^{1}$ [GeV]	-	< 100	-	< 105
W tagged	No	Yes	No	No
Z tagged	No	No	No	Yes
large R jet$_{\mathrm{p_T}}^{1}$ [GeV]	-	> 300	-	> 250
m_{T} [GeV]	100-200	> 100	100-200	> 100

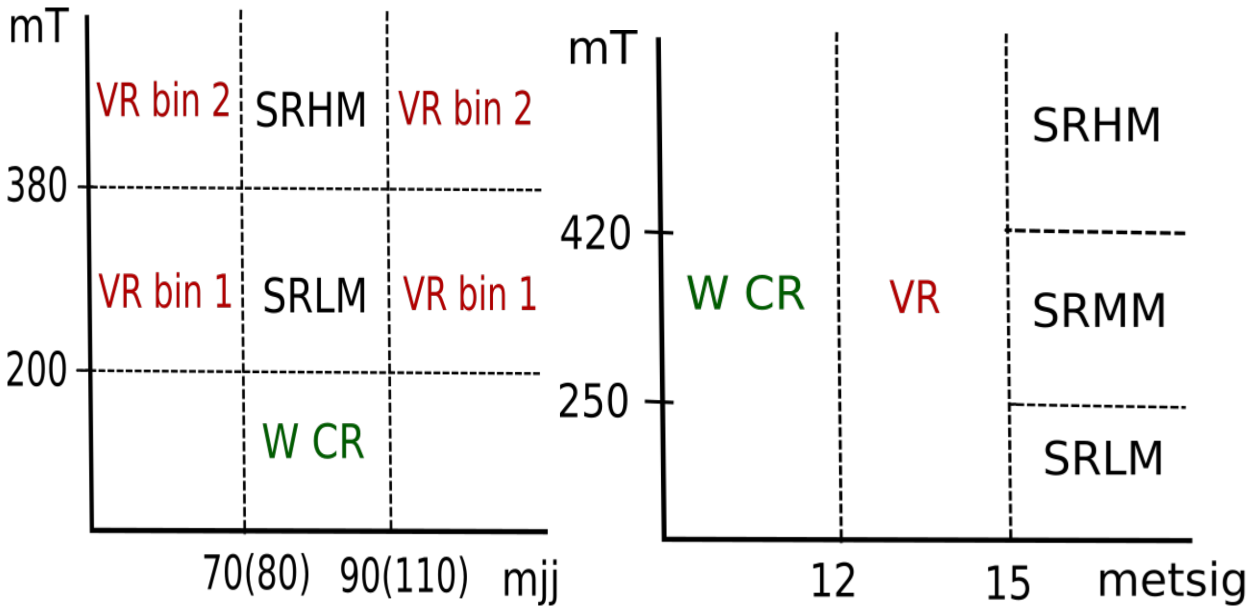

(a) Resolved CR and VR display (b) Boosted CR and VR display

Figure 8.6: WW/WZ model fit region display

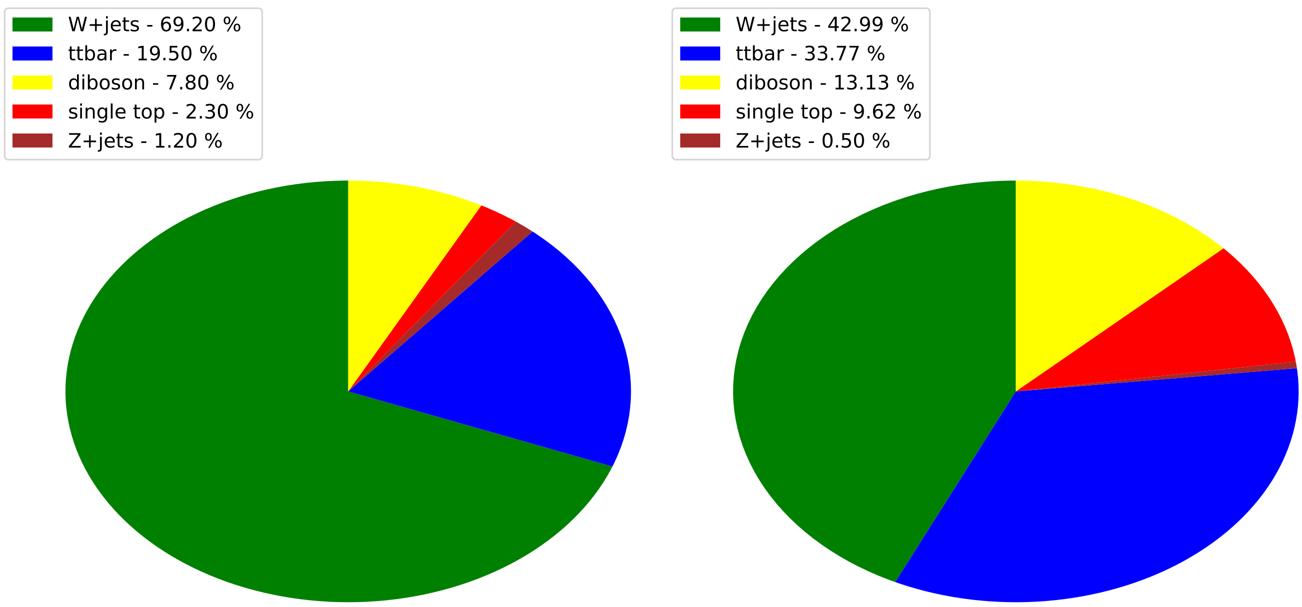

(a) WW model resolved region (b) WW model boosted region

Figure 8.7: Background compositions of the W+jets CR

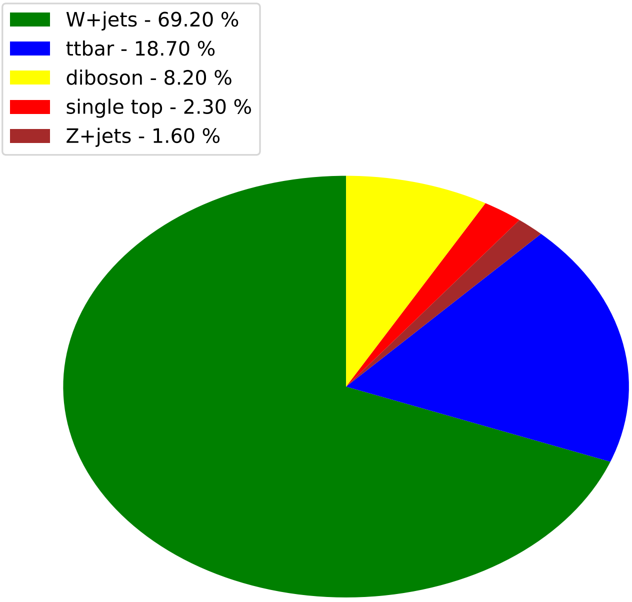

(a) WZ model resolved region

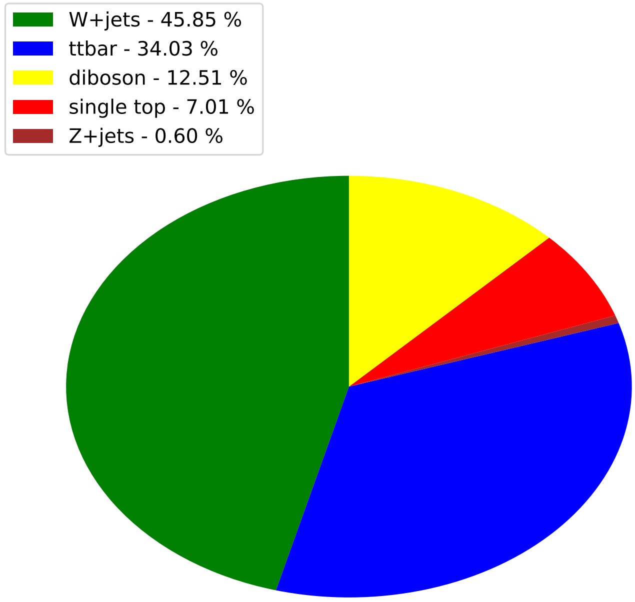

(b) WZ model boosted region

Figure 8.8: Background compositions of the W+jets CR

Background composition in W+jets CR

Considering the resolved case, the CR and SR are separated by inverting m_{T}. Figure 8.6 (b) shows the schematic placement of the W+jets CR. Figures 8.7 and 8.8 illustrate the background composition in the defined CR. Considering both models, the W+jets contribution in the resolved CR dominates with a value of 70%. On the other hand, for the boosted CRs, the percentage of W+jets is 43% in the WW CR and 45.8% in the WZ CR. However, the contribution of $t\bar{t}$ is 33.7% in the WW CR and 34% in the WZ CR. While W+jets is the largest background in this region it is not the clearly dominating background in the CRs. While it is not an ideal case, W+jets is still the clearly dominant background.

Signal contamination for W+jets CR

Signal contamination corresponding to the CR definitions for both models are shown in Figure 8.9 and 8.10. In all four figures the percental signal contamination in the respective CRs is mostly within the previously defined limits. In the case of the resolved regions the maximal values are around 5.7% (WW model) and 4.9% (WZ model). On the other hand, the maximal values are around 10.4% (WW model) and 9.5% (WZ model). The value for the boosted WW region corresponds to the signal point with $m_{\chi_1^\pm} = 200$ GeV and $m_{\chi_1^0} = 0$ GeV. This point has to be treated carefully and further studies will have to investigate potential reoptimisations of the CR to accommodate this problem..

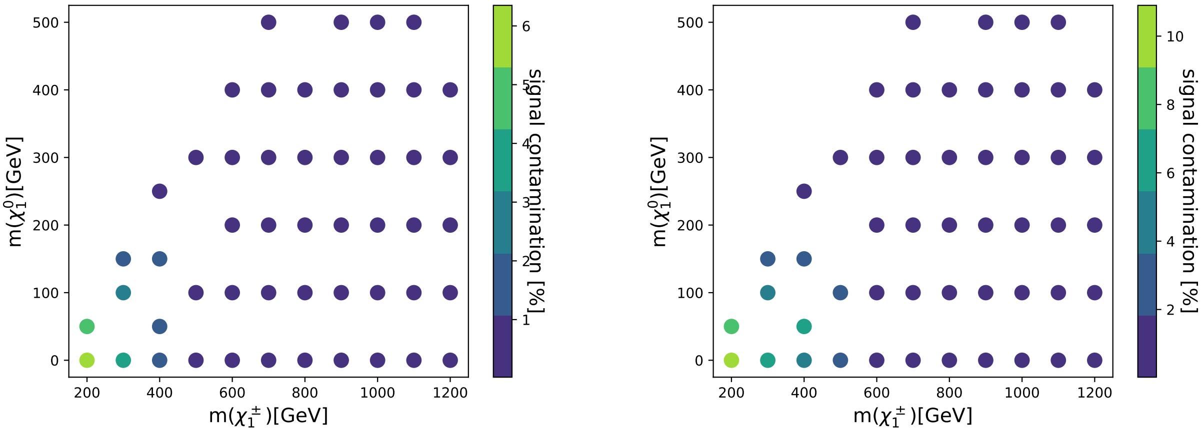

(a) WW model resolved region

(b) WW model boosted region

Figure 8.9: Signal contamination in W+jets CR

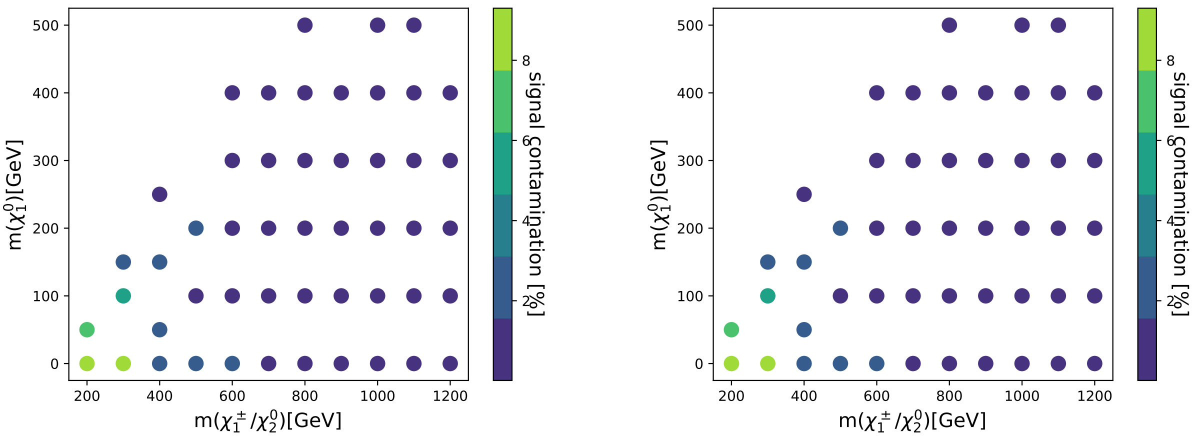

(a) WZ model resolved region

(b) WZ model boosted region

Figure 8.10: Signal contamination in W+jets CR

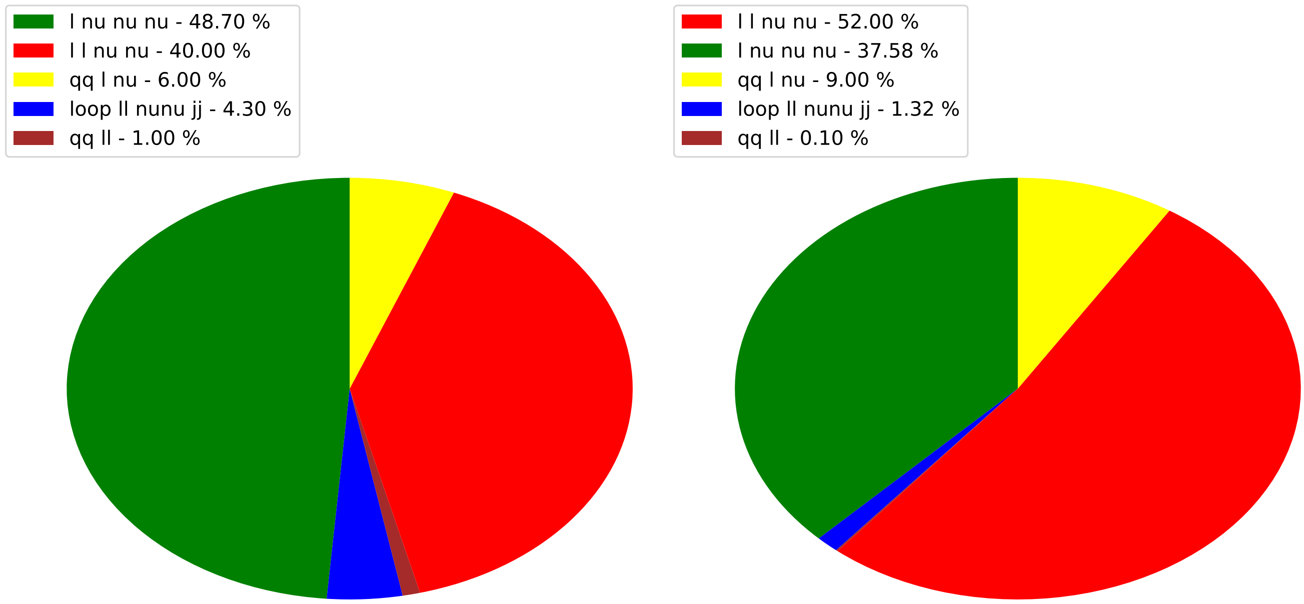

(a) resolved SR composition (b) boosted SR composition

Figure 8.11: Diboson component compositions in the WW model SR

8.3.3 Diboson CR definition

An additional challenge is presented by the definition of a diboson CR. Diboson is a non reducible background to the signal model as was mentioned in chapter 4. Furthermore, W+jets displays a very similar signature in the detector and since diboson is suppressed in kinematic regions targeting higher values of the missing transverse energy, it becomes more difficult to define a CR with a dominant diboson component. The reasoning behind this statement is that W+jets in regions using a large upper limit on the missing transverse energy is favourable compared to backgrounds that have more potential sources for real missing transverse energy.

Figure 8.11 shows the details of the background composition of diboson in the SRs. A significant contribution of cases with 2 leptons can be seen. This suggests the necessity of defining a second type of CRs for cases with 2 leptons. From a physical standpoint the 2 lepton component of the SR could be induced by cases where the second lepton is lost in the detector or reconstructed as a large R jet.

For the definition of the 2 lepton CR an additional variable is introduced.

Invariant mass of two leptons m_{ll}

m_{ll} is defined as the invariant mass of two leptons coming from the decay of a Z boson.

$$m_{\mathrm{ll}} = \sqrt{2lep^1_{P_T} lep^2_{P_T} [cos(lep^1_\eta - lep^2_\eta) - cos(lep^1_\phi - lep^2_\phi)]}$$

The introduction of m_{ll} is based on the idea that the dominant SM background like $t\bar{t}$ and W+jets are not expected to display a final state in which the reconstructed invariant mass of two leptons coincides with the mass of a Z boson.

2 lepton CR background composition

The definition of the 2 lepton diboson CR and the background composition are shown in the table below and figures 8.12 and 8.13. In all four regions diboson is the dominant SM process varying from 47.3% to 57.4%.

Variable	WW model resolved region	WW model boosted region	WZ model resolved region	WZ model boosted region
N_{lep}	=2	=2	=2	=2
$p_{\text{T}}^{\text{lep}}$[GeV]	> 25	> 25	> 25	> 25
N_{Jet}^{25}	$2-4$	$<= 4$	$<= 3$	$<= 4$
N_{bJet}^{25}	=0	=0	=0	=0
$E_{\text{T}}^{\text{miss}}$[GeV]	> 200	> 200	> 200	> 200
$\Delta\phi(p_{\text{T}}^{\text{lep}}, E_{\text{T}}^{\text{miss}})$	< 2.9	< 2.9	< 2.8	< 2.6
$\sigma_{E_{\text{T}}^{\text{miss}}}$	-	< 15	-	< 15
m_{ll}[GeV]	85-95	85-95	-	-
Number of large R jets	=0	>= 1	=0	>= 1
large R jet$_{\text{M}}^{1}$ [GeV]	-	< 100	-	< 105
W tagged	No	No	No	No
Z tagged	No	No	No	No
large R jet$_{p_{\text{T}}}^{1}$ [GeV]	-	> 300	-	> 250
m_{T} [GeV]	150-300	150-300	150-300	150-300

Notable differences to the initially defined SRs:
- Replace m_{jj} with the 2 lepton CR variable m_{ll}.
- No tagger is used, since the signature they are sensitive to, is not given in the diboson control region.
-A mass window for m_{T} was defined.

Signal contamination in the diboson 2L CR

For the diboson 2L CR, the WW and WZ cases must be considered separately. If looking at the case of the WW model, m_{ll} is useful for trying to reduce the signal contamination. Since the WW model is required to show a dileptonic decay configuration, it is not likely to reconstruct the invariant mass of these pairs in the Z boson mass window.
In the case of the WZ model larger signal contamination are expected, which are ultimately below the defined limit.

On the other hand the task of defining a 1-lepton CR has proven to be more difficult. This is, as the diboson processes decaying to a signature with a lepton show a similar final state as W+jets events with decays to leptonic final states. Fuelled by the higher statistics of W+jets in comparison to diboson, the definition of a CR displaying a dominant diboson background was not possible. One proposed solution would be to merge the diboson 1 lepton CR with the W+jets 1 lepton CRs.

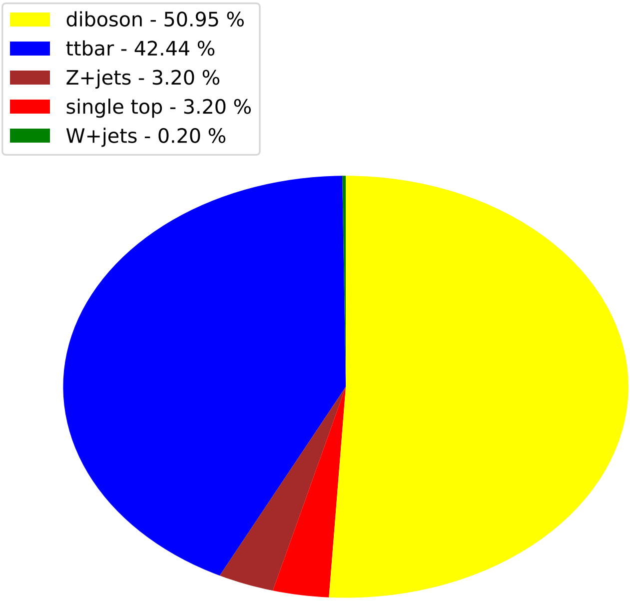

(a) WW model resolved 2L CR

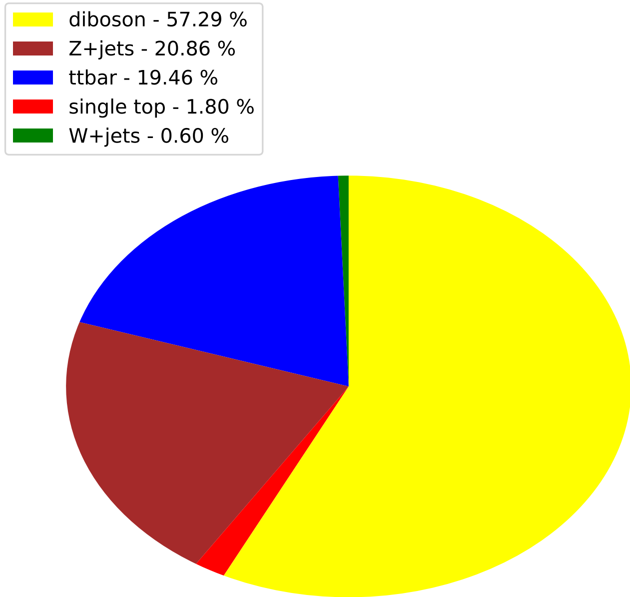

(b) WW model boosted 2L CR

Figure 8.12: Background compositions in the WW model 2L CR

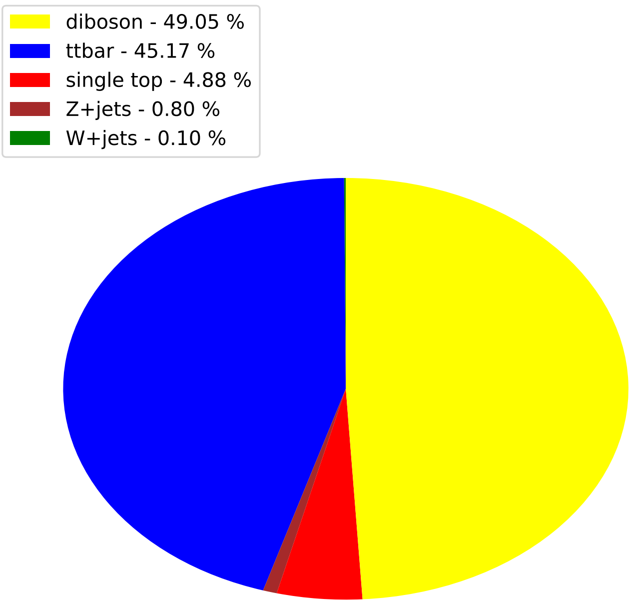

(a) WZ model resolved 2L CR

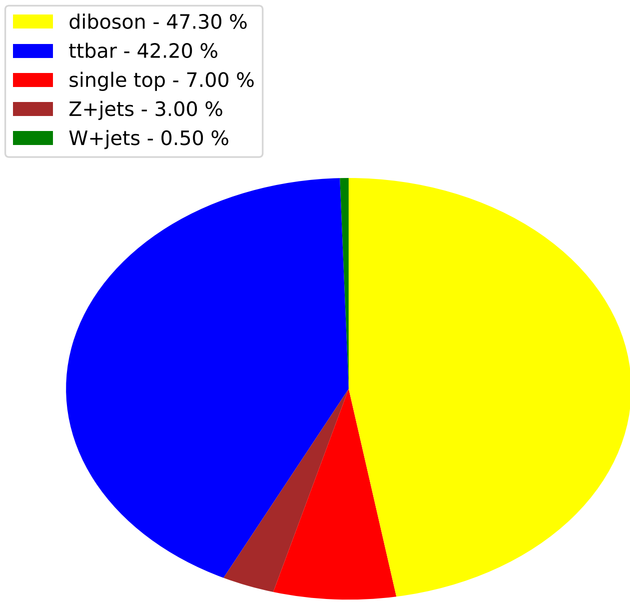

(b) WZ model boosted 2L CR

Figure 8.13: Background compositions in the WZ model 2L CR

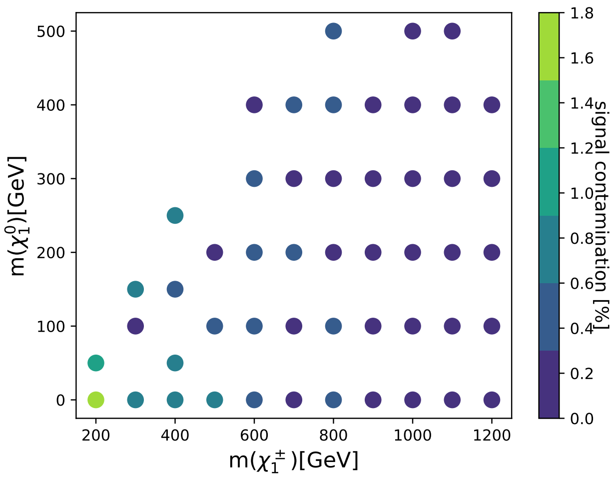

(a) WW model resolved 2L CR

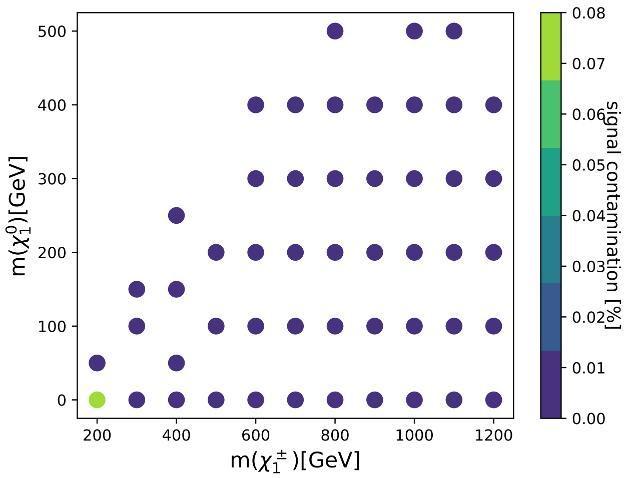

(b) WW model boosted 2L CR

Figure 8.14: Signal contamination in the WW model 2L CR

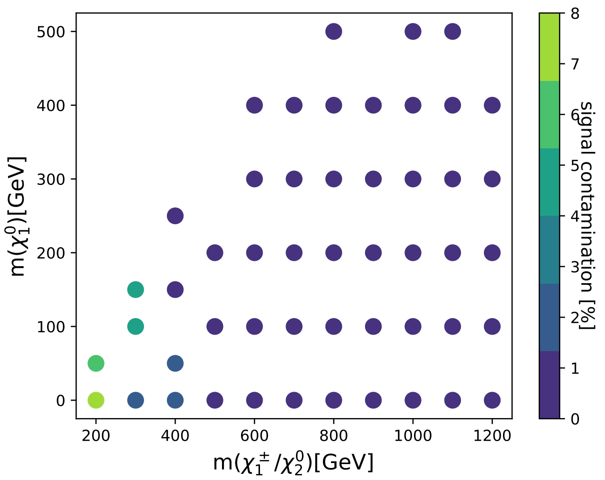

(a) WZ model resolved 2L CR

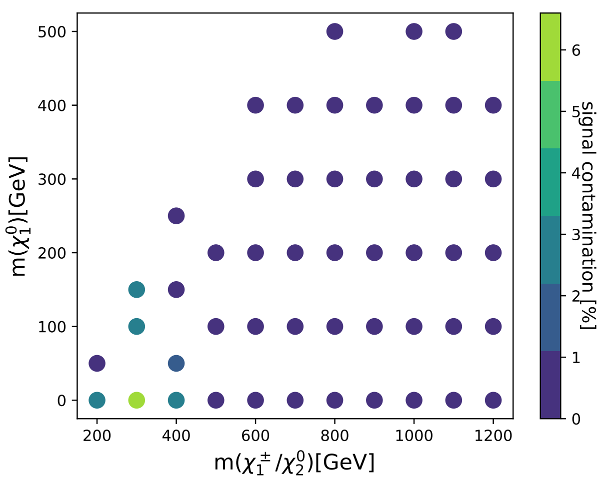

(b) WZ model boosted 2L CR

Figure 8.15: Signal contamination in the WZ model 2L CR

Chapter 9

Validation Region definitions

In a fit the CR defined in the previous chapter would be used to normalize the background estimation to data. The VRs are then used to validate the background predictions given by the CRs. As for the CRs two types of VR are defined: a set of VRs focussing on the resolved kinematic regions and a set of VR focussing on the boosted kinematic regions. Typically, VRs are placed between the SRs and CRs by changing the kinematic requirements on a small subset of variables. It is required to place the VRs in a close proximity to the SRs, because VRs are intended to reflect the background composition of the SR. In this section, only the regions used for the WW model are presented, while the study of the WZ model can be found in the appendix. Another important point influencing the definition of a VR is the signal contamination. As for the CR the VR are supposed to be free of signal events. Due to their proximity to the SR it becomes a challenging task to define VR without signal contamination. Therefore, an upper limit is set to 20% as the maximal amount of signal events in the VR. Plots displaying the signal contamination in the VR for both models can be seen in the Appendix. Signal contamination displayed in these plots are within the set limits.

9.1 Resolved VR definitions

A schematic display of the fit regions is shown in figure 8.6. The strategy used for the VR was to define side-bands next to the SR. They are separated from the SR by using m_{jj} and placing them at the higher and lower m_{jj} ranges next to the SR. Figure 9.1 shows the background composition of the VR in comparison to the background composition of the SR. Additionally the VR is separated in two bins coinciding with the two bins used in the resolved SR. For the binning m_{jj} intervals of 55 GeV $< m_{\mathrm{jj}} >$ 70 GeV and 90 GeV $< m_{\mathrm{jj}} >$ 105 GeV (For the WZ model: 65 GeV $< m_{\mathrm{jj}} >$ 80 GeV and 110 GeV $< m_{\mathrm{jj}} >$ 125 GeV) are combined.

Comparing the corresponding SR and VR background compositions (compare figure 9.1 a) with figure 9.1 b) and figure 9.1 c) and figure 9.1 d)) a good agreement was found.

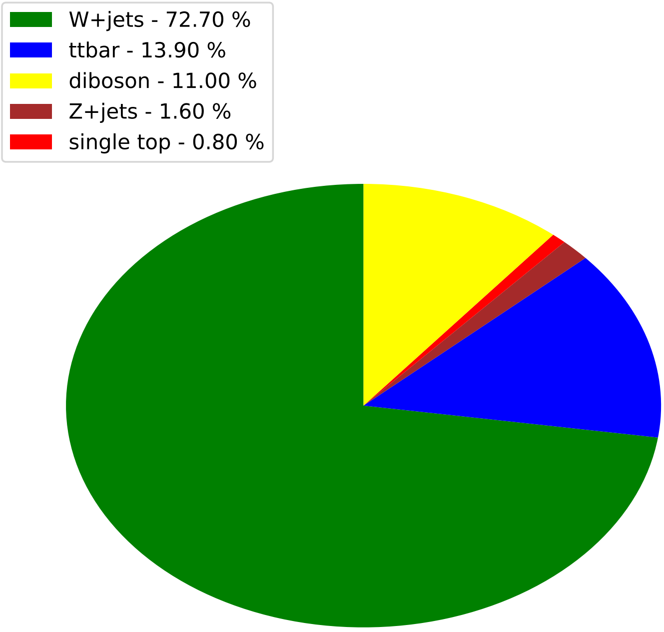

(a) Resolved SRLM

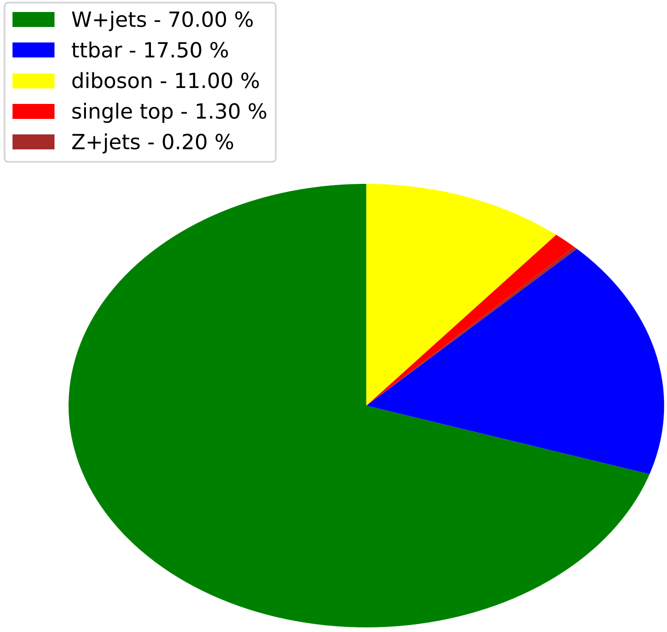

(b) Resolved VR m_{jj} bin 1

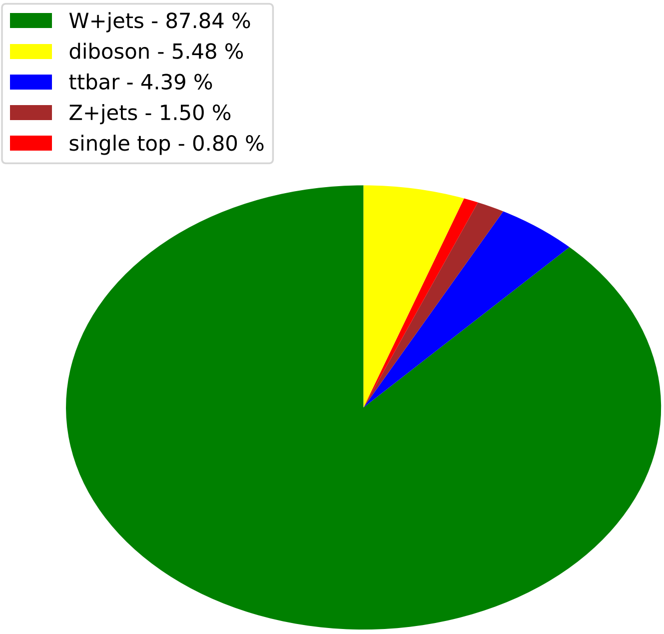

(c) Resolved SRHM

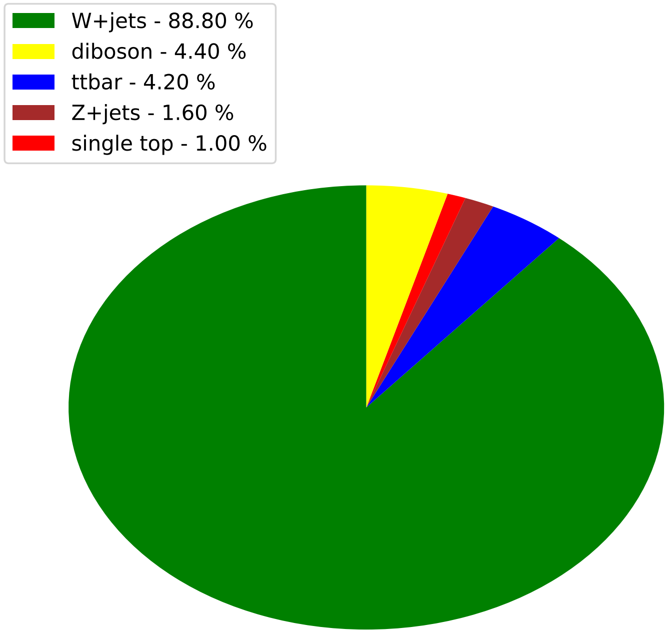

(d) Resolved VR m_{jj} bin 2

Figure 9.1: Background compositions in the SR and VR for the WW model

9.2 Boosted VR definitions

A schematic illustration of the boosted VR definition has already been presented in figure 8.6. The VR is placed between the W+jets CR and the boosted SRs. For the separation of the three regions the missing transverse energy significance is used. Figure 9.2 shows the comparison of the boosted VR and a summarized display of the boosted SR bins.

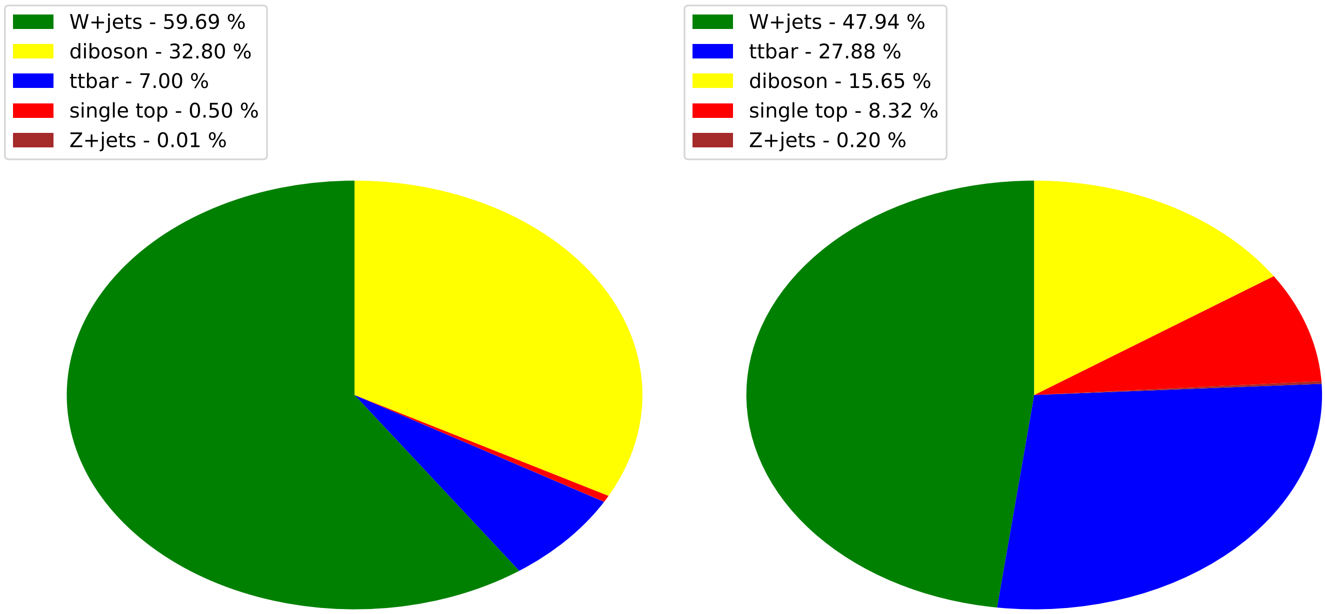

(a) Boosted SR

(b) Boosted VR

Figure 9.2: Background compositions in the SR and VR for the WW model

An interpretation of the preliminary VR definition is not possible at this ponit. In later stages of the analysis, these definitions will have to be validated.

Chapter 10

Summary

In conclusion, potential signal models depicting the pair production of electroweak gauginos decaying further to W and Z bosons and the lightest supersymmetric particle have been studied. For the first time, a complete set of SRs and preliminary CR and VR has been defined in the 1L-channel. A search in the 1L-channel presents the opportunity to target two types of kinematic regions. Namely a resolved and a boosted region, which have been defined in chapter 7. Moreover, the 1L-channel gives a clear signature in the detector with only one lepton and two jets.

The SR definitions are based on a three step optimisation strategy that was used for both models. A multidimensional cut scan gave a first indication about the kinematics of the model. Optimising both models for the best exclusion limits. Preliminary results displayed by an exclusion plot have shown a significant improvement in comparison to the results (19, 20) previously published in different final state signatures. The figures 7.9 and 7.10 show expected exclusions of chargino masses up to 725 GeV (WW model) and 740 GeV (WZ model) with a respective neutralino mass of 0 GeV in the boosted region of the phase space. In the resolved region the expected limit excludes for points with a neutralino mass of 180 GeV respective chargino masses of about 660 GeV (WZ model) and 640 GeV (WW model). In addition a set of CRs and VRs has been defined. The CRs aim to control the three main background processes of the analysis (W+jets, $t\bar{t}$, diboson). For all three SM backgrounds dedicated CRs have been defined for the resolved and boosted signatures. Completing the set of search regions are the definitions of preliminary VRs. In ongoing efforts all defined regions will be validated. These are then expected to be used in a publication.

Bibliography

[1] Alberto Zucchetta. Heavy resonances (W', Z', jets) in ATLAS and CMS in Run 2. In *54th Rencontres de Moriond on Electroweak Interactions and Unified Theories (Moriond EW 2019) La Thuile, Italy, March 16-23, 2019*, 2019.

[2] David J Griffiths. *Introduction to elementary particles; 2nd rev. version.* Wiley, New York, NY, 2008.

[3] Mark Thomson. *Modern particle physics.* Cambridge University Press, New York, 2013.

[4] Masaki Hori. Lecture notes in Modern Atomic and Nuclear Physics 2, Ludwig-Maximilians-Universität München, 10.2018-03.2019 .

[5] Dorothee Schaile. Lecture notes in Advanced Particle Physics, Ludwig-Maximilians-Universität München, 04.2018-10.2018 .

[6] Stephen P. Martin. A Supersymmetry primer. 1997. [Adv. Ser. Direct. High Energy Phys.18,1(1998)].

[7] Standard model of particle physics. `https://favpng.com/png_view/field-particle-physics-standard-model-elementary-particle-higgs-boson-png/JwgQnwMF`, . Accessed: 2020-03-13.

[8] Makoto Kobayashi and Toshihide Maskawa. CP Violation in the Renormalizable Theory of Weak Interaction. *Prog. Theor. Phys.*, 49, 1973.

[9] Julien Lesgourgues and Sergio Pastor. Neutrino cosmology and Planck. *New J. Phys.*, 16:065002, 2014.

[10] F. Del Aguila, J. Gluza, and M. Zralek. The Minimal extension of the SM and the neutrino oscillation data. *Acta Phys. Polon.*, B30:3139–3147, 1999.

[11] Beta plus and beta minus decay. `https://www.fizzics.org/beta-plus-and-beta-minus-notes-and-video-lesson/`, . Accessed: 2020-03-18.

[12] Jens Erler and Matthias Schott. Electroweak Precision Tests of the Standard Model after the Discovery of the Higgs Boson. *Prog. Part. Nucl. Phys.*, 106:68–119, 2019.

[13] Wendy L. Freedman and Michael S. Turner. Measuring and understanding the universe. *Rev. Mod. Phys.*, 75:1433–1447, 2003.

[14] Howard Baer, Andre Lessa, Shibi Rajagopalan, and Warintorn Sreethawong. Mixed axion/neutralino cold dark matter in supersymmetric models. *JCAP*, 1106, 2011.

[15] ATLAS Collaboration. Observation of a new particle in the search for the Standard Model Higgs boson with the ATLAS detector at the LHC. *Phys. Lett.*, B716:1–29, 2012.

[16] Pradipta Ghosh and Sourov Roy. Neutrino masses and mixing, lightest neutralino decays and a solution to the mu problem in supersymmetry. *JHEP*, 04:069, 2009.

[17] George Lazarides, Q. Shafi, and C. Wetterich. Proton Lifetime and Fermion Masses in an SO(10) Model. *Nucl. Phys.*, B181:287–300, 1981.

[18] S. Dawson. The MSSM and why it works. In *Supersymmetry, supergravity and supercolliders. Proceedings, Theoretical Advanced Study Institute in elementary particle physics, TASI'97, Boulder, USA, June 2-27, 1997*, pages 261–339, 1997.

[19] The ATLAS collaboration. Search for electroweak production of charginos and sleptons decaying in final states with two leptons and missing transverse momentum in $\sqrt{s} = 13$ TeV pp collisions using the ATLAS detector. 3 2019.

[20] The ATLAS collaboration. Search for chargino-neutralino production with mass splittings near the electroweak scale in three-lepton final states in $\sqrt{s} = 13$ TeV pp collisions with the ATLAS detector. 5 2019.

[21] Lyndon R Evans. LHC Accelerator Physics and Technology Challenges; rev. version. (LHC-Project-Report-303. CERN-LHC-Project-Report-303):6 p, Apr 1999.

[22] ATLAS Collaboration. The ATLAS Experiment at the CERN Large Hadron Collider. *JINST*, 3:S08003, 2008.

[23] Mirko Berretti. Development of reconstruction algorithms for inelastic processes studies in the TOTEM experiment at LHC. Master's thesis, Siena U., 2008-06-04.

[24] Sushil Singh Chauhan. *Search for Quark Compositeness at $\sqrt{s} = 14$ TeV at the Large Hadron Collider*. PhD thesis, Delhi U., 2010.

[25] LHC Report: LS2 has just begun. `https://home.cern/news/news/accelerators/lhc-report-another-run-over-and-ls2-has-just-begun`. Accessed: 2020-03-12.

[26] ATLAS. Luminositypublicresultsrun2, 2019. URL `https://twiki.cern.ch/twiki/bin/view/AtlasPublic/JetEtmissPublicResultsRetired`.

[27] Atlas: Detector technology. `https://atlas.cern/discover/detector`, . Accessed: 2020-03-10.

[28] ATLAS inner detector: Technical design report. Vol. 2. 1997.

[29] Bartosz Mindur. ATLAS Transition Radiation Tracker (TRT): Straw tubes for tracking and particle identification at the Large Hadron Collider. *Nucl. Instrum. Meth.*, A845, 2017.

[30] *ATLAS Collaboration liquid-argon calorimeter: Technical Design Report*. Technical Design Report ATLAS. CERN, Geneva, 1996.

[31] *ATLAS tile calorimeter: Technical Design Report*. Technical Design Report ATLAS. CERN, Geneva, 1996.

[32] *ATLAS muon spectrometer: Technical Design Report*. Technical Design Report ATLAS. CERN, Geneva, 1997.

[33] ATLAS Collaboration. Construction and Test of MDT Chambers for the ATLAS Muon Spectrometer. *Nucl. Instrum. Meth.*, A461:17–20, 2001.

[34] J Wotschack. ATLAS Collaboration Muon Chamber Construction Parameters for CSC, MDT, and RPC chambers. Technical Report ATL-MUON-PUB-2008-006. ATL-COM-MUON-2008-008, CERN, Geneva, Apr 2008. Back-up document for the ATLAS Detector Paper.

[35] Christoph Amelung. Upgrade of the ATLAS Muon System for the HL-LHC. Technical Report ATL-MUON-PROC-2018-005, CERN, Geneva, Jun 2018.

[36] Cristobal Padilla. The ATLAS trigger system. *IEEE Trans. Nucl. Sci.*, 57:650–657, 2010.

[37] Maria Spiropulu and Steinar Stapnes. LHC's ATLAS and CMS detectors. *Int. J. Mod. Phys.*, A23:4081–4105, 2008. [,25(2008)].

[38] ATLAS Collaboration. Electron reconstruction and identification in the ATLAS experiment using the 2015 and 2016 LHC proton-proton collision data at $\sqrt{s} = 13$ TeV. *Eur. Phys. J.*, C79(8):639, 2019.

[39] ATLAS Collaboration. Muon reconstruction performance of the ATLAS detector in proton–proton collision data at $\sqrt{s}$ =13 TeV. *Eur. Phys. J.*, C76(5):292, 2016.

[40] B. R. Webber. Hadronization. In *Proceedings: Summer School on Hadronic Aspects of Collider Physics, Zuoz, Switzerland, Aug 23-31, 1994*, pages 49–77, 1994.

[41] Electron identification measurements in ATLAS using $\sqrt{s} = 13$ TeV data with 50 ns bunch spacing. Technical Report ATL-PHYS-PUB-2015-041, CERN, Geneva, Sep 2015.

[42] ATLAS Collaboration. Electron and photon performance measurements with the ATLAS detector using the 2015–2017 LHC proton-proton collision data. *JINST*, 14(12):P12006, 2019.

[43] The ATLAS collaboration. Searches for electroweak production of supersymmetric particles with compressed mass spectra in $\sqrt{s} = 13$ TeV pp collisions with the ATLAS detector. 2019.

[44] Matteo Cacciari, Gavin P. Salam, and Gregory Soyez. The anti-k_t jet clustering algorithm. *JHEP*, 04:063, 2008.

[45] The ATLAS collaboration. Luminosity determination in pp collisions at $\sqrt{s} = 13$ TeV using the ATLAS detector at the LHC. 2019.

[46] ATLAS Collaboration. ATLAS data quality operations and performance for 2015-2018 data-taking. 2019.

[47] Andy Buckley et al. General-purpose event generators for LHC physics. *Phys. Rept.*, 504:145–233, 2011.

[48] ATLAS Collaboration. ATLAS Monte Carlo tunes for MC09. 2010.

[49] ATLAS Collaboration. Search for direct production of electroweakinos in final states with one lepton, missing transverse momentum and a Higgs boson decaying into two b-jets in (pp) collisions at $\sqrt{s} = 13$ TeV with the ATLAS detector. 2019.

[50] Eric Schanet. Sensitivity studies for a search for charginos in finalstates with one lepton with the atlas detector and interpretation of a search for gluinos and squarks in the pmssm, 2018.

[51] Andrea Giammanco. Single top quark production at the LHC. *Rev. Phys.*, 1:1–12, 2016.

[52] Carlo Oleari. The POWHEG-BOX. *Nucl. Phys. Proc. Suppl.*, 205-206:36–41, 2010.

[53] Hung-Liang Lai, Marco Guzzi, Joey Huston, Zhao Li, Pavel M. Nadolsky, Jon Pumplin, and C. P. Yuan. New parton distributions for collider physics. *Phys. Rev.*, D82:074024, 2010.

[54] Riccardo Di Sipio. Shower it again, Pythia. *Phys. Open*, 1:100002, 2019.

[55] Enrico Bothmann et al. Event Generation with Sherpa 2.2. *SciPost Phys.*, 7(3):034, 2019.

[56] Richard D. Ball et al. Parton distributions from high-precision collider data. *Eur. Phys. J.*, C77(10):663, 2017.

[57] Stefan Hoeche, Frank Krauss, Marek Schonherr, and Frank Siegert. QCD matrix elements + parton showers: The NLO case. *JHEP*, 04:027, 2013.

[58] Johan Alwall, Michel Herquet, Fabio Maltoni, Olivier Mattelaer, and Tim Stelzer. MadGraph 5 : Going Beyond. *JHEP*, 06:128, 2011.

[59] S. Redaelli. Beam Cleaning and Collimation Systems. In *Proceedings, 2014 Joint International Accelerator School: Beam Loss and Accelerator Protection: Newport Beach, CA, USA, November 5-14, 2014*, pages 403–437, 2016.

[60] ATLAS Collaboration. Characterisation and mitigation of beam-induced backgrounds observed in the ATLAS detector during the 2011 proton-proton run. *JINST*, 8:P07004, 2013.

[61] D. Abbaneo et al. Combined results on B hadron production rates, lifetimes, oscillations and semileptonic decays. 2000.

[62] Expected performance of the ATLAS b-tagging algorithms in Run-2. Technical Report ATL-PHYS-PUB-2015-022, CERN, Geneva, Jul 2015.

[63] ATLAS Collaboration. Optimisation of the ATLAS b-tagging performance for the 2016 LHC Run. Technical Report ATL-PHYS-PUB-2016-012, CERN, Geneva, Jun 2016.

[64] 1 lepton SUSY group. Search for squarks, gluinos and electroweakinos in events with an isolated lepton, jets and missing transverse momentum at $\sqrt{s} = 13$ TeV with the ATLAS detector. Technical Report ATL-COM-PHYS-2018-1638, CERN, Geneva, Nov 2018.

[65] M. Baak, G. J. Besjes, D. Côte, A. Koutsman, J. Lorenz, and D. Short. HistFitter software framework for statistical data analysis. *Eur. Phys. J.*, C75:153, 2015.

[66] Alexander L. Read. Presentation of search results: The CL(s) technique. *J. Phys.*, G28: 2693–2704, 2002. [,11(2002)].

[67] ATLAS Collaboration. Object-based missing transverse momentum significance in the ATLAS detector. Technical Report ATLAS-CONF-2018-038, CERN, Geneva, Jul 2018.

[68] ATLAS Collaboration. Performance of top-quark and W-boson tagging with ATLAS in Run 2 of the LHC. *Eur. Phys. J.*, C79(5):375, 2019.

[69] Andrew J. Larkoski, Ian Moult, and Duff Neill. Power Counting to Better Jet Observables. *JHEP*, 12:009, 2014.

[70] Nikolai Hartmann. ahoi. `https://gitlab.com/nikoladze/ahoi`. Accessed: 2020-03-17.

Appendix A

WZ model VR study

A.1 Resolved regions background comparisons

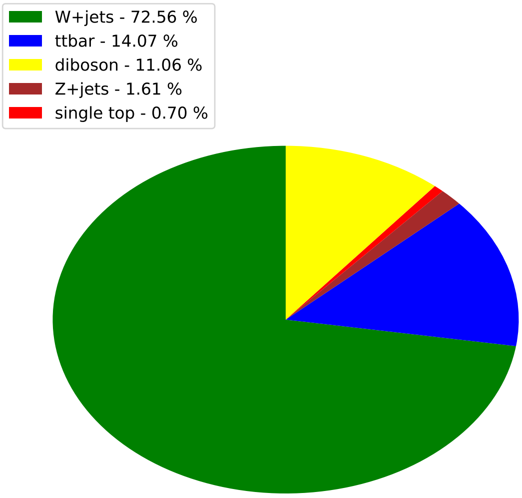

(a) Resolved SRLM

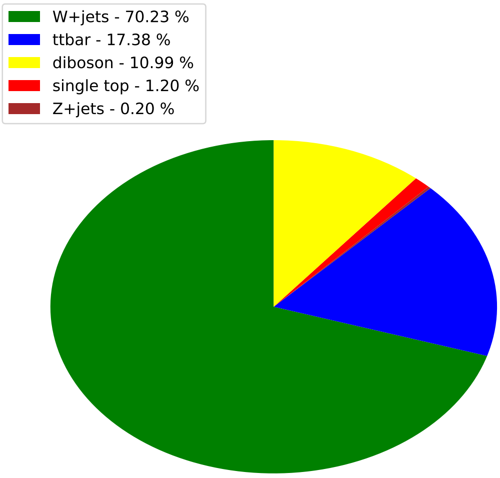

(b) Resolved VR m_{jj} bin 1

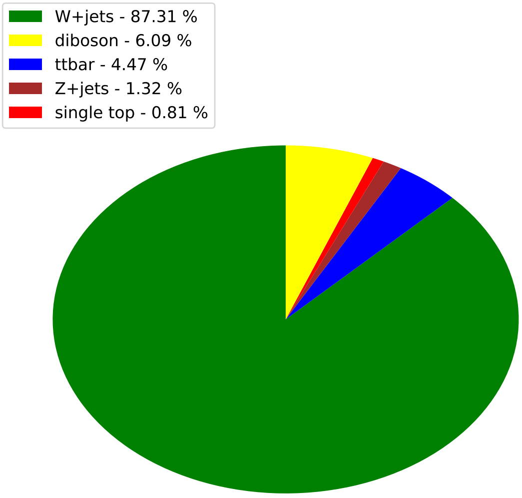

(c) Resolved SRHM

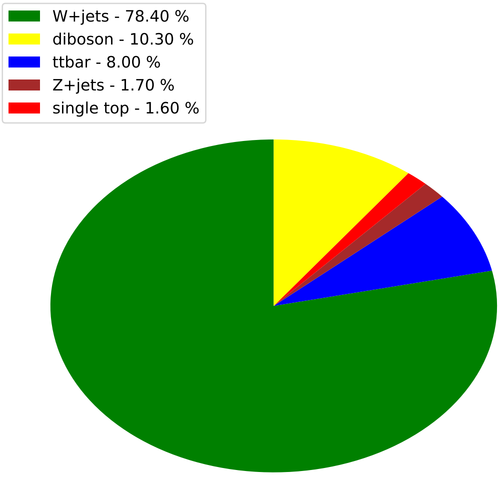

(d) Resolved VR m_{jj} bin 2

Figure A.1: Background compositions in the SR and VR for the WZ model

A.2 Boosted regions background comparisons

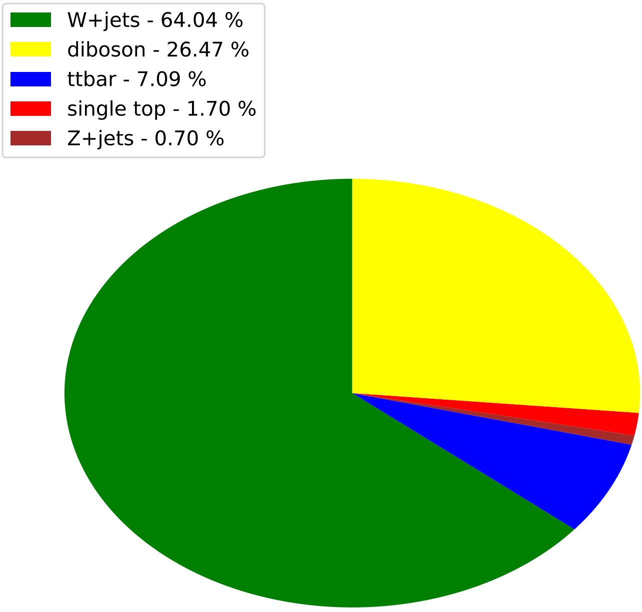

(a) Boosted SR

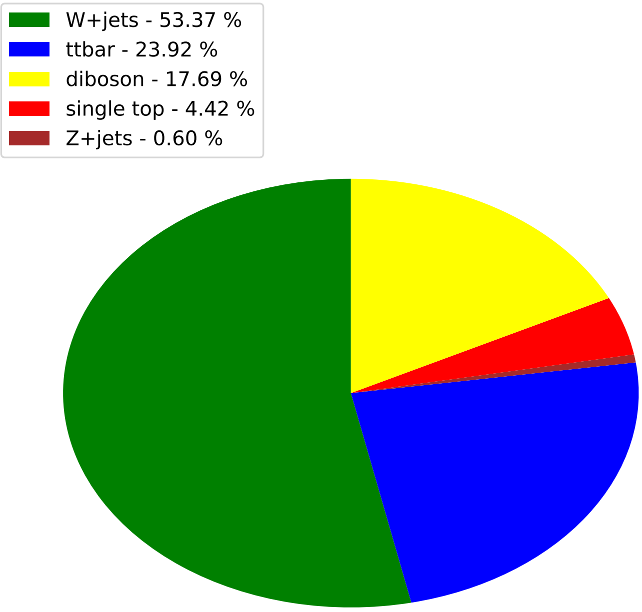

(b) Boosted VR

Figure A.2: Background compositions in the SR and VR for the WZ model

Appendix B

Yieldstables of the shown CRs

B.1 Yieldstables WW for the CR

Yields for W+jets CR

Process	resolved	boosted
Total SM	662.51 ± 33.01	246.53 ± 8.12
$t\bar{t}$	137.45 ± 3.79	83.08 ± 2.73
Diboson	54.64 ± 1.91	32.33 ± 2.53
W+jets	447.79 ± 32.63	105.88 ± 6.67
Single top	17.83 ± 2.20	23.80 ± 2.73
Z+jets	4.79 ± 1.58	1.44 ± 0.41
Unweighted Total SM	10324	5931
Unweighted $t\bar{t}$	2877	2645
Unweighted Diboson	5306	1756
Unweighted W+jets	1997	1360
Unweighted Single top	70	109
Unweighted Z+jets	74	61

Yields for $t\bar{t}$ CR

Process	resolved	boosted
Total SM	105.19 ± 3.57	86.85 ± 3.52
$t\bar{t}$	94.80 ± 3.20	62.43 ± 2.36
Diboson	0.23 ± 0.13	0.44 ± 0.18
W+jets	2.37 ± 0.68	1.81 ± 0.44
Single top	7.73 ± 1.43	22.15 ± 2.56
Z+jets	0.05 ± 0.05	0.02 ± 0.02
Unweighted Total SM	1940	2036
Unweighted $t\bar{t}$	1824	1894
Unweighted Diboson	36	13
Unweighted W+jets	45	29
Unweighted Single top	31	99
Unweighted Z+jets	4	1

Yields for diboson CR

Process	resolved	boosted
Total SM	110.95 ± 6.22	90.25 ± 3.42
$t\bar{t}$	44.78 ± 2.67	29.82 ± 1.56
W+jets	0.76 ± 0.50	0.40 ± 0.38
Z+jets	8.88 ± 4.05	18.87 ± 1.94
Diboson	47.78 ± 2.36	36.80 ± 1.60
Single top	6.46 ± 1.98	4.36 ± 1.67
Unweighted Total SM	2293	3376
Unweighted $t\bar{t}$	637	861
Unweighted W+jets	3	2
Unweighted Z+jets	69	1060
Unweighted Diboson	1572	1446
Unweighted Single top	11	7

B.2 Yieldstable WZ for the CR

Yields for W+jets CR

Process	resolved	boosted
Total SM	995.51 ± 40.04	413.25 ± 13.01
$t\bar{t}$	206.08 ± 4.71	140.77 ± 3.68
Diboson	80.22 ± 2.28	51.79 ± 2.73
W+jets	672.18 ± 39.57	189.47 ± 11.81
Single top	24.51 ± 2.54	28.39 ± 2.91
Z+jets	12.52 ± 1.98	2.83 ± 0.71
Unweighted Total SM	14841	9129
Unweighted $t\bar{t}$	4222	3730
Unweighted Diboson	7552	3247
Unweighted W+jets	2839	1953
Unweighted Single top	109	126
Unweighted Z+jets	119	73

Yields for $t\bar{t}$ CR

Process	resolved	boosted
Total SM	179.81 ± 4.73	152.19 ± 4.46
$t\bar{t}$	162.64 ± 4.21	125.07 ± 3.60
Diboson	0.30 ± 0.19	0.62 ± 0.24
W+jets	3.48 ± 1.03	2.46 ± 0.50
Single top	13.30 ± 1.90	23.99 ± 2.58
Z+jets	0.09 ± 0.05	0.05 ± 0.03
Unweighted Total SM	3188	3297
Unweighted $t\bar{t}$	3034	3124
Unweighted Diboson	44	28
Unweighted W+jets	53	40
Unweighted Single top	53	102
Unweighted Z+jets	4	3

Yields for diboson CR

Process	resolved	boosted
Total SM	111.29 ± 8.04	126.16 ± 3.76
$\mathrm{t\bar{t}}$	44.21 ± 2.69	45.17 ± 2.09
W+jets	0.76 ± 0.50	0.40 ± 0.38
Z+jets	5.25 ± 6.45	17.53 ± 1.22
Diboson	54.15 ± 2.75	56.93 ± 2.07
Single top	4.62 ± 1.65	6.13 ± 1.97
Unweighted Total SM	2359	4243
Unweighted $\mathrm{t\bar{t}}$	605	1105
Unweighted W+jets	3	2
Unweighted Z+jets	55	1020
Unweighted Diboson	1686	2106
Unweighted Single top	9	10

Appendix C

Yieldstables of the shown VRs

C.1 Yieldstable WW for the VR

Process	resolved VR bin1	resolved VR bin2	boosted VR
Total SM	576.60 ± 93.53	568.44 ± 77.02	132.06 ± 7.95
$t\bar{t}$	99.89 ± 2.77	24.21 ± 1.27	30.58 ± 1.34
W+jets	391.14 ± 93.42	504.93 ± 76.93	71.49 ± 7.53
Single top	9.44 ± 1.63	4.95 ± 1.24	7.20 ± 1.46
Diboson	72.98 ± 1.50	25.06 ± 1.10	21.73 ± 1.58
Z+jets	3.15 ± 3.03	9.29 ± 2.98	1.06 ± 0.37
Unweighted Total SM	12737	4706	3846
Unweighted $t\bar{t}$	3111	1059	1386
Unweighted W+jets	1678	998	560
Unweighted Single top	37	22	30
Unweighted Diboson	7816	2561	1843
Unweighted Z+jets	95	66	27

C.2 Yieldstable WZ for the VR

Process	resolved VR bin1	resolved VR bin2	boosted VR
Total SM	274.40 ± 31.87	98.13 ± 26.11	117.49 ± 7.07
$t\bar{t}$	47.93 ± 1.93	7.87 ± 0.71	28.19 ± 1.28
W+jets	192.73 ± 31.73	76.89 ± 26.02	62.54 ± 6.67
Single top	3.52 ± 0.94	1.62 ± 0.66	5.21 ± 1.20
Diboson	29.86 ± 0.89	10.04 ± 1.04	20.79 ± 1.48
Z+jets	0.36 ± 1.82	1.71 ± 1.49	0.75 ± 0.36
Unweighted Total SM	5511	1651	3752
Unweighted $t\bar{t}$	1509	355	1269
Unweighted W+jets	655	330	566
Unweighted Single top	17	6	24
Unweighted Diboson	3291	949	1873
Unweighted Z+jets	39	11	20

Appendix D

Signal contamination in VRs

The signal contamination plots that were mentioned in chapter 9. All plots show signal contaminations below the set limit of 20%.

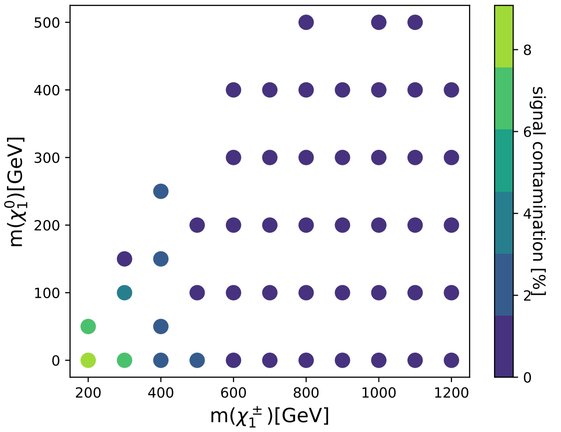

(a) Resolved WW VR m_{jj} bin 1

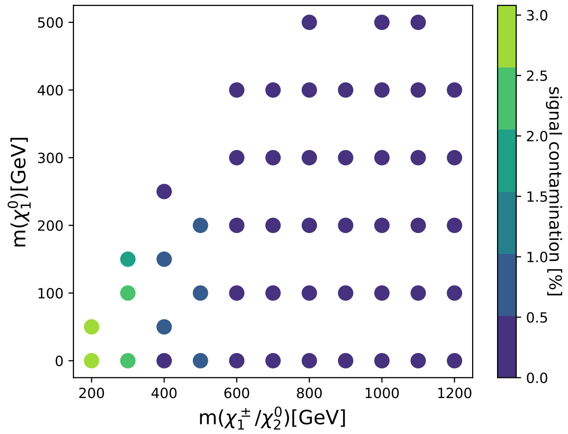

(b) Resolved WZ VR m_{jj} bin 1

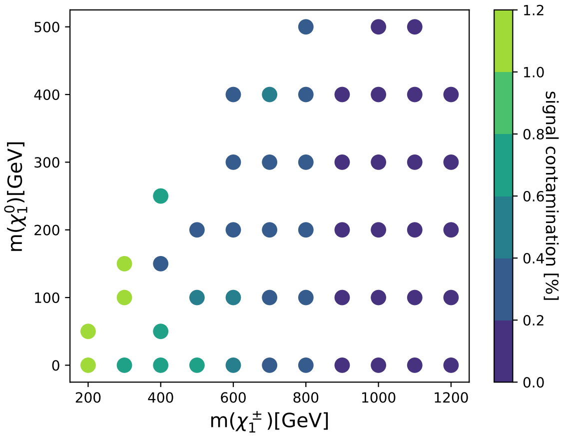

(c) Resolved WW VR m_{jj} bin 2

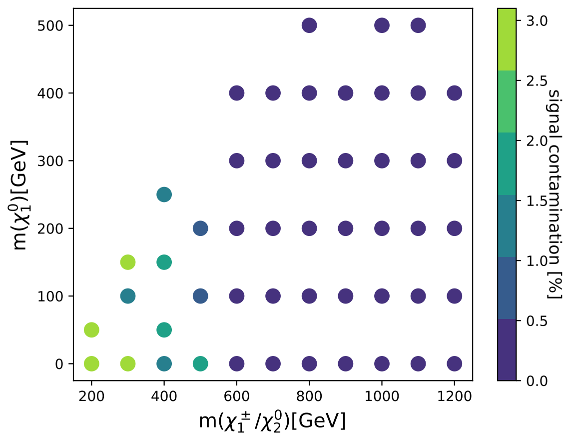

(d) Resolved WZ VR m_{jj} bin 2

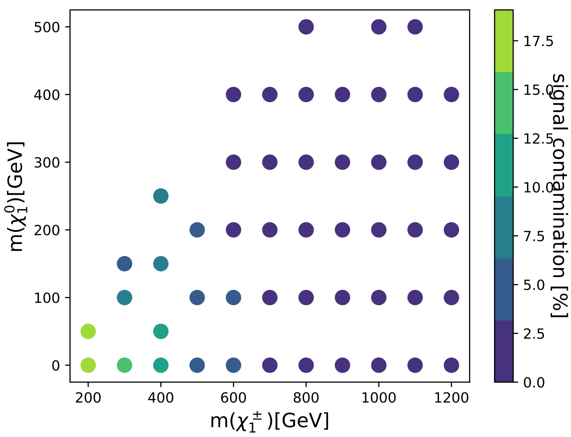

(e) Boosted WW VR

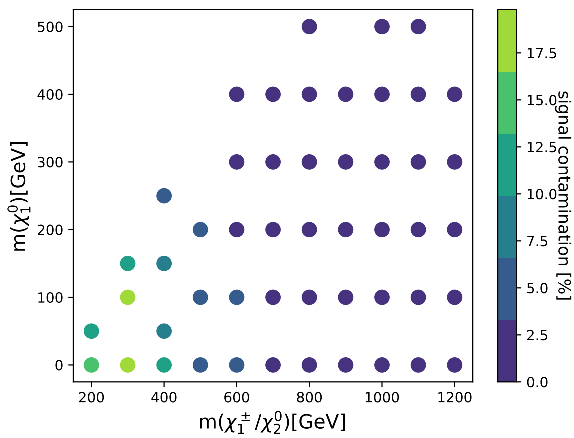

(f) Boosted WZ VR

Selbständigkeitserklärung

Ich versichere hiermit, die vorliegende Arbeit mit dem Titel

Search for charginos and neutralinos decaying to final states with one lepton

selbständig verfasst zu haben und keine anderen als die angegebenen Quellen und Hilfsmittel verwendet zu haben.

Vorname Name

München, den 01. April 2020